MS53035
MASTER THESIS:

Fracture toughness testing of Advanced High Strength Steels for automotive applications

---

Company supervisor:	dr. A.R. Chezan
University supervisor:	dr. V.A. Popovich
Graduation committee:	prof.dr. J. Sietsma
	ir. T. Boot
Author:	H. Halilović

Materials Science and Engineering

Delft, August 6, 2021

Preface

The research done during this thesis would not have been possible without the immense support I received from my girlfriend, family, and all of my colleagues at Tata Steel IJmuiden. Even though the experimental efforts were quite demanding at times, we were able to wrap this project up successfully. A million thank you's to all those involved, especially Toni for granting me this great opportunity to prove and develop myself as an engineer. I sincerely hope that this thesis will make a valuable contribution to the company.

-Haris

Abstract

Carbon dioxide emissions from the transportation sector account for roughly one-third of world-wide CO2 emissions. Governmental pressure to tackle this problem has forced the industry to adapt with regard to material development. One such adaption is the development and application of advanced high-strength steels (AHSS), offering high specific strength combined with improved ductility. This enables lightweighting of consumer cars, as well as improving the overall occupant safety and crash-worthiness. Despite these apparent advantages of AHSS, sheet metal forming operations can cause unexpected edge-cracking. In this research the occurrence of edge-cracking is investigated and rationalized with fracture toughness testing. The Essential Work of Fracture (EWF) methodology is applied on double-edge notched (DENT) specimens, an increasingly applied method to characterize the crack propagation resistance of thin sheet metal. A novel sample preparation method is evaluated here, based on sheared notches instead of fatigue pre-cracked specimens. The obtained fracture toughness parameters are validated against laboratory-scale deep-drawing experiments to estimate its predictive capabilities. Scanning electron microscopy (SEM) was employed to examine the fractured surfaces and to identify the relevant micro-mechanisms of fracture. It was found that the obtained EWF results are in good agreement with the observed cracking behaviour during deep-drawing. Both the established method (fatigue pre-cracking) as well as the novel method of sheared notches were able to reveal the intrinsically low fracture toughness, otherwise undetected with conventional tensile testing. From the fractured surfaces of the EWF samples the relevant micro-mechanisms of failure were identified that govern the fracture toughness properties. Transgranular cleavage fracture was responsible for brittle behaviour while failure ductile failure occurred via microvoid coalescence. Although the fatigue pre-cracking method for EWF testing seems to show a higher accuracy in predicting the cracking susceptibility, the shearing method can be employed as a rapid routine test to identify deterioration of fracture toughness properties early on.

Contents

List of symbols

Symbol	Description	Units
a	Crack length	m
b	Size of the burgers vector $\vec{b}$	m
E	Young's modulus	GPa
G	Shear modulus	GPa
HEC	Hole-expansion capacity	%
K_c	Critical stress intensity factor	MPa$\cdot\sqrt{\text{m}}$
K_I	Stress intensity factor in mode I	MPa$\cdot\sqrt{\text{m}}$
K_{Ic}	Critical (plane strain) stress intensity factor in mode I	MPa$\cdot\sqrt{\text{m}}$
K_{eff}	Local stress intensity factor in mode I	MPa$\cdot\sqrt{\text{m}}$
L_0	Initial ligament length	m
n	Strain-hardening exponent	[-]
R_m	(Ultimate) tensile strength	MPa
$R_{p0.2}$	0.2% offset yield strength	MPa
r	Plastic anisotropy (Lankford) coefficient	[-]
r_p	Second-order plastic zone size	m
r_y	First-order plastic zone size	m
W_e	Essential work of fracture	J
W_f	Total work of fracture	J
W_p	Non-essential plastic work of fracture	J
w_e	Specific essential work of fracture	J/m^2
w_f	Specific total work of fracture	J/m^2
w_p	Specific non-essential work of fracture	J/m^2
β	Plasticity shape factor	m^{-1}
$\Delta\tau$	Bowing stress (Orowan mechanism)	MPa
δ	Mean free path for dislocation glide	m
$\bar{\bar{\varepsilon}}$	Strain tensor	[-]
ε_t	Total elongation	%
ε_u	Uniform elongation	%
η	Stress triaxiality	[-]
λ	Dislocation source spacing	m
ν	Poisson's ratio	[-]
ρ	Notch curvature	m^{-1}
σ_{app}	Nominally applied load	MPa
σ_{eq}	Von-Mises equivalent stress	MPa
σ_h	Hydrostatic stress	MPa
σ_n	Net sectional stress	MPa
σ_Y	Yield strength	MPa
τ_{crss}	Critical resolved shear stress	MPa

Abbreviations

AHSS	...	advanced high-strength steel
BCC	...	body-centered cubic
CAE	...	computer aided engineering
CP	...	complex phase
CTOD	...	crack-tip opening displacement
DBTT	...	ductile-to-brittle transformation temperature
DENT	...	double-edge notched tension specimen
DIC	...	digital image correlation
DP	...	dual phase
EDM	...	electrical discharge machining
EDX	...	energy dispersive x-ray
EPFM	...	elastic-plastic fracture mechanics
EWF	...	essential work of fracture
FCC	...	face-centered cubic
FLD	...	forming limit diagram
FPZ	...	fracture process zone
HCP	...	hexagonal close-packed
HSLA	...	high-strength low alloy
LEFM	...	linear elastic fracture mechanics
LOM	...	light optical microscopy
SEM	...	scanning electron microscopy
TEM	...	transmission electron microscopy

1. Introduction

1.1 Context

In light of the continuously increasing carbon emissions world-wide, legislative pressure from government bodies has forced the industry to adapt. One such adaptation is to lower CO_2 emissions produced by the transportation sector. The CO_2 emissions from the transportation sector account for roughly $1/3^{rd}$ of worldwide emissions, and can be considered the most polluting sector (see Figure 1.1). Tackling this problem can be done in numerous ways; decreasing raw-material production emissions, reducing vehicle emissions, improving recyclability of materials, etcetera. Some governments have responded by setting CO_2 emission targets on consumer cars, expressed in the amount of CO_2 emitted per driven kilometer[1]. It is measures such as these that drive the need for lightweighting of cars, as it is an effective measure to decrease fuel consumption.

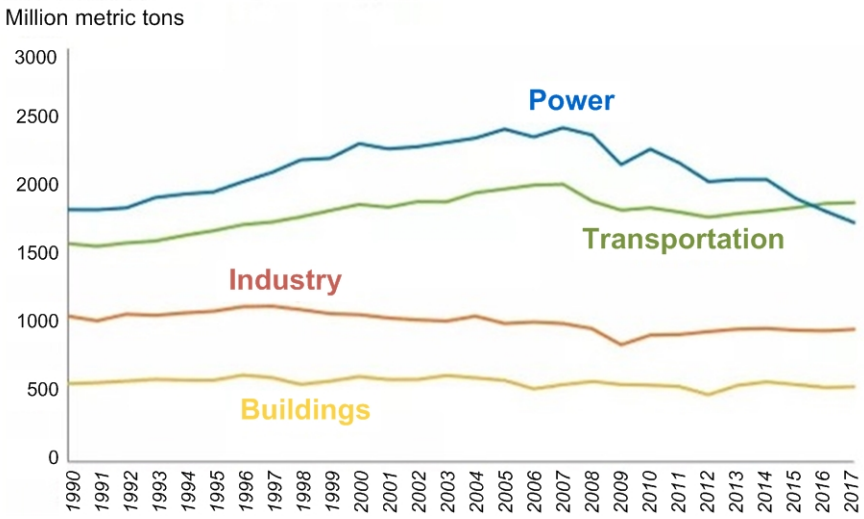

Figure 1.1: *Energy related CO_2 emissions per sector, from 1990 up until 2017 expressed in million metric tons[2]*

Simultaneously, passenger safety has been increasing as well, resulting in stricter requirements for the crash-worthiness of cars. Compared to the 1950s, the fatality risk (for occupants) decreased by 56% in 2012 [3]. Even though the safety is increased by clever design and improved vehicle architecture, the material choice also plays an important role. Naturally, the yielding behaviour during impact is largely defined by the choice of material. Traditionally in automotive industry, conventional steels were used for most of the structural and aesthetic components. In recent years the use of aluminum alloys and next-generation ferrous alloys has increased, as a result of further developed metallurgical knowledge on the processing and manufacturing. Modern advanced high-strength steels (AHSS) offer the benefits of high specific strength combined with improved ductility, along with excellent weldability and formability. These properties are sought-after in automotive industry and have further fueled interest. In Figure 1.2 AHSS is put into perspective with other (traditional) steel alloys.

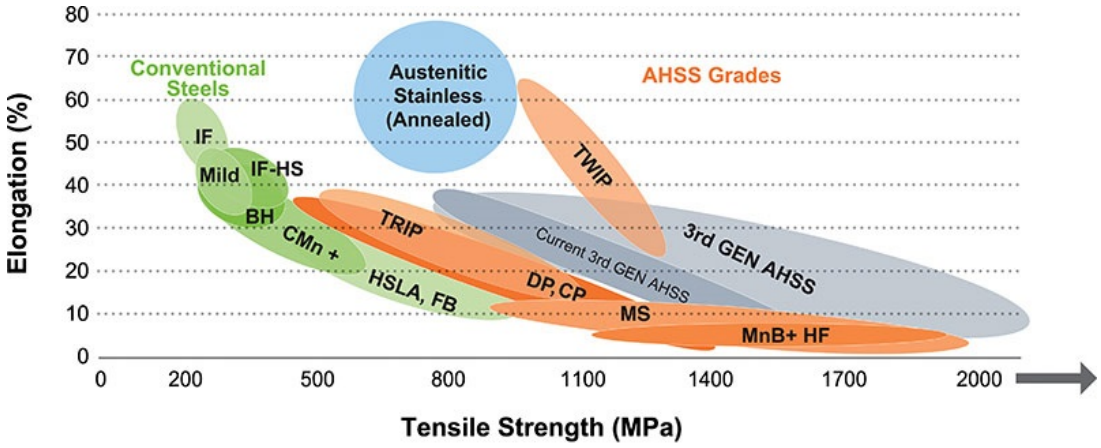

Figure 1.2: *Elongation versus tensile strength chart comparing AHSS alloys to conventional steels [4]*

1.2 Problem statement

Despite the apparent increase in strength and ductility of AHSS, some problems may arise during sheet metal forming operations. Unexpected edge-cracking is a commonly encountered issue that cannot be predicted with global formability parameters obtained from regular tensile testing. Instead, the theory of fracture mechanics is applied to rationalize cracking-related problems during forming. Figure 1.3 shows two common types of defects.

(a) Edge-cracking after forming

(b) Cracking after folding of a crash-rail

Figure 1.3: *Two types of cracking-related defects found often in automotive AHSS applications* [5]

Fracture mechanics essentially describes the material resistance to crack propagation for a flawed geometry, as illustrated in Figure 1.4. Different experimental methods i.e. fracture toughness testing methodologies exist to characterize cracking resistance of different types of materials, such as [6][7]:

- Crack-tip opening displacement testing
- J-integral testing
- K_{Ic} testing
- Kahn tear tests

These established methods are widely used in engineering practices and standardized in ASTM (American Society for Testing and Materials), ISO (International Organization for Standardization), or BS (British Standards) norms. Generally speaking, these methods require highly-experienced technicians to prepare samples and conduct (time-consuming) experiments.

In recent literature there is an increasing interest in the Essential Work of Fracture (EWF) methodology of fracture toughness testing with thin (below 2.0 mm) double-edge notched tensile (DENT) specimens of [7][8][9][10][11]. The method received much attention in automotive industry due to its relative simplicity, which means it could potentially be implemented in routine testing.

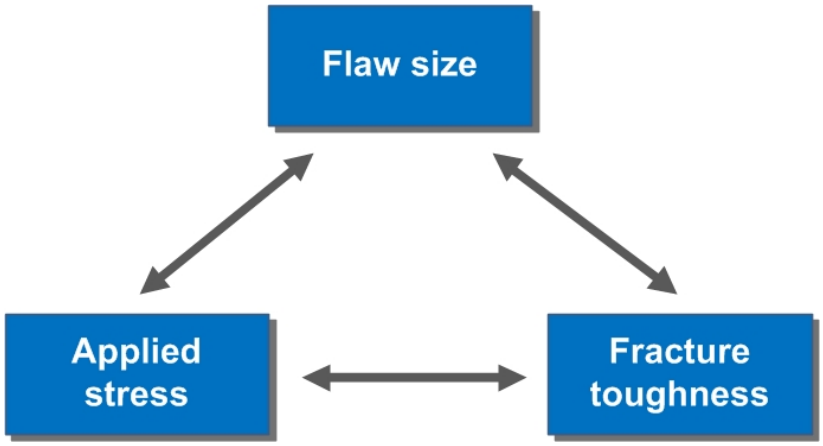

Figure 1.4: *Fundamental relations of fracture mechanics*

In addition to purely testing, the role of the microstructure in the fracture mechanics is non-trivial. Identification of the micro-mechanisms that control the fracture toughness are critical and can be fed back to production of the steel. Based on metallurgical knowledge, the fracture toughness can potentially be improved accordingly.

1.3 Research goals

The goal of this thesis is to develop a fracture toughness test for AHSS based on the Essential Work of Fracture methodology, using a novel sample preparation method of sheared notches rather than fatigue pre-cracks. The research questions are defined as follows:

1. Is the novel method of sheared notches a feasible method to create DENT specimens of intermediate thickness (between 2.0 and 4.0 mm) AHSS suitable for EWF testing?
2. How does this sample preparation method compare with fatigue pre-cracking, in terms of robustness and accuracy for EWF testing?
3. What is the influence of the initial flaw size on the EWF results and observed cracking behaviour during forming?
4. Can the EWF methodology be applied to understand and predict edge-cracking behaviour during industrial forming processes?
5. Can the EWF method be used to reveal the intrinsic micro-mechanisms of failure that govern the fracture toughness properties?

6. Is the EWF method suitable to be implemented as a routine 'material release test' to reveal and identify deterioration of fracture toughness properties, within an acceptable experimental time-frame?

1.4 Outline

In the following chapter background information is given on automotive applications of AHSS and the types of defects that are often encountered. Also the different types of AHSS and HSLA are explained along with the common fracture mechanisms in metallic materials. In Chapter 3 the investigated materials are presented along with the experimental methods applied. Here, the novel method of sheared notches is described along with the theory behind the essential work of fracture. The results are presented and discussed in Chapter 4. This chapter is subdivided into the different experiments, whereas the essential work of fracture results are separated into the three different initiation methods and are presented per material. Finally, the conclusions are given with respect to the formulated research questions. After that a list of recommendations is provided to expand and improve the fracture toughness experiments as well as the fundamental knowledge behind it.

2. Background

2.1 Automotive applications

As mentioned in the introduction, the safety and efficiency of consumer cars is an increasingly important selling point. Increased public environmental awareness contributes to this trend. Modern cars are already composed of 30-40% AHSS due to the additional safety it offers compared to conventional high-strength steels steels [12]. In regions where energy absorption from a potential impact is critical, it can offer a weight reduction due to its superior specific properties. Steel providers claim various advantages when applying AHSS in consumer vehicles[12]:

1. A weight reduction of 25 - 39% (compared to conventional steels)
2. A 5% reduction in greenhouse gas emissions
3. Good recyclability

Generally speaking about crashworthiness, components are required to either (plastically) deform substantially in order to absorb energy maximally or deform very little to protect the passengers. This distinction leads to different AHSS grades and characteristics, which are applied very differently in the car architecture. In the next sections more information is given about these different grades of materials.

In Figure 2.1 the body-in-white of a typical passenger car is shown with the different (safety) components indicated. The safety cell, which is essentially the confined space wherein the passengers are seated, belongs to the second class of materials as explained above. More specifically, the safety cell consists of vertical pillars (A, B, C/D pillars), lateral roof beams, corner joint supports and the roof panel itself. This design protects passengers in case of frontal/side impact and in case of roll-over whereby intrusion from the bodywork of the car is potentially lethal [13]. On the other hand, the crumple zones, which are designed to absorb energy as much as possible and dampen deceleration during impact, belong to the first class of materials. These components therefore deform considerably and in a controlled manner. This component is highlighted in Figure 2.1. The result of combining these two design approaches is illustrated in Figure 2.2, where the crumple-zone is clearly crushed and deformed while the passenger in the safety cell is relatively unharmed. Similarly, in Figure 2.3 the body-in-white of the 5-star Euro NCAP (highest score) awarded Volvo XC40 is shown with the different grades of AHSS (and more conventional steels) used. This approach has effectively led to the increase of occupant-safety as well as to other road users, and at the same time minimized emissions by lightweighting. Thin sheet metal is extensively used here, and by optimizing the sheet thickness safely, weight is saved in the construction.

2.2 Defects in manufacturing

Considering that the AHSS arrives in sheet metal coils, different forming operations are required to process the material into the desired shape and geometry. The sheets are cut to size, hydraulically press-formed or deep-drawn, trimmed down, and in the end joined together by means of welding/brazing/mechanical fastening. It is a well-known fact in industry that the forming of AHSS sheets instead of traditional alloys presents additional challenges, such as [14][15][16]:

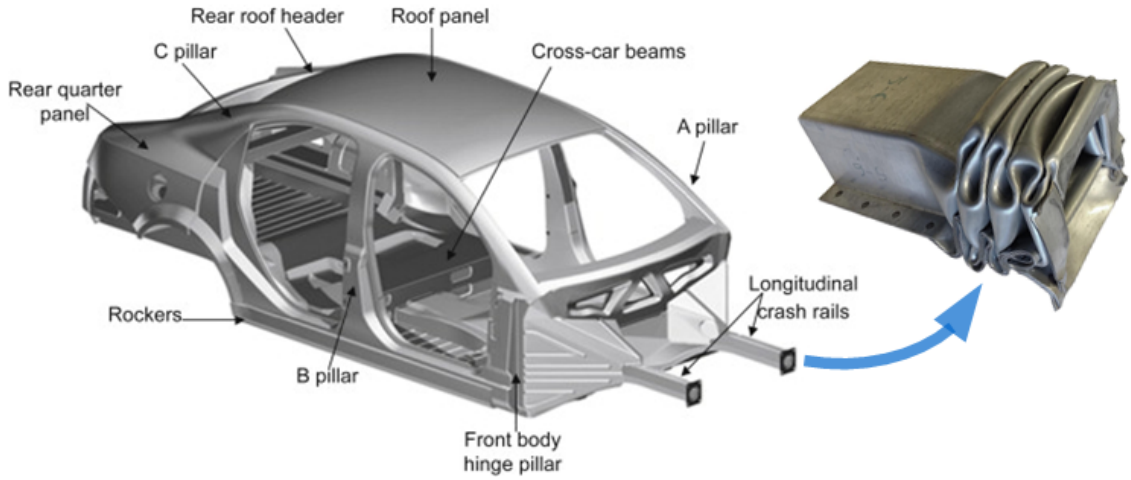

Figure 2.1: *Body-in-white architecture, showing a deformed crumple-zone member with the intended collapsing and folding deformation. Adapted from: [17][18].*

Figure 2.2: *Crash-test results of a 2017 Dodge Durango SUV during a small-overlap frontal crash[19].*

1. Increased springback of the blank and out-of-plane twisting, especially in deep-drawing applications
2. Increased tendency to wrinkling, requiring more blankholder pressure between the press
3. Increased press and tool deformations, causing shape deviations and potential product failure
4. Damage to the tooling, e.g. excessive wear and plastic deformation
5. Different blank failure mechanisms with more localized failure, due to the microstructural characteristics

There exist several straightforward solutions to tackle some of the above-mentioned problems. Accurate process control is key, as usual. For example, the application of the proper lubricants with the correct operating temperatures and viscosity can effectively decrease friction between the blank and tooling. Frictional forces depend heavily on local pressure fields, which is often a source of mechanical failure (i.e. tearing, cracking). To decrease springback effects, drawbeads are added in the die which induce extra plastic stretching of the blank. At the same time, manufacturing engineers spend months touching-in the tooling to optimize blank flow. Wrinkling on the other hand is often times decreased by applying more blankholder pressure. However, the required blankholder pressure

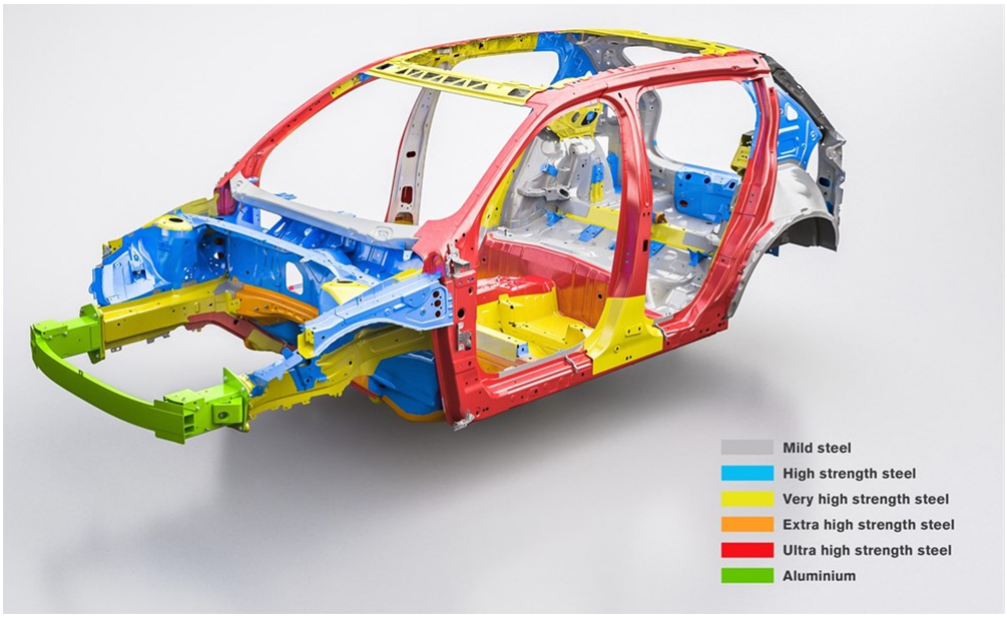

Figure 2.3: *Architecture of a 2018 Volvo XC40 cross-over, which was awarded 5 stars in Euro NCAP (highest score) due to its effective use of Ultra High-Strength Boron steel in the safety cage. Image courtesy of Volvo Cars, Sweden.*

must be within press limits, which can be a challenge with AHSS. Computer Aided Engineering (CAE) predictions are useful tools to assist in the design stage and prevent problems in the prototyping stages. Unfortunately, highly accurate predictions are not feasible yet for complex forming operations.

Blanking and trimming operations also suffer from additional challenges. AHSS exhibits higher work hardening coefficients, which can lead to higher strength and hardness in sheared/punched edges. Such conditions near the edges create susceptibility to cracking, in addition to surface defects such as burrs. Burrs act as unsafe stress raisers at the edges, which can often lead to unexpected failure. Ideally, the sheared/punched edges have smooth transition zones with no burrs, voids, secondary shear or other damages. Some grades of AHSS consist of ferrite and islands of martensite that have a much higher hardness and strength, which can act as stress-raisers as well. In general, the AHSS grades exhibit higher resistance to plastic deformation compared to traditional steels, which results in higher tool and press deflections, which in turn demands higher operating forces from the processing equipment. Methods involving lasers, milling, water-jets or electrical discharge machining (EDM) introduce very little to no work hardening at all, making them the preferred methods especially in AHSS. More details on the microstructures and linked behaviour is provided in the next paragraphs. [20]

There are several points of action that can prevent the issues mentioned earlier. Firstly, the tool geometry in punching operations plays an important role. By using a bevelled punch rather than a flat design, the maximum shear force can be reduced significantly along with a decreased edge cracking tendency [21]. The correct punch clearance can also effectively reduce secondary shear, burrs and voids in the final product. Tool-coatings are also an important measure against premature failure due to wear and abrasion. The type of coating that is required is defined by the strength of the AHSS grade, the coating on the steel, the complexity of the process and the number of parts that need to be produced [20].

In Figure 2.4 a collection of manufacturing defects are collected as described above. As a general recommendation, it is advised to regularly inspect the microstructure of sheared or cut edges to assess their condition and as a tool to optimize the process itself. As mentioned in the introduction, this research focuses on the issue of edge-cracking such as in Figure 2.4d.

(a) Wrinkling

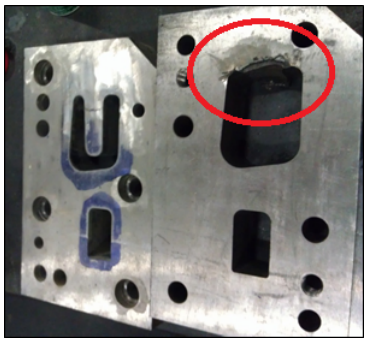

(b) Wearing of tools

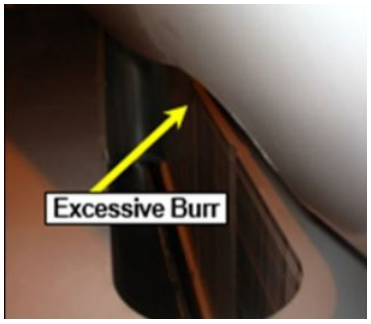

(c) Burring

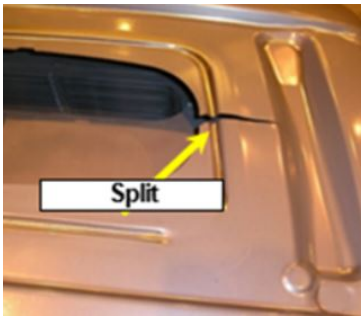

(d) Splitting

Figure 2.4: *Four types of manufacturing defects often found in AHSS [20][22]*

From the material-development point of view, it is important to investigate where fracture toughness testing can contribute to the understanding of cracking-related problems. Traditionally, forming limits (local necking limit) are used to predict failure in sheet metal forming, expanded with ductile fracture limits. These methods rely on fracture criteria that assume the generation of microscopic flaws during monotonic loading (examples are given in the next paragraph). However, these methods do not incorporate an initial flaw in the geometry, as is the case with fracture mechanics approaches. Recent literature [23] suggests that a correlation between the fracture toughness and edge ductility can be found, by predicting the crack propagation resistance once a notch or crack is formed. Such cracks originate from areas with large amounts of plastic deformation, e.g. compressed corners after bending. The onset of crack growth is often found during reversed deformation in these areas i.e. elastic springback. It is important to consider that fracture toughness testing is performed on undeformed material, therefore the accumulated plastic deformation in already formed material needs to be kept in mind.

While conventional steels (in green in Figure 1.2) have established metallurgical solutions and the behaviour of these materials is well understood, AHSS grades are more complex and not easily predictable. Multiple alloying and processing solutions can be considered in order to improve either the strength or ductility (or both). While the continuum properties appear very similar (global strength and ductility) the microstructural solutions selected might result in tremendous differences in fracture toughness (as will be shown in the Results).

2.3 Steel grade variations

Single-phase grades

One of the investigated steels is of a commercially available single-phase grade, developed and produced by Tata Steel IJmuiden, denoted as (HR) XPF1000-UC/GI. It is a hot-rolled steel intended for automotive purposes such as engine sub-frames, chassis and suspension components, axles and similar. The steel offers a very competitive combination of strength and ductility to enable further lightweighting and safety improvement of vehicles. Due to the mechanical properties of the steel, it is eminently applicable to complex forming applications, hence the product-range name 'XPF' (e**X**tra **P**rocessing **F**ormability). The tensile strength is roughly 1000 MPa but is also available as 800 MPa, depending on the amount of precipitation (the grain size is not varied).

The obtained strength is derived from a novel metallurgical concept of nano-precipitation, which can elevate the ferrite grains to much higher strengths while maintaining sufficient ductility. A single-phase microstructure is chosen as it eliminates the large (local) strength-differentials encountered in multi-phase steels, especially in dual-phase ferritic-martensitic grades, which can often act as promoters of failure through induced strain-localisation and microvoid-nucleation [24]. Instead, (coherent) nanoprecipitates throughout the matrix increase the strength of the material by increasing the resistance to shear deformation in the presence of a moving dislocation. The hardness of these intermetallic particles is much higher than the surrounding ferrite. Figure 2.6 shows the distribution of nanoprecipitates in the matrix. As a result of the dislocations movement through the grains, dislocation loops (sometimes referred to as 'Orowan loops') are created around the precipitates. As a result, the dislocation increases in length. The strength-gain, or 'bowing' stress $\Delta\tau$, is calculated by the Orowan equation below:

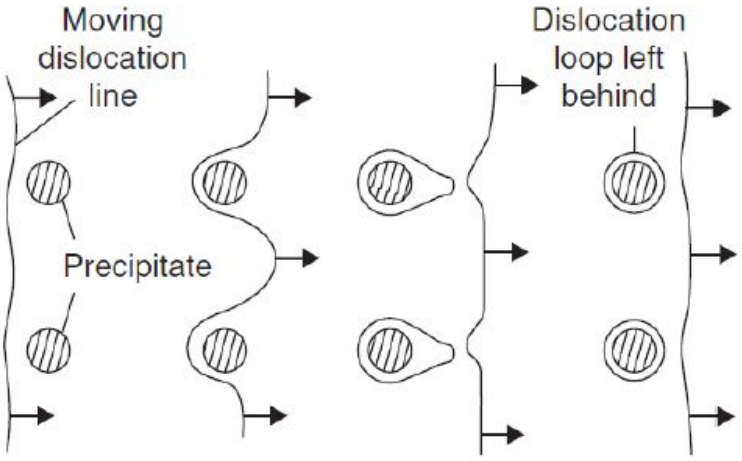

Figure 2.5: *Precipitate-dislocation interactions by Orowan loops [25]*

$$\Delta\tau = \frac{Gb}{L-2r} \tag{2.1}$$

Where G is the shear modulus, b the size of the Burgers vector, L the inter-particle spacing and r the radius of the particles. Although the equation assumes a simplified representation of reality, it can be derived that $\Delta\tau \propto r^{-1}$; a metallurgical effect which is taken advantage of in these steels.

The creation of the precipitates depends on carefully controlling the processing conditions and the available elements in the steel. Table 2.1 shows the chemical composition of the XPF800 and XPF1000 grades. The tensile properties of XPF800 are given in Table 2.2; the tensile properties of XPF1000 are measured separately as part of this research (see: Chapter 4.1).

Table 2.1: *Chemical composition of the XPF steel grades (maximum values shown) expressed in wt%.* [26]

Alloy	C	Mn	Si	P	S	Al	Cr+Mo	Nb+Ti	V	B
HR XPF800-UC	0.08	1.7	0.5	0.02	0.05	0.015-0.1	0.3	0.2	0.03	0.008
HR XPF1000-UC	0.13	1.7	0.5	0.02	0.05	0.015-0.1	0.4	0.1	0.4	0.005

Table 2.2: *Tensile properties of XPF800-UC (3.2 mm thickness) with a specimen gauge length of 50 mm. Values are given parallel to rolling direction (L-T) and perpendicular to rolling direction (T-L).[27]*

Orientation	$R_{p0.2}$ [MPa]	R_m [MPa]	ε_u [%]	ε_t [%]
T-L	781	833	8.4	14.4
L-T	730	820	9.4	16.9

As the materials cools down, the aim is to subject the steel to $\gamma \rightarrow \alpha$ phase transformation only, and to promote the formation of nanoprecipitates with coiling between 600 - 650 $^{\circ}$C. Molybdenum (Mo) is added to achieve a fine-grained and damage-resistant ferrite microstructure. Simultaneously, Mo lowers the interphase velocity at the γ/α-interface which promotes interphase precipitation (seen in Figure 2.6, bottom-right) while acting as a carbide former in the precipitation process. Niobium (Nb) and Vanadium (V) are selected as precipitating elements for both the strength-gains as well as the grain-refinement. Typical compounds that are then formed in these alloys are e.g. (NbVMo)CN. The maximum strength-gain by precipitation is obtained by balancing the carbon- and nitrogen amounts with carbide- and carbonitride forming elements. As a result, the added strength by precipitation is estimated to be around 300 MPa and 450 MPa for XPF800 and XPF1000, respectively. Figure 2.6 shows the single-phase microstructure, as well as the precipitates.

Application-wise, the XPF grades were primarily designed to outperform other multi-phase alloys in a combination of hole-expansion capacity (HEC), yield strength and tensile elongation. Figure 2.7 shows the results compared to other steel alloys. While the yield strength and tensile elongation represent fundamental material properties in uniaxial loading conditions, hole-expansion testing simulates the (more realistic) sheet-metal forming conditions combined with punched edges. Altogether, it can be said that XPF alloys outperform the multi-phase alloys in terms of the weight-saving potential, or increased in-service performance at an equivalent gauge.

Dual phase grades

Dual phase (DP) steels are among the first variations of AHSS to have been invented. Typically the two phases involved are ferrite and martensite, which results in a low yield strength due to the ferritic phase combined with a high tensile strength due to the martensitic phase. The desired microstructure is achieved by annealing in the intercritical region, promoting the formation of austenite and ferrite. Afterwards, a rapid quenching step causes the carbon-rich austenite to transform into martensite. DP steel contains roughly 0.1wt% carbon, varying slightly. The investigated dual phase steel is a commercially available cold-rolled DP1000 grade produced by Tata Steel IJmuiden with an (ultimate)

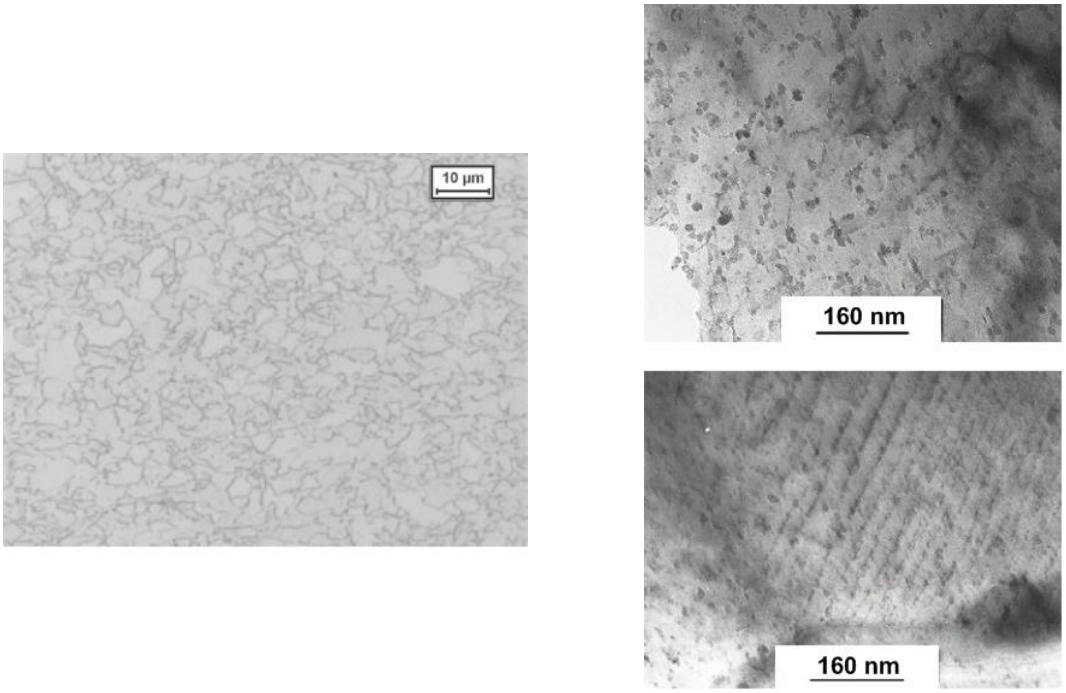

Figure 2.6: *Micrograph showing the single-phase ferrite microstructure (left) and TEM bright field images showing random precipitates (top-right) and interphase precipitates (bottom-right) [24].*

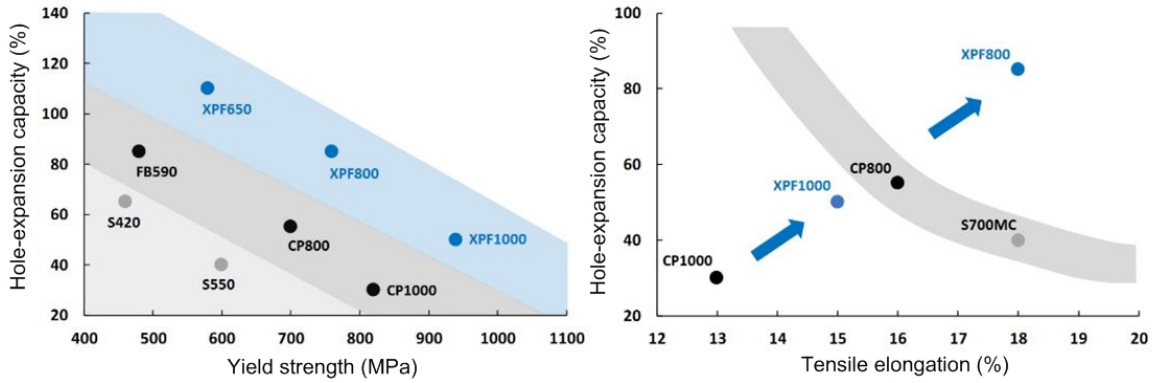

Figure 2.7: *HEC vs. yield strength for XPF and other multi-phase alloys (left) and HEC vs. tensile elongation for XPF and other alloys (right) [24].*

tensile strenght of roughly 1000 MPa, denominated as DP1000-GI (zinc-coated). The tensile properties of the DP1000-GI grade used in this project are collected in Table 2.3.

Naturally, the grain size, morphologies and relative volume fractions of both phases determine the mechanical response (among other things). Furthermore, they exhibit very high (initial) work-hardening rates. This effect is useful for forming operations as it results in a stronger material afterwards, improving the fatigue and crashworthiness properties. This advantage is further exploited to use thinner-gauge materials. In Figure 2.8a a micrograph from a scanning electron microscope (SEM) is shown, revealing the microstructure of a DP steel. DP steels typically have a tensile strength in the range of 500-1000 MPa, and a total elongation before fracture of up to $\sim$30%.

Table 2.3: *Tensile properties of DP1000-GI (2.0 mm thickness) with a specimen gauge length of 80 mm. NB orientations are given in ASTM fracture toughness notation: tranverse T-L and longitudinal L-T.*

Orientation	$R_{p0.2}$ [MPa]	R_m [MPa]	ε_u [%]	ε_t [%]	Lankford coefficent r [-]
T-L	788	982	5.5	11.6	0.89
L-T	750	980	6.2	11.7	0.73

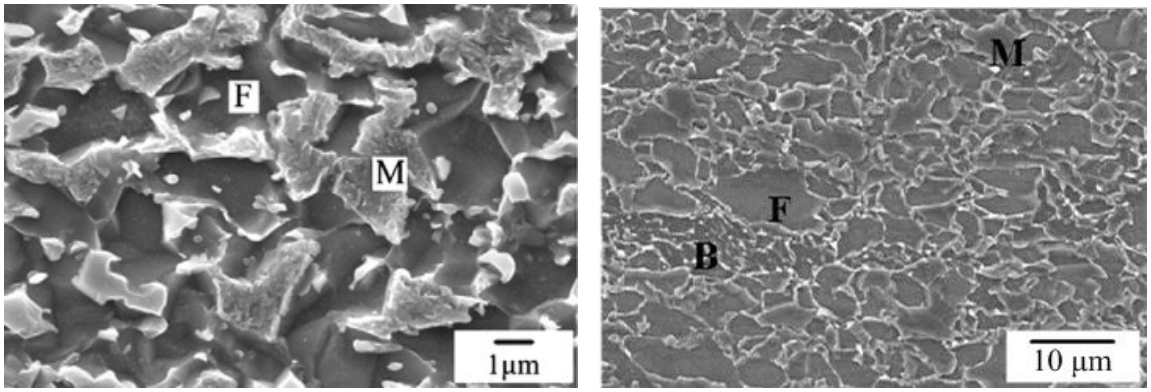

(a) Dual-phase [28] (b) Complex-phase [29]

Figure 2.8: *SEM images of DP steel (left) and CP steel (right). The darker ferrite matrix (F) can be distinguished from the lighter martensite phases (M). Bainite (B) is revealed by small martensite islands in a ferrite matrix.*

Complex phase grades

Complex phase (CP) steels contain several phases, in contrast to just two in DP. Ferrite and bainite, combined with smaller amounts of martensite, pearlite and retained austentite typically form the microstructure. The microstructure is very refined, which is obtained by the addition of alloying elements such as vanadium and titanium that can suppress grain growth. The carbon content is also slightly higher, with roughly 0.15wt%. The microstructure is illustrated in Figure 2.8b.

Compared to DP steels, the tensile strength is slightly higher (800-1200 MPa) while compromising on ductility (approx. 7-15%). As a result of the microstructure, the work hardening rate is lower compared to DP, making it slightly less suitable for complex forming operations. Overall, it is considered an improvement over HSLA steels with its superior strength. In Figure 2.9 the difference between the mechanical response of DP and CP is illustrated by comparing two similar-strength grades. The investigated steel are two (slightly different) commercially available hot-rolled 800 MPa grades (3.3 mm and 4.0 mm thickness) produced by Tata Steel IJmuiden and are referred to as CP800-UC. They consist out of a fine bainitic matrix with martensite phases, pearlite/cementite phases and ferrite phases. The uniaxial tensile properties are listed in Table 2.4 below.

High-strength low-alloy grade

Before the introduction of AHSS, high-strength low-alloys (HSLAs) were the most prevalent type of steel used in high-strength automotive applications. These steels contain low amounts of carbon ($< 0.25\%$) and other alloying elements to promote grain refinement and/or precipitation to increase

Table 2.4: *Tensile properties of CP800-UC (3.3 mm thickness) with a specimen gauge length of 80 mm. Values are given parallel to rolling direction (L-T) and perpendicular to rolling direction (T-L).*

Orientation	$R_{p0.2}$ [MPa]	R_m [MPa]	ε_u [%]	ε_t [%]
T-L	723	819	5.8	10.3
L-T	661	787	6.8	11.5

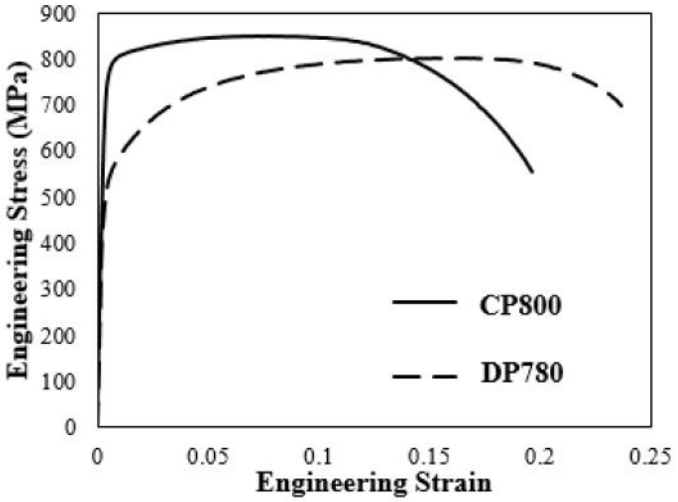

Figure 2.9: *Tensile test results for a CP800 and DP780 steel in transverse direction (strain rate $\dot{\varepsilon} = 0.003\ s^{-1}$[30].*

the strength. Niobium (Nb), vanadium (V) and titanium (Ti) are often used for this purpose. As with the XPF steels, niobium and vanadium are chosen as they are strong carbide/nitride formers that can hinder grain growth during cooling-induced phase transformations and create precipitates. Mangenese (Mn) is mainly added for solid solution strengthening. Unexpected cracking is far less frequently observed with these steels, and is an interesting comparison with the aforementioned AHSS grades. The chosen HSLA is a hot-rolled Ympress S550MC grade with a tensile strength of roughly 660 MPa and a thickness of 3.0 mm. The chemical composition is given in Table 2.5 and the mechanical properties in Table 2.6. Microstructurally it consists of a fine ferritic matrix with fine carbides/cementite concentrated at the grain boundaries.

Table 2.5: *Chemical composition of the Ympress S550MC steel grades (maximum values shown) expressed in wt%.* [31]

Grade	C	Mn	Si	P	S	Al	Ti
Ympress S550MC	0.1	1.65	0.03	0.003	$\geq$0.015	0.09	0.06

2.4 Fracture mechanics and failure

Stresses at the crack-tip

The failure modes observed in steels can be separated into two basic types: *brittle* failure, and *ductile* failure. The type of failure depends on multiple aspects, such as the applied load, temperature, strain

Table 2.6: *Tensile properties of Ympress S550MC (3.0 mm thickness) with a specimen gauge length of 80 mm. Values are given parallel to rolling direction (L-T) and perpendicular to rolling direction (T-L).[27]*

Orientation	$R_{p0.2}$ [MPa]	R_m [MPa]	ε_u [%]	ε_t [%]
T-L	645	698	11.0	18.8
L-T	643	689	11.8	20.6

rate, microstructure, and so on. Brittle failure mechanisms are distinctively different from ductile tearing mechanisms on both microscale and macroscale. The observed fracture mechanisms are explained in the third paragraph.

Ductile failure involves large amounts of plasticity occurring at microscopic grain-level, resulting in stable tearing increments i.e. crack growth, while brittle failure involves very little (highly localized) plasticity where sudden failure is very likely. This distinction is also referred to as *yielding dominant* and *fracture dominant* failure, respectively. For the simplest example, an infinitely large plate with a central (circular) hole, the maximum stress at the notch tip is raised due to the geometric irregularity (see Figure 2.10).

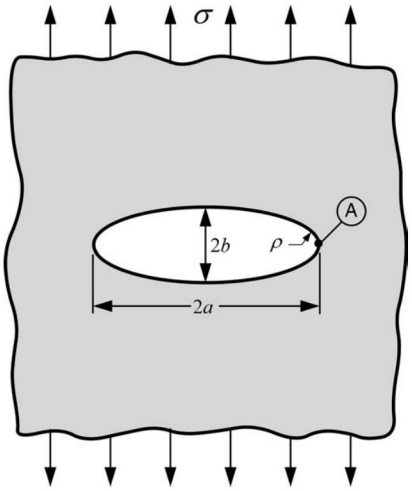

Figure 2.10: *Infinite plate with a central hole [32].*

For a circular hole it holds that $a = b$ where the curvature can be expressed as:

$$\rho = \frac{b^2}{a} \tag{2.2}$$

The maximum stress at A is then found by making use of Inglis' solution:

$$\sigma_{max} = \sigma_{app}\left(1 + 2\sqrt{\frac{a}{\rho}}\right) \tag{2.3}$$

Where σ_{app} is the nominal applied load and a & ρ the hole length and curvature, respectively. This relation is only valid for blunt notches, and approaches infinity as $\rho \to 0$ as is the case for sharp cracks. For other geometries and configurations than the shown example, the relations are similar in terms of parameter dependency. From the linear-elastic fracture mechanics (LEFM) approach, the

stress components near the *crack*-tip can be obtained in Mode I loading for a central crack in an infinite plate [32]:

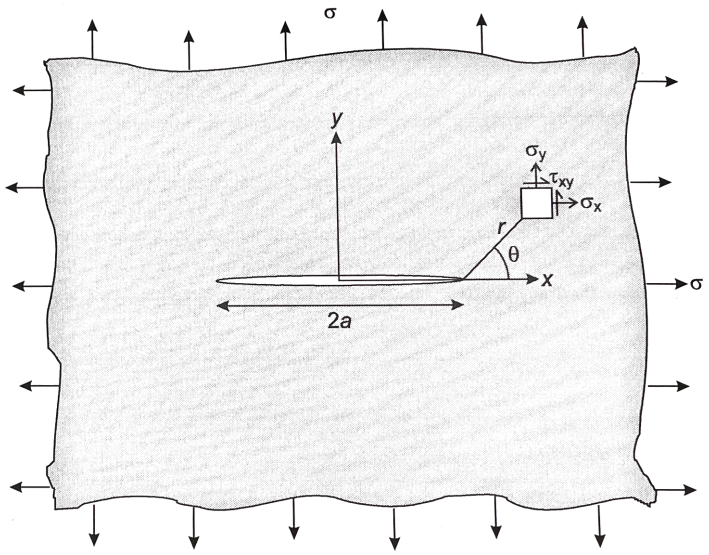

Figure 2.11: *Infinite plate with a central crack [6].*

$$\sigma_{xx} = \frac{\sigma\sqrt{\pi a}}{\sqrt{2\pi r}}\cos\left(\frac{\theta}{2}\right)\left[1-\sin\left(\frac{\theta}{2}\right)\sin\left(\frac{3\theta}{2}\right)\right] \tag{2.4}$$

$$\sigma_{yy} = \frac{\sigma\sqrt{\pi a}}{\sqrt{2\pi r}}\cos\left(\frac{\theta}{2}\right)\left[1+\sin\left(\frac{\theta}{2}\right)\sin\left(\frac{3\theta}{2}\right)\right] \tag{2.5}$$

$$\sigma_{zz} = 0 \text{ (plane stress)} \quad \text{or:} \quad \sigma_{zz} = \nu\left(\sigma_{xx}+\sigma_{yy}\right) \text{ (plane strain)} \tag{2.6}$$

$$\tau_{xy} = \frac{\sigma\sqrt{\pi a}}{\sqrt{2\pi r}}\cos\left(\frac{\theta}{2}\right)\sin\left(\frac{\theta}{2}\right)\cos\left(\frac{3\theta}{2}\right) \tag{2.7}$$

Where r and θ are the polar coordinates at the crack-tip, as defined above. These three expression also tend to infinity at an infinitely sharp crack-tip radius ($r \to 0$), also referred to as the $1/\sqrt{r}$ singularity. The intensity of this stress singularity is the *stress intensity factor* K_I and is equal to $\sigma\sqrt{\pi a}$ for this specific configuration and loading. Figure 2.12 illustrates the stress intensity solution that describes the singularity dominated zone, as well as the far-field solution that is governed by the remote boundary condition (σ_∞). An ideal material is assumed here, i.e. linear-elastic isotropic behaviour. Mode I denotes the first of the three types of loading-modes with respect to the orientation of the crack-flanks, as shown below. In Mode II and III shear stresses become dominant in the K-solution, rather than the normal stresses. [32]

As a result of finite stress-levels allowed in the material, yielding occurs inside the plastic zone at the yield strength, σ_y, assuming an elastic-plastic response (no strain hardening). This limitation results in a re-distribution of forces i.e. an increase in the effective plastic zone Δa (see Figure 2.14);

$$r_p = r_y + \Delta a \tag{2.8}$$

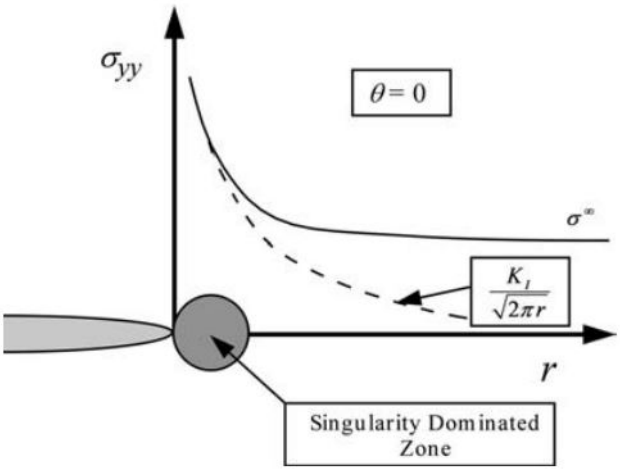

Figure 2.12: σ_{yy} *(stress component normal to the crack plane) as a function of the distance from the crack-tip r. Both the far-field solution and the singularity-dominated zone are shown.[32]*

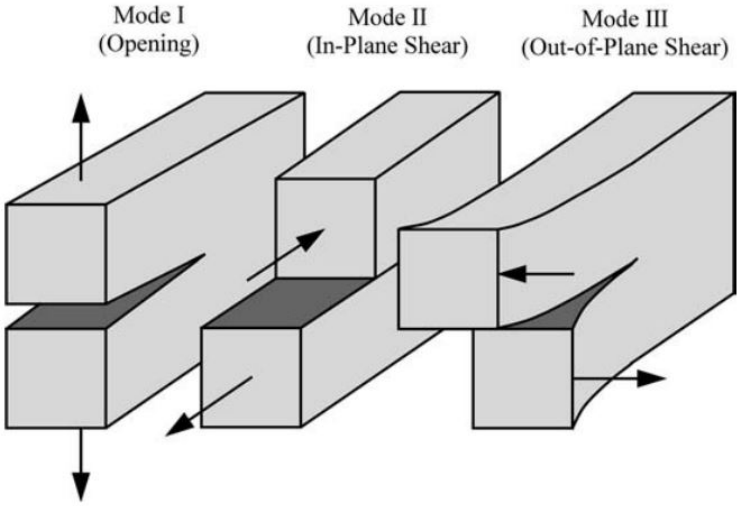

Figure 2.13: *Different loading modes in cracked geometries.*

Where r_y represents the first-order estimate of the plastic zone size and r_p the second-order estimate, taking plasticity into account. Using the solution for stress intensity the plastic zone size can then be calculated:

$$r_p = \frac{1}{\pi}\left(\frac{K_I}{\sigma_{ys}}\right)^2 \quad \text{(Plane stress)} \tag{2.9}$$

Similarly for (ideal) plane strain condition, where the stress triaxiality limits yielding by a factor 3 (assuming Poisson's ratio $\nu = 1/3$):

$$r_p = \frac{1}{3\pi}\left(\frac{K_I}{\sigma_{ys}}\right)^2 \quad \text{(Plane strain)} \tag{2.10}$$

The above equations are valid for linear-elastic materials where the plastic zone size is small

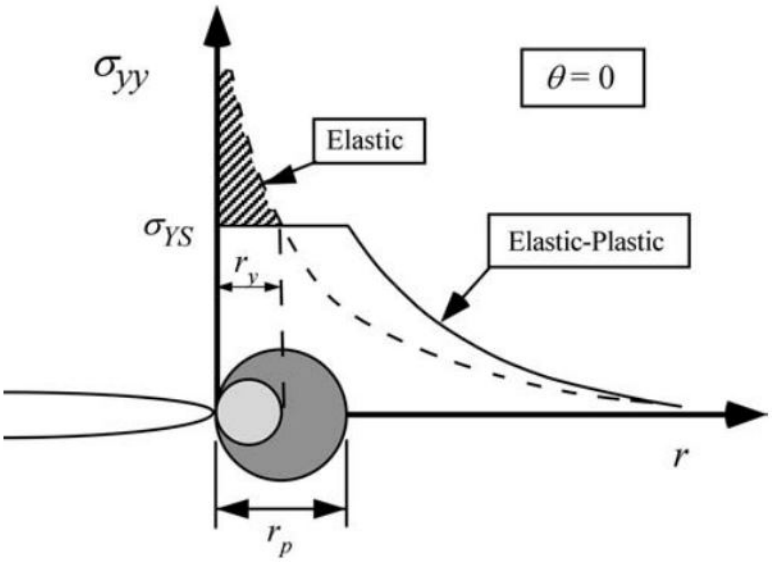

Figure 2.14: *Estimations of the plastic zone size using the purely elastic- and elastic-plastic material model (Irwin's approach) [32]*

relative to the bulk of the deforming body, therefore the global mechanical response remains in the linear regime. The distinction between pure plane strain and plane stress conditions is made by comparing the plastic zone size to the plate thickness. As a general rule of thumb found in literature [6]:

$$\text{when: } 2r_y \geq B \;\Rightarrow \text{plane stress}$$

$$\text{or: } 2r_y \leq \frac{B}{10} \;\Rightarrow \text{plane strain}$$

It must be stated that materials in practice often experience a combination of both stress states, referred to as plane stress-plane strain transitions. Actually, true plane-stress is only achieved at the free surfaces of the plate as there is always *some* degree of stress triaxiality (see Figure 2.15). The stress triaxiality is defined as:

$$\eta = \frac{\sigma_h}{\sigma_{eq}} \tag{2.11}$$

Where σ_h is the hydrostatic stress given by:

$$\sigma_h = \frac{\sigma_{xx} + \sigma_{yy} + \sigma_{zz}}{3} \tag{2.12}$$

And σ_{eq} is the Von-Mises equivalent stress:

$$\sigma_{eq} = \sqrt{\frac{1}{2}\left[(\sigma_1 - \sigma_2)^2 + (\sigma_1 - \sigma_3)^2 + (\sigma_3 - \sigma_2)^2\right]} \tag{2.13}$$

Finite-element calculations show that the actual plastic zone shape in Mode I is different from the earlier assumed circle, and depends strongly on the strain-hardening coefficient n and the elastic-plastic boundary i.e. when yielding actually takes place. When the Von-Mises yield criterion is

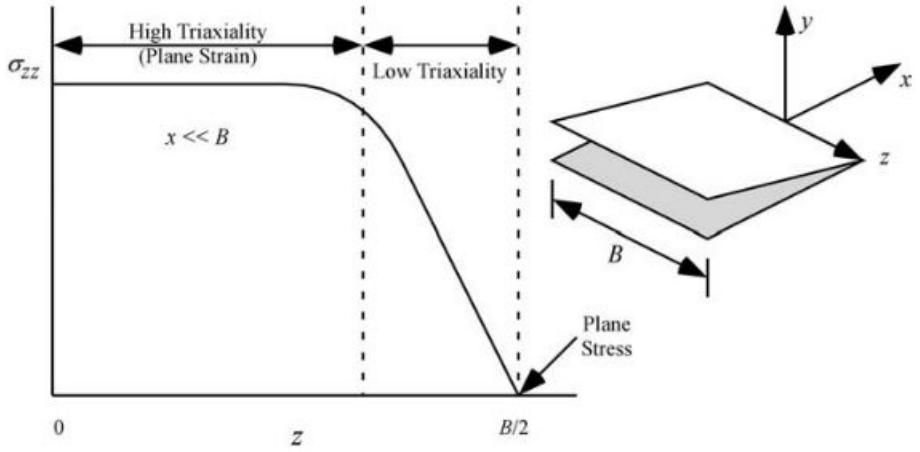

Figure 2.15: *Variation of σ_{zz} (stress in thickness direction, reflecting the degree of stress-triaxiality.[32]*

assumed and the elastic-plastic boundary is set at $\sigma_{eq} = \sigma_{YS}$, the plastic zone size is severely underestimated when compared with a purely-elastic material model. When defining yielding at an effective stress 8% lower, it significantly increases its size. As for strain-hardening: a high strain-hardening coefficient promotes the potential of stress absorption inside the material and consequently reduces the plastic zone size, as there is less need to re-distribute the forces in the vicinity of the crack-tip. Both effects are illustrated below.

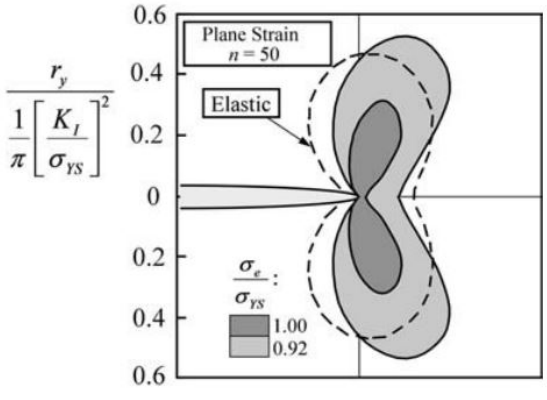

(a) Effect of the elastic-plastic boundary $\frac{\sigma_{eq}}{\sigma_{YS}}$ [33]

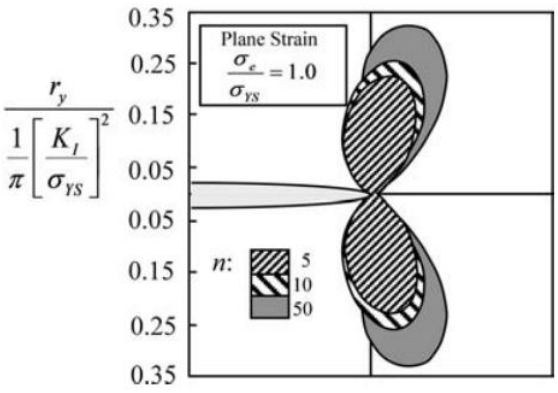

(b) Effect of strain-hardening coefficient n [32]

Figure 2.16: *Parameters affecting the (plane strain) plastic zone size- and shape, obtained from finite-element analysis.*

When the plasticity increases up to the point that the deforming body does not behave linearly anymore, elastic-plastic fracture mechanics (EPFM) takes over. Although this approach yields more accurate results for some cases, the elegant analytical solutions are lost and more complex experimental methods and numerical models are required instead.

Crack-tip plasticity and microstructure

Focusing on the events inside the plastic zone reveals the mechanisms at grain-level that allow for plasticity. At the root of the crack-tip, a local stress intensity factor K_{eff} is activating a dipole source that sends either (i) shielding dislocations that move towards the grain boundary or (ii) anti-shielding dislocations that move towards the crack-tip. The elastic fields from dislocations either increase the effective stress intensity factor K_{eff} at the crack tip (anti-shielding dislocations) or decrease it (shielding dislocations). The former cause dislocation pile-up at the grain boundary, while the latter are annihilated at the free surface of the crack-tip and cause blunting. Dislocation pile-ups are also responsible in triggering new dislocation sources (Frank-Read source) in the neighboring grain when the critical resolved shear stress (τ_{crss}) is reached i.e. $\tau = \tau_{crss}$, thus developing more plasticity. In short, crack-tip plasticity consists of these three steps:

nucleation of dislocations ⇒ gliding through the crystal ⇒ interaction with obstacles

In Figure 2.17 a schematic illustration is shown. Two relevant length-scales can be identified: the mean free path for dislocation glide (δ), and the dislocation source spacing along the crack front (λ). This explanation only accounts for plasticity through dislocation-glide though (e.g. no twinning deformation). [34] [35]

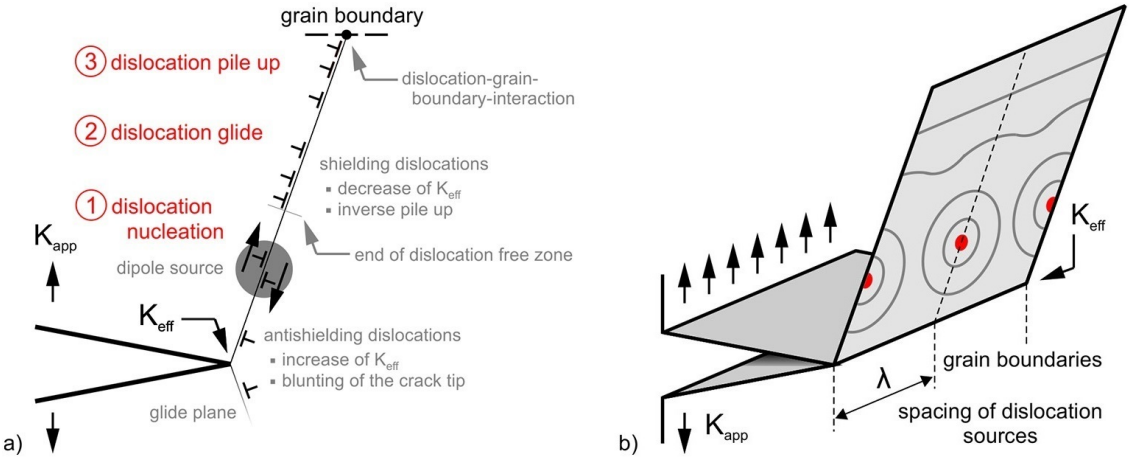

Figure 2.17: *Schematics of crack-tip plasticity and associated dislocation mechanisms. Onset of fracture occurs at $K_{eff} = K_{Ic}$. Adapted from:[35]*

The role of grain boundaries in crack-tip plasticity is apparently twofold:

1. They act as dislocation motion barriers, creating dislocation pile-up that limits crystal plasticity.

2. They provide a dislocation nucleation source where the grain boundaries intersect with the crack front.

Recalling the Hall-Petch equation, as presented below, the effect of grain-size on the yield strength can be estimated;

$$\sigma_y = \sigma_0 + \frac{k}{\sqrt{d}} \tag{2.14}$$

Where σ_0 represents the lattice friction stress, k the Hall-Petch strengthening coefficient and d the grain size. Similarly, the grain size effect on crack-tip plasticity can be applied to estimate the fracture toughness. For equiaxed grains wherein the mean distance of intersection points of grain

boundaries with the crack front is measured by the aformentioned λ (i.e. dislocation nucleation happens 'externally' at the grain boundaries), the following relation is found[34]:

$$K = K_0 + \frac{k}{\sqrt{d}} \tag{2.15}$$

This equation is actually identical to the Hall-Petch equation shown before. When λ is better measured by the mean distance of intrinsic sources along the crack front (i.e. dislocation nucleation happens inside the grains), the relation changes into [34]

$$K = K_0 + \frac{k\sqrt{\delta}}{\lambda} \tag{2.16}$$

This transition occurs at a critical grain size, whereby the first regime (relatively small grain size) finds an increase in fracture toughness with decreasing grain size, and in the second regime (relatively large grain size) the fracture toughness decreases with grain size. See Figure 2.18 below.

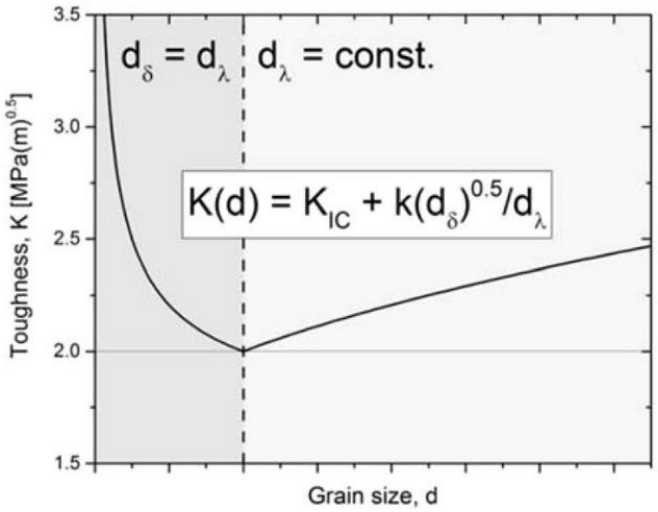

Figure 2.18: *Analytical relation between toughness and grain size. In the first regime (dark grey)* $\lambda = \delta$ $(d_\lambda = d_\delta)$ *while* λ (d_λ) *is constant in the other regime (light grey) [34]*

This relation explains the minimum often found in fracture toughness at a specific grain size. Similarly, the effect of λ and δ together with the encountered obstacle force at the grain boundary Φ is shown in Figure 2.19 (for the small-grain size regime). It again shows the inverse relation between grain size and toughness, as well as a negative relation with the obstacle force. The positive effects of smaller grains are diminished when the grain boundary obstacle is higher.

The crystal structure also largely determines the opportunities for plasticity through the available slip-systems. In principle, both a BCC- and FCC lattice have 5 linearly independent slip-systems required for plasticity (as the strain tensor $\bar{\bar{\varepsilon}}$ has 5 degrees of freedom). However the slip-planes in the FCC configuration are truly close-packed and require less energy (heat activation) to move along the slip direction. Therefore FCC metals behave much more ductile and do not experience a ductile-to-brittle transformation at a certain temperature. The slip systems are listed in Table 2.7. HCP crystal systems are not further discussed as they are irrelevant to the materials under investigation.

Apart from the inherent crystal anisotropy induced by plasticity (because slip occurs only on the preferred slip-planes, it causes re-orientation to these 'stable positions'), anisotropy is introduced by

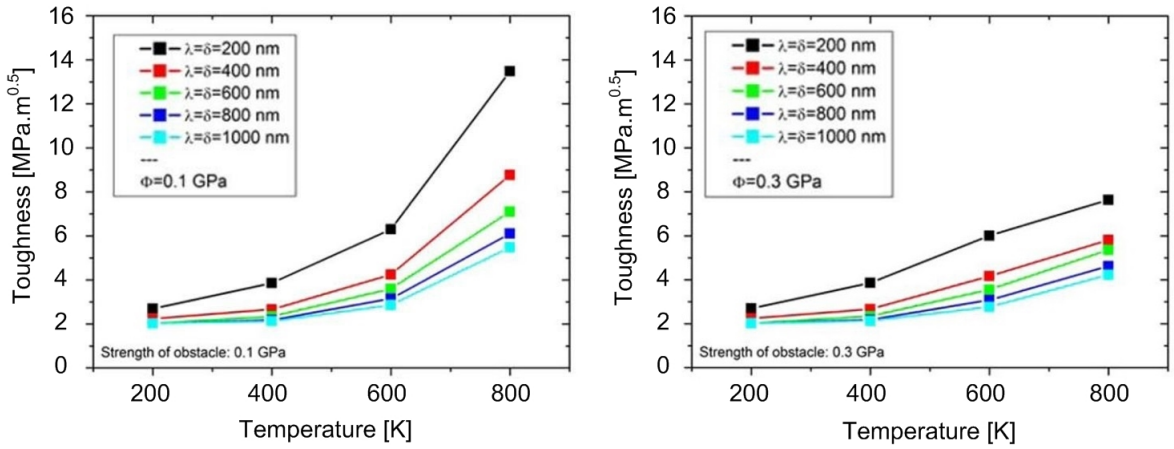

Figure 2.19: *Effect of mean free path λ, dislocation source spacing δ and the obstacle force Φ on the fracture toughness, based on numerical simulations. [34]*

Table 2.7: *Slip-systems in a face-centered cubic (FCC), body-centered cubic (BCC) and hexagonal close-packed (HCP) crystal lattice.*

Crystal structure	Slip-system	Possible combinations	Close-packed plane
Body-centered cubic (BCC)	$\{110\}\langle 111\rangle$	12	No
	$\{112\}\langle 111\rangle$	12	No
	$\{123\}\langle 111\rangle$	24	No
Face-centered cubic (FCC)	$\{111\}\langle 110\rangle$	12	Yes
	$\{100\}\langle 10\bar{1}\rangle$	12	Yes
Hexagonal close-packed (HCP)	$\{0001\}\langle 11\bar{2}0\rangle$	3	Yes

rolling reduction. It is well-known that grains are flattened during rolling and lose the earlier assumed equiaxed character. As a result, grains are distorted to a certain aspect ratio, which can be expressed as the ratio between the chord length in the minor- and major axis a and b, respectively:

$$\text{Aspect ratio} = b/a \tag{2.17}$$

As the grains distort more heavily (aspect ratio increases), the mean-free path decreases, resulting in earlier dislocation pile-up at the grain boundary. This prevents the generation of new dislocations from the source, effectively reducing the toughness. The relation between the cord length a and mean-free path of dislocations in the case of a parallel crack (relative to RD) is given by [34]:

$$2\delta = a/\sin(70.5^{\circ}) \tag{2.18}$$

Furthermore, the mean-free path increases with the length of b in the case of a perpendicular crack relative to RD. See Figure 2.20. For these two configurations the effect of grain distortion on the toughness is numerically evaluated in Figure 2.21. Clearly the positive effects of grain elongation are only valid when the crack is perpendicular to the rolling direction, due to the increase mean-free path length δ. When the energy barrier to emanate dislocations from- and to the crack-tip is too high, chemical bond-breaking takes place which is the mechanism of brittle fracture, rather than ductile tearing. This failure mechanism is thus activated when there is no opportunity for plasticity.

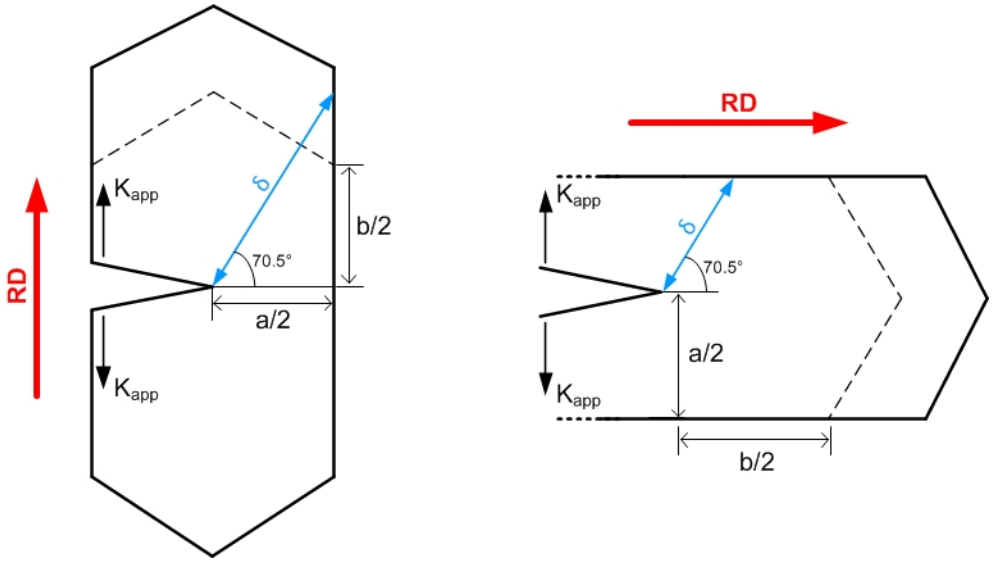

Figure 2.20: *Effect of grain shape parameters on the mean-free path for dislocation glide, causing anisotropy. Left: crack is oriented transverse to the rolling direction. Right: crack is oriented longitudinal to the rolling direction. Adapted from: [34]*

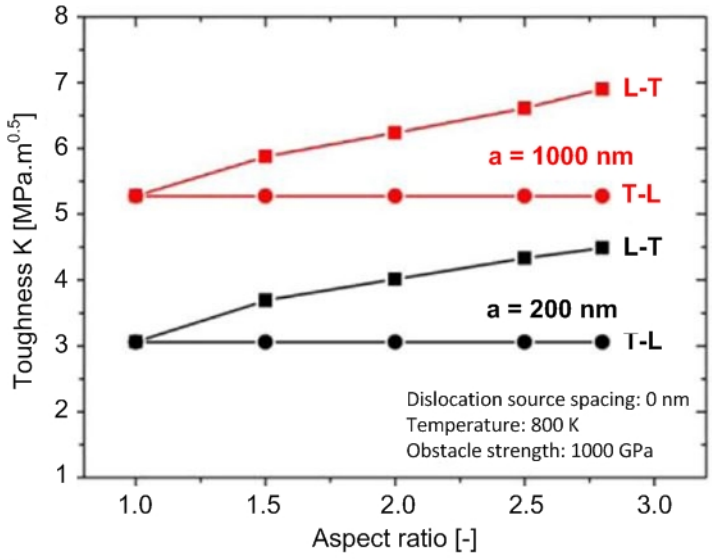

Figure 2.21: *Toughness as as function of grain aspect ratio for two grain sizes. L-T and T-L configuration stand for a perpendicular crack relative to RD and parallel to RD, respectively (left and right in Figure 2.20). [34]*

Fracture mechanisms

While materials in engineering practices often display a mixed-mode failure comprising both brittle- and ductile failure modes, the two are treated separately here for the sake of clarity. The fracture paths can also be split up: transgranular (through the grains) or intergranular (along the grain boundaries). In common practice, ductile fracture is controlled by *microvoid coalescence* while brittle fracture occurs via *(transgranular) cleavage*.

Microvoids coalescence happens through microvoids that nucleate at various locations inside the lattice, such as intermetallic particles and precipitates that introduce a certain discontinuity in the lattice. With increased loading, voids can grow in size depending on the orientation. Small and large voids (or equally sized voids) can co-operate in the formation of a fracture surface, by crack linkage. The size of the particle determines the size of the void through which cracks can connect and grow (see Figure 2.22). Ductile failure can thus be divided into three parts:

$$\text{void nucleation} \Rightarrow \text{void growth} \Rightarrow \text{void coalescence}$$

Upon complete failure, the fractured surfaces reveal the phenomenon of microvoid coalescence through dimples. The type of loading (tensile, shearing or tearing) can also be deduced from the dimple formation. An example of a dimpled fracture surface is shown below in Figure 2.23a.

For some AHSS grades containing relatively high concentrations of carbon-rich martensite, intergranular fracture is also an observed fracture mechanism. For example in DP steels, delamination of ferrite and martensite at the interface creates voids that can grow and coalesce. The strength differential between the ferrite and martensite is responsible for this behaviour, causing DP steels to be more sensitive to void nucleation compared to CP steels for example where the strength differentials are smaller. Transgranular fracture can occur due to martensite cracking sooner than the ferritic matrix, which acts as a void nucleation site. Less common causes of void nucleation are hard TiN-particles, although it has been reported in literature for both DP and CP steels to cause interface de-cohesion between phases. [36]

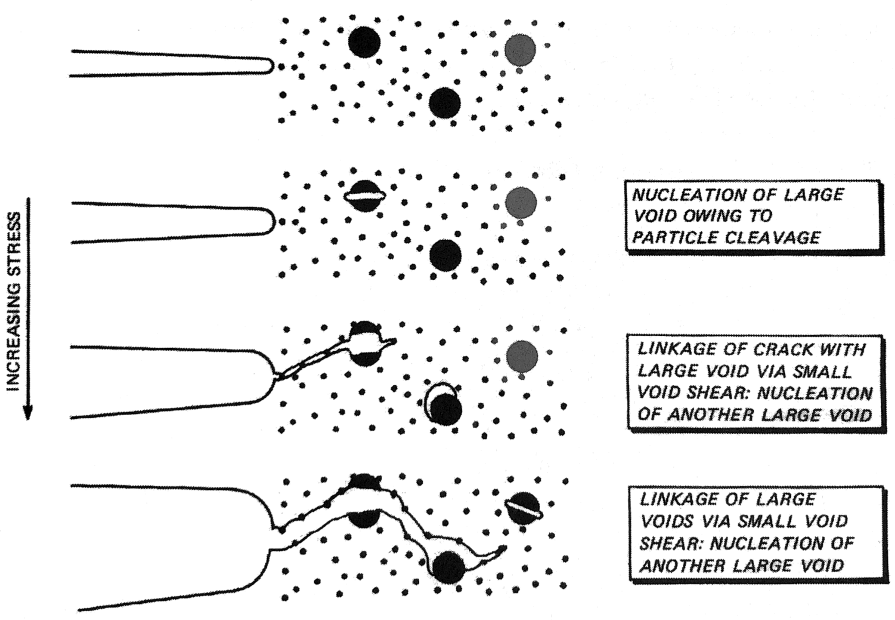

Figure 2.22: *Crack evolution as a result increased stress and microvoid coalescence.[6]*

The occurence of microvoid coalescence can be predicted with models for void nucleation. A critical decohesion stress σ_c is defined accordingly, as a combination of two stress-contributions [37]:

$$\sigma_c = \sigma_{eq} + \sigma_m \tag{2.19}$$

Where σ_{eq} is the equivalent Von-Mises stress and σ_m is the mean stress defined as the sum of the principal stresses:

$$\sigma_m = \frac{\sigma_1 + \sigma_2 + \sigma_3}{3}$$

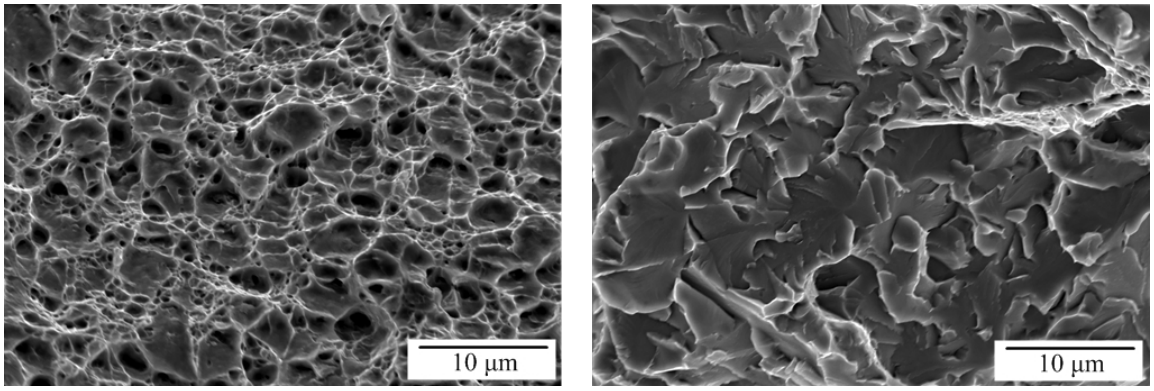

(a) Microvoid coalescence (b) Transgranular cleavage

Figure 2.23: *SEM images showing the ductile and brittle fracture mechanisms in steel.*

According to this model, the void nucleation strain decreases as the hydrostatic stress increases. Thereby suggesting that void nucleation is more prominent when there is a stress triaxiality, something that is observed also in experimental data [32]. This model only accounts for particle-matrix debonding, neglecting void nucleation sites such as cracked particles (think of oxide inclusions and other larger particles that can crack prematurely).

A well-known void growth model is derived by Rice and Tracey, and assumes a single circular void in an infinite solid (that grows elliptically). Resulting in a semi-empirical relation [38]:

$$\ln\left(\frac{\bar{R}}{R_0}\right) = 0.283 \int_0^{\varepsilon_{eq}} \exp\left(\frac{1.5\sigma_m}{\sigma_{YS}}\right) d\varepsilon_{eq}^p \tag{2.20}$$

Where $\bar{R}/R_0$ represents the void growth in three-dimensional space, and ε_{eq}^p is the equivalent Von-Mises plastic strain. Note that this model assumes one single void, therefore no void-interaction is included. Fracture by void coalescence is therefore not predicted, but can be substituted by a critical value for the void radius for instance. Other (more complex models) have been developed with more predictive capabilities, such as the Gurson-Tvergaard and Thomason model [39].

When eventual crack growth takes place, a tunneling-effect is often observed in the center of the plate due to the high stress-triaxiality here (see Figure 2.24). Recall the positive effects of stress-triaxiality in the void-nucleation process. Typically, the growth- and coalescence of voids is the limiting factor, occuring much closer to the (blunted) crack-tip where the stress-levels are higher. Shear lips are found at the edges of the plate, at a 45^o angle with respect to the maximum principal stress. This is caused by the nucleation of voids along the angled deformation bands. The shear fracture-zone lags behind the flat fracture through the middle. The ratio shear/flat-fracture increases with decreasing specimen thickness, up to the point where shear fracture is the only observed type. [32]

Transgranular cleavage fracture on the other hand involves the breaking of bonds through the grains. The resulting fracture surface exposes the grains, as shown in Figure 2.23b. Typical for cleavage is the formation of river patterns. These are the result of brittle crack-propagation whereby the encountered grain boundary is slightly misoriented to a certain twist-angle, therefore the crack planes are split up in parallel and eventually recombine to a common plane after a certain distance (to reduce energy). This process is illustrated schematically in Figure 2.25 and a close-up example is shown in Figure 2.26. Cleavage fracture initiation is most commonly caused by inclusions and

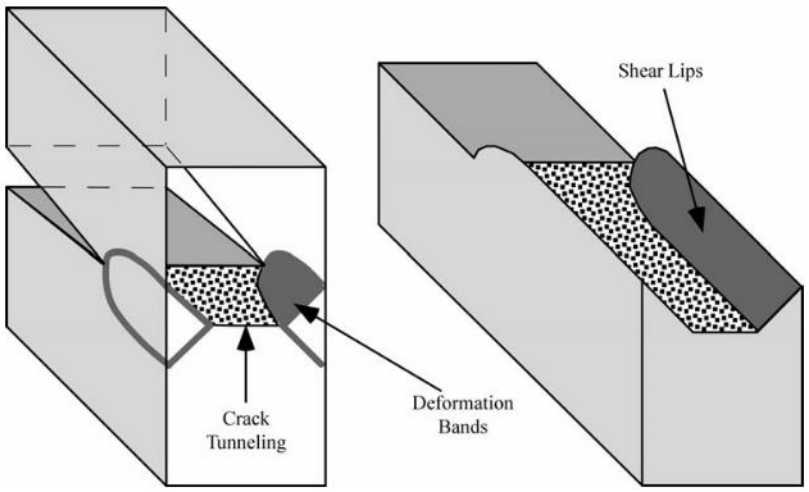

Figure 2.24: *Ductile crack growth leading to crack tunneling at the center, and shear lips at the edges due to deformation bands.[32]*

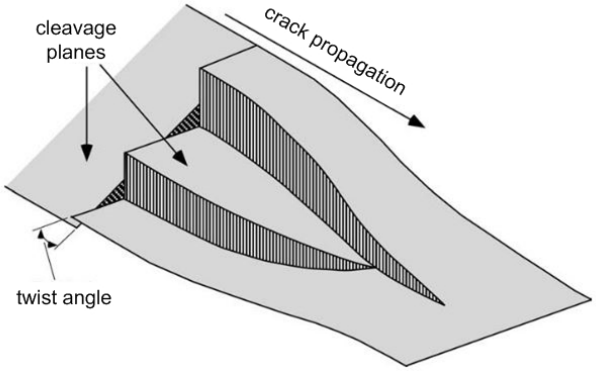

Figure 2.25: *River pattern formation. [32]*

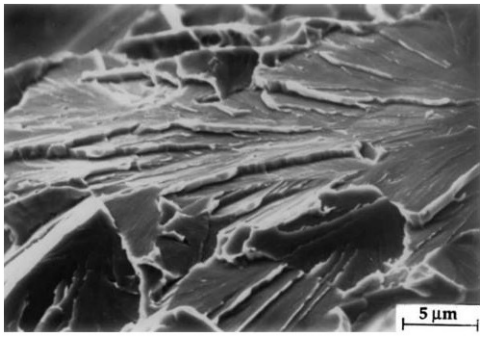

Figure 2.26: *Example of river patterns in a A508 Class 3 steel. [32]*

second-phase particles. These particles experience the elevated stress- and strain levels near the crack-tip which causes the particles to crack first. If the stress is sufficiently high, these newly created microcracks can grow into the surrounding matrix. See Figure 2.27. For this simplified case with a spherical particle creating a penny-shaped crack, the fracture stress σ_f can be derived[32]:

$$\sigma_f = \sqrt{\frac{\pi E \gamma_p}{(1-\nu^2)C_0}} \tag{2.21}$$

Where γ_p is the plastic work required to create a unit area of fracture surface in the ferrite matrix and C_0 the particle diameter. Particle-cracks do not necessarily lead to macroscopic fracture; crack arrest can occur which halts the crack at a grain boundary for example. The source of cleavage fracture initiation can vary among steels with different microstructures and cannot be easily predicted with such models only. It is however established that factors such as: low temperature, stress triaxiality, high strain-rate and strain-aging, which all tend to increase the yield strength, increase the susceptibility to cleavage fracture as well[32].

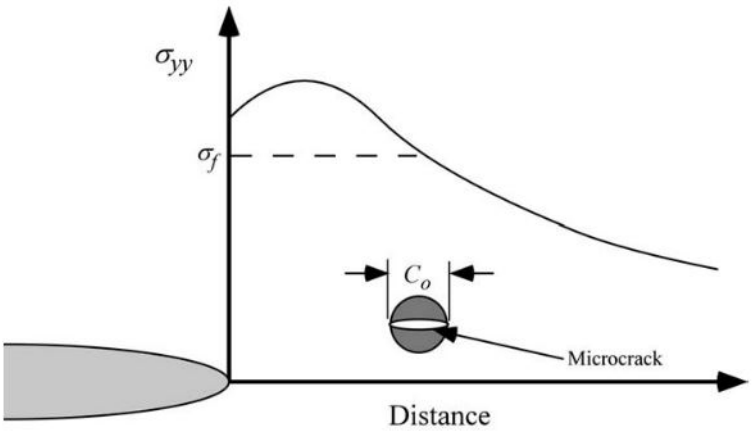

Figure 2.27: *Cleavage crack initiation due to second-phase particles [32]*

If the initiation of brittle fracture depends on the premature fracture of non-primary particles, then the distribution of these particles near the crack-tip determines the required amount of plasticity for fracture, and thus the observed fracture toughness. For instance, two fracture toughness specimens taken from neighboring material in the same coil of steel can show significant dissimilarity. This can be explained by the difference in the frequency of 'fracture-triggering particles' near the crack-tip. As this phenomena is of statistical nature, it leads to a lowered (observed) fracture toughness as the thickness of the sample increases. A probability tree is given in Figure 2.28 which illustrates the weakest-link mechanism that controls cleavage initation [40] [41] [42]. Reality shows that actual observed fracture often comprises both brittle- and ductile-type fracture phenomena. In the Results chapter, several examples will be brought forward.

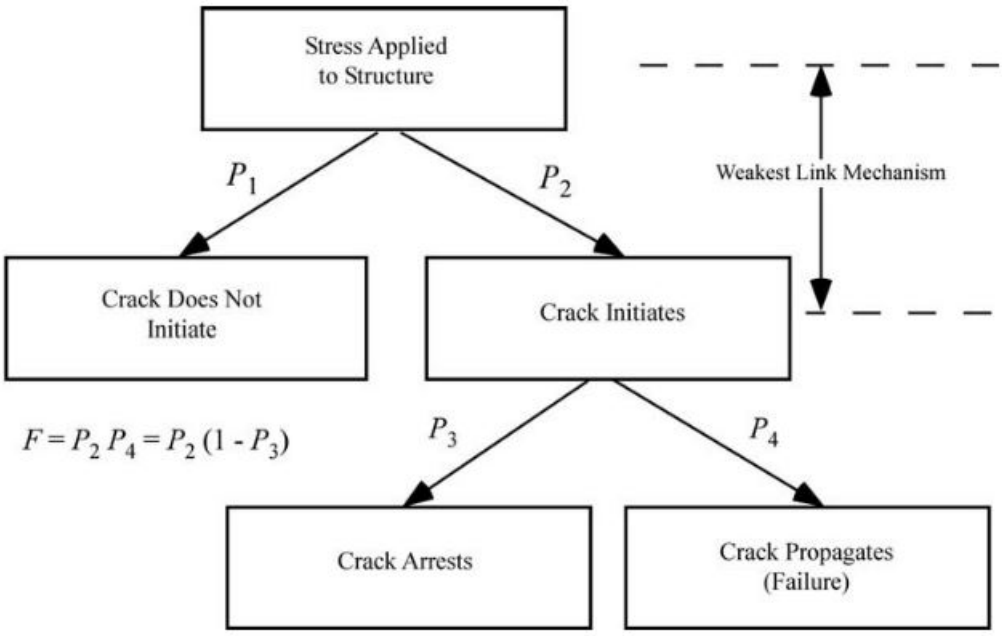

Figure 2.28: *Probability tree for cleavage initation and propagation that result in failure (F). [32]*

Apart from stretching, bending loads can also lead to similar fracture behaviour. During hot-rolling, voids can form near inclusions close to the tension surface (for example) which can coalesce outwards, thus forming a crack. Spinel ($MgO{\cdot}Al_2O_3$), alumina (Al_2O_3), and a mixture of calcium aluminate ($CaO{\cdot}Al_2O_3$) and spinel are commonly found inclusions in DP steels[43]. These particles can also break during bending of the steel, depending on the relative strength of the particle. It has been found that when the particles are much stronger than the steel matrix, the void formation is more pronounced[44]. Figure 2.29 shows the effect of an inclusion in a bent specimen. Here it can be seen that the inclusion has neighboring voids on either sides, and that these are surrounded by a larger region wherein more brittle-like cleavage fracture is observed. This is often referred to as a 'fish-eye' morphology. This brittleness is induced by trapped hydrogen, which can enter the material via different paths (annealing, acid picking, welding, and other H_2 sources). Although this phenomenon is found across numerous AHSS grades, the effect is found to be most prominent when the proximity of inclusion is more towards the tension surface[43]. Therefore in sheet metal designed to withstand bending loads, it is essential to control all processes carefully to minimize such impurities, especially near the free surfaces.

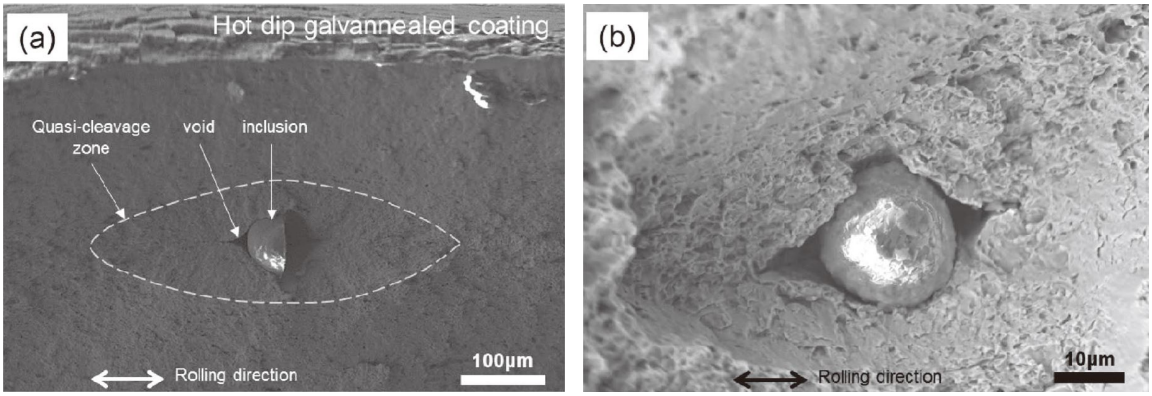

Figure 2.29: *SEM images of an inclusion found near the steel surface. Voids are formed parallel to the rolling direction, surrounded by a quasi-cleavage zone wherein brittle-like fracture is observed[43].*

Other research has shown that dynamic loading, rather than quasi-static loads, often activate the same basic failure mechanisms as described above. It must be noted however, that certain parameters such as the temperature, strain rate and inertia affect the individual stages (void nucleation, growth and coalescence). Proper experimental investigation is therefore required to validate models and to fully capture the fracture behaviour under dynamic loading conditions.[45] [46]

The creation of sheared edges, such as in stamping or punching operations, can create burrs and micro-cracks at the edges (recall the previous paragraphs). These can act as initiation points of fracture during sheared-edge elongation. Similarly, elastic strain reversal during springback can also cause edge-cracks to grow during forming. It is important to recognize the effect of locals strain-hardening on the ductility of the material, as it can increase the edge-cracking sensitivity. Among the investigated materials the strain hardening coefficient varies significantly, which can play in role in the observed fracture toughness.

3. Materials and methods

3.1 Materials

The different AHSS and HSLA grades that were introduced and explained in the Background chapter are subjected to different experiments including tensile testing, fracture toughness testing and (laboratory scale) deep-drawing. Various types of steels are investigated here, namely single-phase (XPF), dual-phase (DP), complex-phase (CP) and an HSLA (S550MC). The mechanical properties were given in section 2.3. The chosen experiments were selected based on company interest and material availability. In Table 3.1 the materials are listed together with the performed experiments.

Table 3.1: *List of materials and performed experiments.*

Material	Thickness	Tensile testing	Fracture toughness testing	Deep-drawing
XPF800-UC	3.2 mm	✓*	✓	✓
XPF1000-UC	1.8 mm	✗	✓	✗
XPF1000-UC/GI	2.7 mm	✓	✓	✗
XPF1000-UC	2.9 mm	✓*	✓	✓
DP1000-GI	2.0 mm	✓*	✓	✗
CP800-UC	3.3 mm	✓*	✓	✓
CP800-UC	4.0 mm	✗	✓	✗
S550MC-UC	3.0 mm	✓*	✓	✓

(*Not as part of this research)

The relevant testing methods and procedures are explained in the next sections, along with a detailed overview of all evaluated specimens. The corresponding results are presented and discussed in Chapter 4.

3.2 Tensile testing

Sample preparation

The fundamental tensile properties of the XPF1000 grades are measured with A50R tensile test specimens, machined according to Figure 3.1. All tensile tests were done on 2.7 mm thick samples. The specimens received a speckle-pattern coating on one side for digital-image correlation (DIC) measurements, and black (non-reflective) high-emissivity paint for infrared measurement on the other side. Figure A5 (Appendix A.2) shows a photo of both sides of the sample. A list of all evaluated samples is given below in Table 3.2.

Experimental setup

The tests were conducted on a Dartec 100 kN testing machine equipped with a GOM 3D digital image correlation (DIC) system (35 mm lenses). The test procedure consisted of a two-step program with regard to the machine cylinder displacement rate: (1) 1.125 mm/min until 0.75 mm relative

Total specimen length:	190 mm
Clamped width:	20 mm
Machined length:	75 mm
Gauge length:	50 mm
Gauge width:	12.5 mm
Shoulder radius:	20 mm
Tolerance:	$\pm$ 0.1 mm

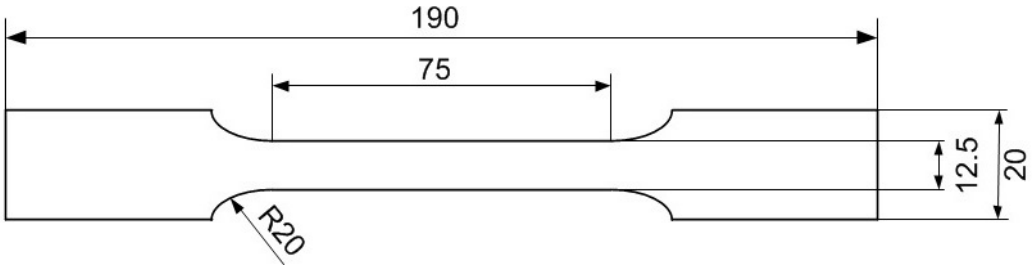

Figure 3.1: *A50R specimen geometry in mm, including the details in the table above.*

Table 3.2: *List of evaluated A50R tensile samples (orientation is given in ASTM notation to unify definitions with the fracture toughness testing). All samples were 2.7 mm thick.*

Material	From coil	Temperature	Orientation	Repetitions
XPF1000-UC	#1	20 °C	T-L	2
XPF1000-UC	#1	20 °C	L-T	2
XPF1000-GI	#2	20 °C	T-L	3
XPF1000-GI	#2	20 °C	L-T	2
XPF1000-UC	#1	60 °C	T-L	3
XPF1000-GI	#2	60 °C	T-L	3
XPF1000-UC	#1	100 °C	T-L	3
XPF1000-GI	#2	100 °C	T-L	3
XPF1000-UC	#1	100 °C	L-T	2
XPF1000-GI	#2	100 °C	L-T	2
XPF1000-GI	#3	20 °C	L-T & T-L	2
XPF1000-GI	#4	20 °C	L-T & T-L	2
XPF1000-GI	#5	20 °C	L-T & T-L	2
XPF1000-GI	#6	20 °C	L-T & T-L	2

displacement & (2) 36 mm/min until fracture. The slow initial step is chosen to capture the elastic slope accurately. The DIC system captured images at a frequency rate between 10 - 15 s^{-1}. The grid size is 0.78 x 0.78 mm^2 (square). The tests were done at elevated temperatures as well, as this is both demanded from the automotive industry, and relevant to compare with the ductile-to-brittle transition in the fracture toughness properties (explained later in the Results chapter). The temperature measurements from the infrared camera were validated with the readings from a thermocouple. The experimental setup is shown in Figure 3.2 and Figure 3.3. The strains are analysed with GOM Aramis (version 6.3) with an automated script [47].

For the XPF1000 grade the effects of the following parameters are measured:

1. Zinc-coating (hot-dip galvanizing process)
2. Anisotropy as a result of rolling (parallel & perpendicular to RD)
3. Variation in different coils of the same material
4. Temperature (measurements at room temperature, 60 ^{o}C and 100 ^{o}C are performed)

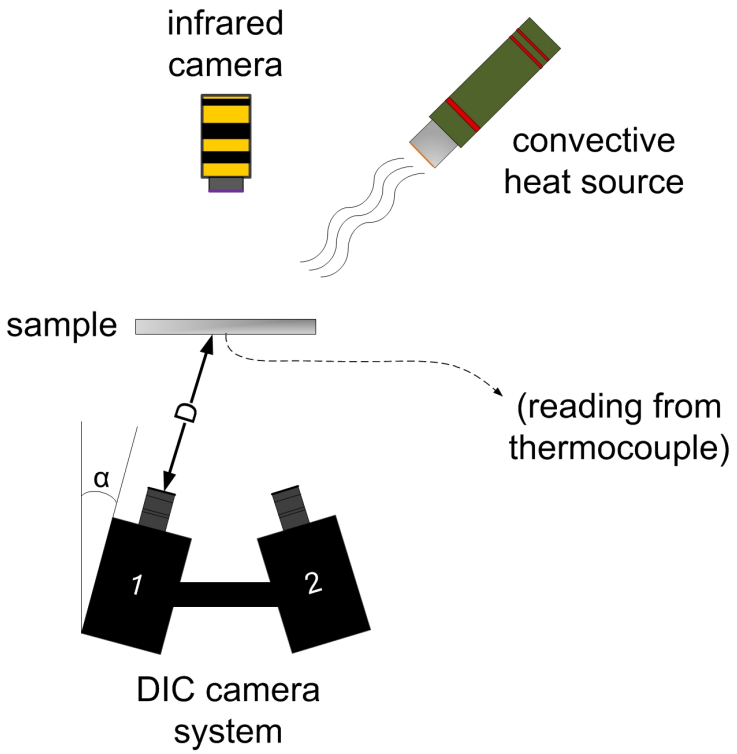

Figure 3.2: *Schematic of experimental setup with DIC and IR measurements.*

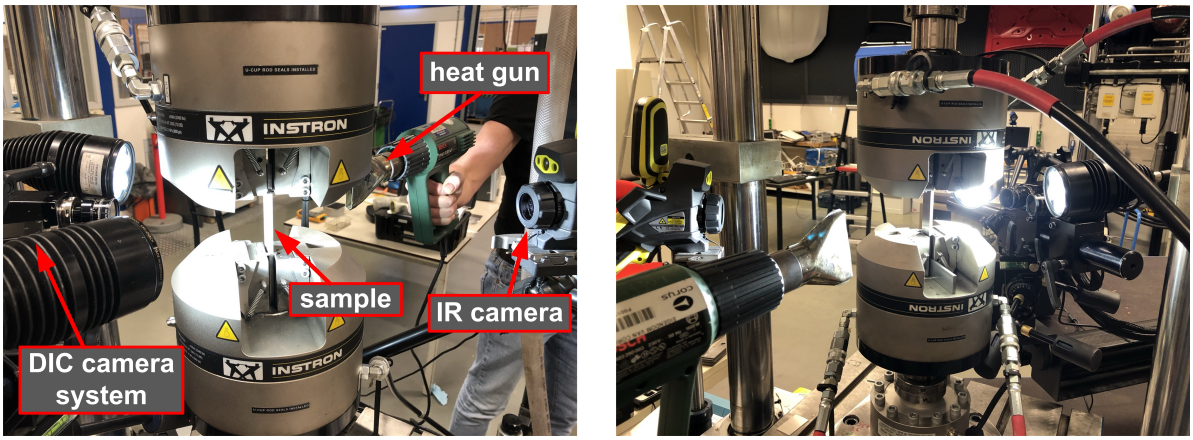

Figure 3.3: *Front & back images of experimental setup*

3.3 Fracture toughness testing

Essential work of fracture methodology

The fracture toughness testing method is based on the essential work of fracture (EWF). It has been introduced to measure the crack propagation resistance for ductile materials. It is often employed as a replacement for J-integral measurements due to the relatively simple experimental procedure. In the 1970s the idea was proposed by K.B. Broberg, who argued that ductile fracture takes place in two different regions inside the material: the inner fracture process zone (FPZ) and the outer plastic region[48]. The EWF method relies on measuring the total work of fracture inside the FPZ, which represents the formation of new surfaces at the front of the crack tip. The remaining contribution in the plastic zone is dissipated energy. A double-edge notched tension (DENT) specimen is used for measurements. Currently, no standard exists for the evaluation of EWF for metallic materials. There is an ESIS (European Structural Integrity Society) standard however, intended for thin plastic films which is often used as a guide[49]. Because the ligament must fully yield before any crack propagation occurs, as well as maintain a plain-stress state, there are constraints to the double edge-notched tensile (DENT) geometry. In Figure 3.4 the procedure is illustrated schematically, along with the relevant equations that describe the components of the total work of fracture W_f: [7].

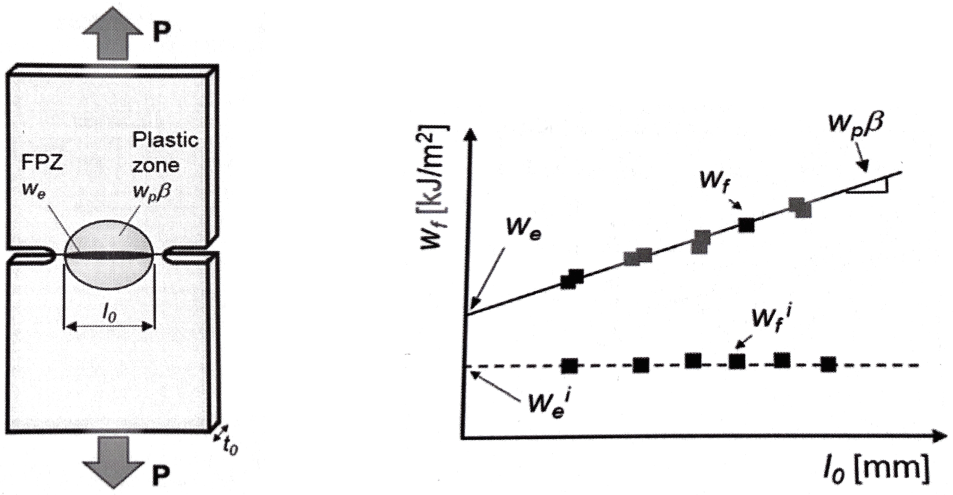

Figure 3.4: *DENT specimen during EWF testing (left) and the obtained work-of-fracture results (right). [7]*

$$W_f = W_e + W_p = w_e L_0 t_0 + \beta w_p L_0^2 t_0 \tag{3.22}$$

Where W_f is the total work of fracture, W_e the essential work of fracture, W_p the non-essential plastic work, w_e the specific essential work of fracture per unit area, w_p the specific non-essential plastic work per unit volume, and β a shape-factor dependent on the plastic zone shape. By dividing the equation by the initial ligament area $L_0 t_0$ the equation reduces to:

$$w_f = w_e + \beta w_p L_0 \tag{3.23}$$

This allows to obtain w_e (and the initiation value w_e^i) from W_f-measurements by linear regression to $L_0 = 0$ (see figure above). The main advantage of this method is that it can be regarded a material property, independent of specimen geometry. Furthermore, it is particularly suitable for thin plates

under plane stress conditions. The values obtained from EWF measurements and J-integral measurements are similar, although EWF measurements incorporate the total energy until complete fracture while J-integral measurements only hold for small crack-advances.

Regarding the DENT specimen constraints, the ESIS protocol explains that the minimum ligament length L_0 must be at least three times the thickness t or 5 mm based on empirical results in polymer-testing. The maximum ligament length should be below two times the radius of the plastic zone to ensure the plasticity constraint, and smaller than one-third the specimen width to eliminate edge-effects [49]. To summarize:

$$\max(3t, 5) < L_0 < \min(2r_p, W/3) \tag{3.24}$$

The notch radius is a highly sensitive parameter for the w_f value, as well as the orientation of the two notches (deviations from the horizontal are especially critical). It is commonly found that smaller notch radii lead to lower fracture toughness values, due to the increase of stress-triaxiality near the crack-tip and limited plasticity. However, it has also been found that below a critical notch radius the fracture toughness remains constant. This parameter is material-dependent and often in the order of 10^{-1} mm [7][49].

Sample preparation with EDM notches

Several DENT samples were machined with an electrical discharge machined (EDM) notch. This is done with only the width of the wire to create a semi-circular notch. This relatively blunt notch ($r_{notch} = 150\mu m$) is chosen to be able to compare with a sharper (microscopic crack-like) initiation. Hence, the influence of the notch radius can be estimated. Samples were taken from neighboring material inside one single coil. A schematic image of the specimens is provided in Figure 3.5 along with an example. The tested specimens are listed in Table 3.3.

Table 3.3: *List of evaluated DENT (EDM notch) fracture toughness samples (orientation is given in ASTM notation).*

Material	Dimensions ($L \times W \times t$)	Ligament length	Temperature	Orientation	Repetitions
XPF1000-UC	$150 \times 80 \times 2.7$ mm^3	25 mm	20 °C	T-L	1
XPF1000-UC	$150 \times 80 \times 2.7$ mm^3	25 mm	20 °C	T-L	1
XPF1000-UC	$150 \times 80 \times 2.7$ mm^3	10 mm	20 °C	L-T	1
XPF1000-UC	$150 \times 80 \times 2.7$ mm^3	10 mm	20 °C	L-T	1

Sample preparation with sheared notches

The established method to introduce a crack-like initiation is via cyclic fatigue loading. However, in this research a novel method of sheared notches is evaluated and compared with fatigue pre-cracking. Previous research has shown the difficulty of introducing a well-defined pre-crack by fatigue loading, as it is extremely sensitive to machine settings and orientation inside the clamps, often resulting in unevenly grown cracks or out-of-plane moments skewing the crack front. Examples will be shown later on in the Results chapter.

The new method (that has been proven to yield reliable results in [50]) is a more practical method for an industry environment as it relies on one single shearing step inside a designated tool. The sample preparation process is shown in Figure 3.6. It consists of three steps:

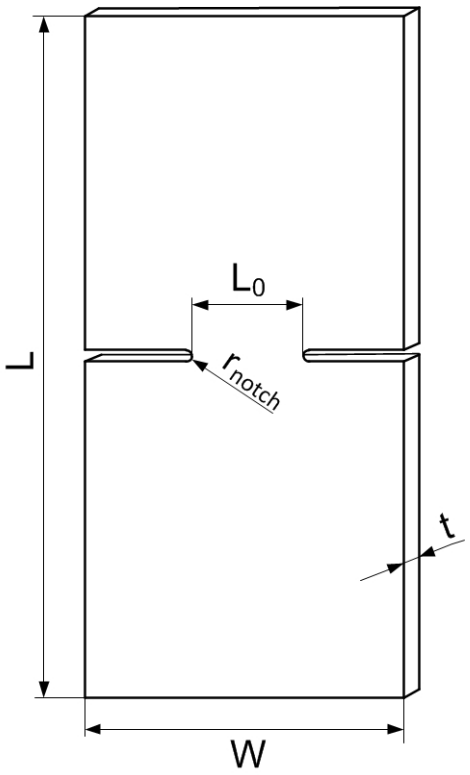

Figure 3.5: *DENT fracture toughness specimen with only EDM notches ($r_{notch} = 150\mu m$).*

1. Cutting material from the coil within a distance d from the edges, to eliminate edge-effects due to rolling
2. Cutting rectangular samples of $L \times W \times t$ [mm^3] to the desired geometry
3. Introducing the sheared notches with the tool, creating a ligament length L_0

The list of evaluated samples is presented in Table 3.4. All specimens were oriented as shown in the figure (ASTM notation: T-L). All samples were cut to size with a hydraulic Darley shearing machine. The notch-shearing tool is shown in Figure 3.7. The tool is fabricated by Weber Machinebouw and the blade is machined from high-strength and high-hardness steel. The blade was inspected regularly for wearing and damage, and replaced when inspection revealed damage. More detailed images of the sheared notch are stored in Appendix A.1.

The different ligament lengths that are required for the essential work of fracture methodology were realized by varying the width W of the sample, as the blade depth inside the tool was constant and always sheared-off the same amount of material. This also lead to the creation of slightly different ligament lengths when the thickness was varied, as this is dependent on both the blade- and sample geometry. The tool only cuts one notch per side, therefore the specimen was flipped to create the second notch. The sample geometries were based on the ESIS protocol but adapted slightly to comply with the geometry of the shearing tool. Consequently, the resulting L_0/W-ratios were higher than the protocol advises (or: lower a/W-ratios). Afterwards the samples received a speckle pattern for DIC measurement on one side, and a black (non-reflective) high-emissivity paint for infrared measurement on the other side.

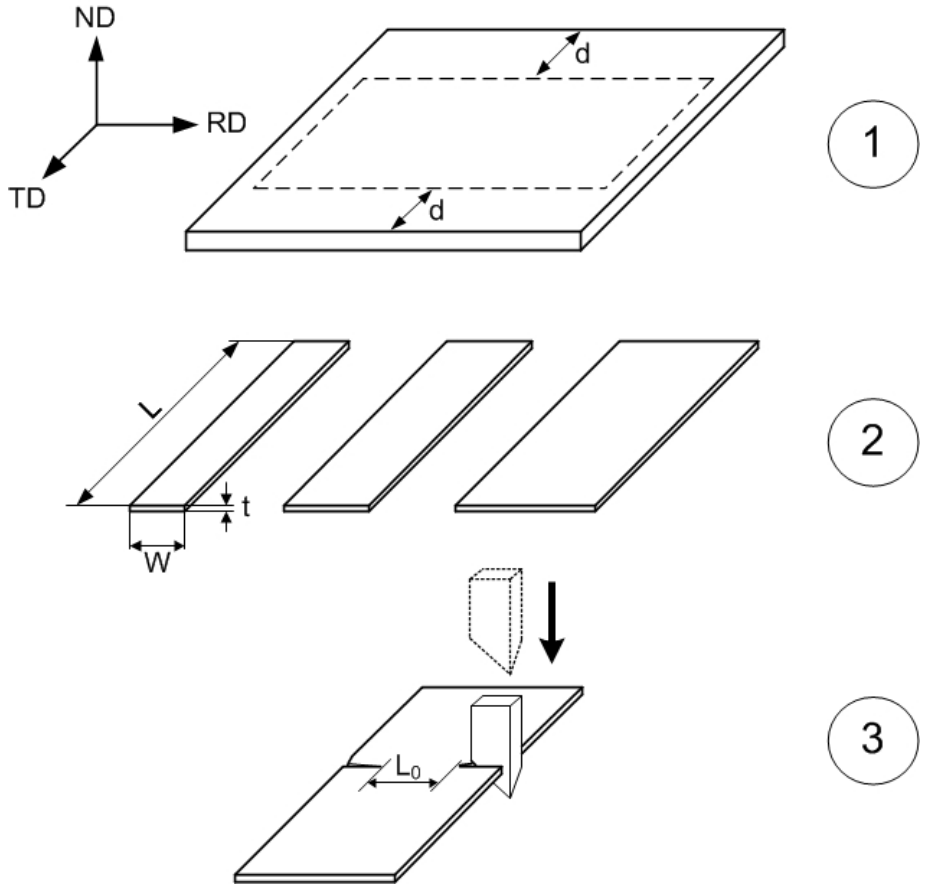

Figure 3.6: *DENT specimen preparation with sheared notches, consisting of three steps (1) material extraction from coil, (2) cutting of specimens and (3) introducing sheared notches.*

Sample preparation with fatigue pre-cracks

To be able to compare to the established method, DENT specimens with fatigue pre-cracks have also been tested. These experiments were done in parallel research as part of Cutting Edge 4.0, a research project funded by European Commission to investigate edge-cracking in AHSS [27]. The initial EDM notch was created with a 150 μm radius. The continued fatigue pre-crack was achieved with a Rumul resonance fatigue machine, to introduce a fatigue crack of $\pm$ 2 mm in length. The sample geometries were based on the recommendations provided in the ESIS protocol [49] to ensure valid ligament lengths (as explained before). A schematic of the created samples is shown in Figure 3.9. The list of evaluated samples is given in Table 3.5.

Experimental setup

The EDM-notched and sheared samples were tested in the Dartec 100 kN testing machine and an MTS 300 kN testing machine equipped with a GOM 3D digital image correlation (DIC) system (35 mm lenses). The samples were pulled at a cylinder displacement rate of 1 mm/min to remain in the quasi-static domain. Global strain data was extracted from DIC measurements with a chosen gauge length of approximately 25 mm. In both machines the samples were gripped in hydraulic clamps and checked for slipping afterwards. The specimen alignment inside the clamps was done manually. The tests were done at elevated temperatures as well, similar to the tensile tests. This was done to estimate the effects of a ductile-to-brittle transition in the XPF1000 material, as will be made clear

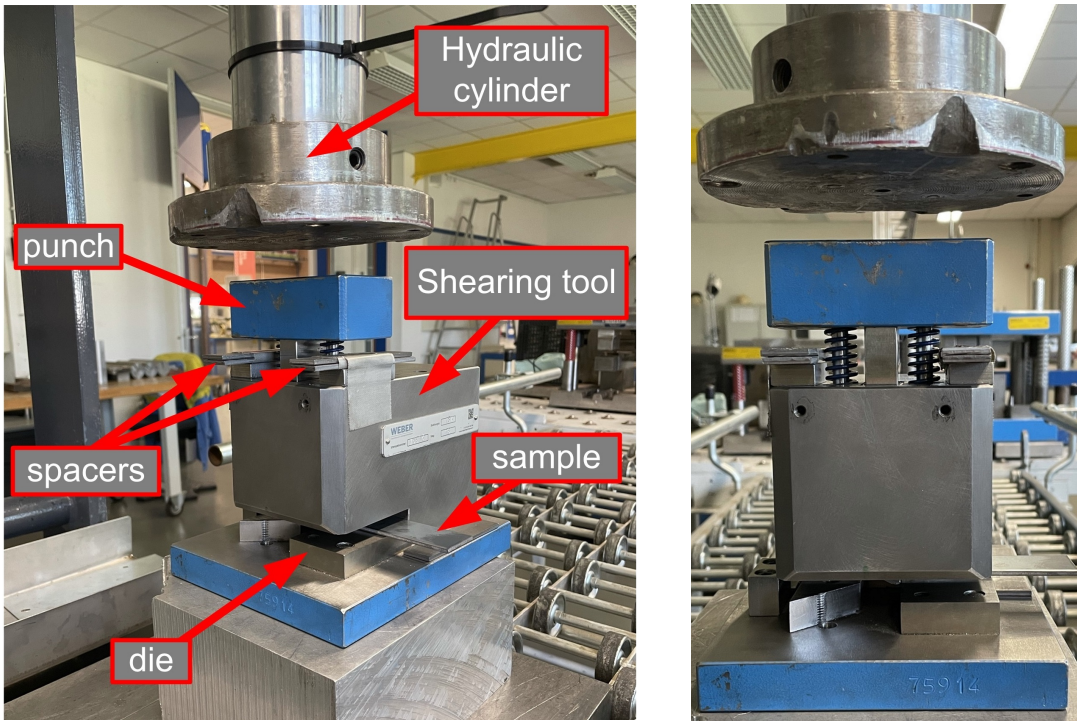

Figure 3.7: *Shearing tool used for notching. The blade is located inside the punch and cuts at a 45° angle. The punch is actuated with a hydraulic cylinder and the stroke is limited with the spacers.*

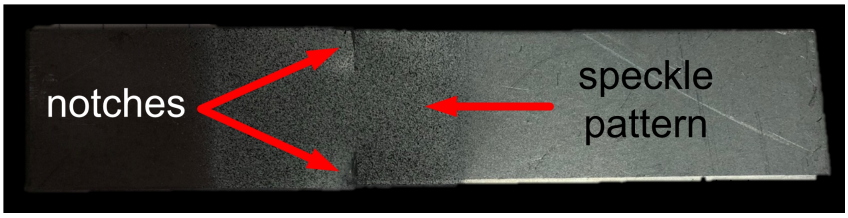

Figure 3.8: *DENT specimen with sheared notches (example).*

from the Results. The temperature measurements from the infrared camera were validated with the readings from a thermocouple (see Table 4.1). The used experimental setup is shown in Figure 3.2 and 3.3. An example of the samples is shown in Figure 3.8.

For the experiments conducted in the Cutting Edge project, a 250 kN universal testing machine was used to pull the specimens at a constant cylinder displacement rate. Full-field strain analysis with a 2D DIC system was used to evaluate the validity of the chosen ligament lengths. whereas a digital video-extensometer was employed to measure the global strains for EWF analysis.

As an additional measurement, a high-speed camera setup was created to check the crack-growth in the case of (sudden) brittle failure during the EWF testing. These images could be used to detect uneven crack growth (from both sides of the sample), due to machine misalignment for example. The high-speed camera was aligned with two mirrors to capture both the front and back of the samples at a sampling frequency of 20,000 frames per second. Designated LED lighting was used to supply a sufficient amount of light. The setup is shown in Figure 3.10.

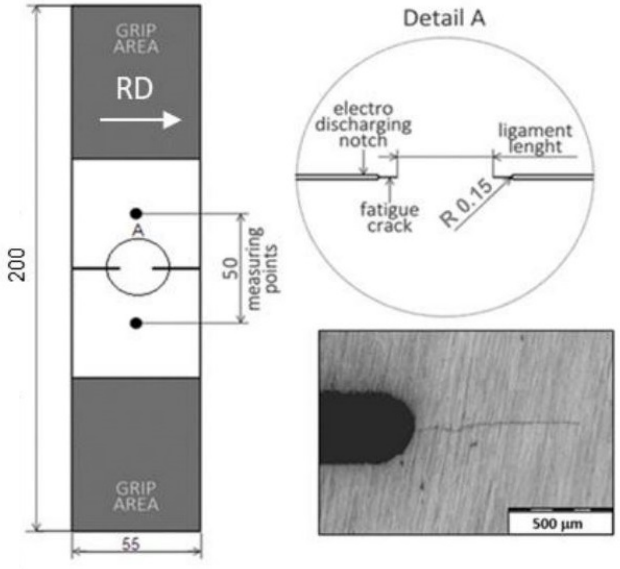

Figure 3.9: *DENT samples with an EDM notch and fatigue pre-crack.[27]*

Data processing

The strain fields from the DIC measurements were analysed with GOM Aramis (version 6.3) and the EWF calculations for fracture toughness were done in MATLAB (version R2016b). Load-displacement data was post-processed in MATLAB as well to filter out noise caused by the hydraulic systems [47][51]. A moving average filter was applied in the form of:

$$y(n) = \frac{1}{W}\{x(n) + x(n-1) + ... + x(n-(W-1))\} \tag{3.25}$$

Where $y(n)$ is the filtered data from vector $x(n)$, and W the chosen window-size, dependent on the noise and length of $x(n)$. The specific work of fracture w_f was then determined by numerically integrating the force-displacement curves until fracture (x_f) and dividing by the initial ligament area A_0:

$$w_f = \frac{W_f}{A_0} = \frac{1}{L_0 \cdot t} \cdot \int_0^{x_f} F dx \tag{3.26}$$

Where L_0 is the ligament length and t the specimen thickness. The ligament lengths were determined afterwards from the fractured surfaces. The specific work of fracture was plotted against the ligament lengths L_0 and a linear regression line was constructed to find the intercept at $L_0 = 0$ for the essential work of fracture w_e.

To ensure that the specimen has failed under plane stress conditions a stress criterion is often introduced with regard to the maximum stresses in the ligament. For example, Hill's criterion prescribes that the net sectional stress in the ligament (for an ideal elastic-plastic material) should be independent of the ligament length L_0 and in the range of [49][52]:

$$\sigma_n \approx 1.15\sigma_y \tag{3.27}$$

The net sectional stress in the ligament at peak load is calculated by dividing the peak force by the initial ligament area:

$$\sigma_n = \frac{F_{max}}{A_0}$$

This stress-level check is adopted in the ESIS protocol as well, and proposes that all stress levels should pass between the boundaries $0.9\sigma_n$ and $1.1\sigma_n$ [49]. However, many studies on AHSS report that this is an underestimation of the actual stresses due to strain-hardening. Instead, the (ultimate) tensile strength is better used to check the stress levels [11][53]. It must be said that this stress criterion is somewhat empirical and dependent of material properties such as the strain hardening coefficient, and should therefore be assessed per material.

3.3 Fracture surface examination

The fractured surfaces of the broken specimens were investigated to derive the fracture mechanisms that took place. This provides valuable insight in the type of deformation that has occurred and the amount of ductility associated with it. Hence it is used to conclude whether the type of failure was predominantly brittle or ductile (or a mixed-mode). A Zeiss scanning electron microscope (SEM) was employed to detect back-scattered electrons and secondary electrons.

In addition to the fracture mechanisms, the effect and quality of the sheared notches were evaluated as well as the fatigue pre-crack from the CuttingEdge project samples. The findings are stored in the Appendix A.1.

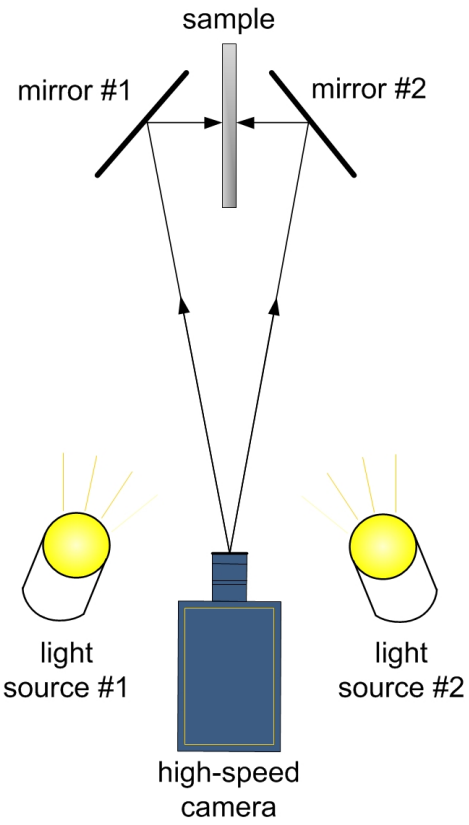

Figure 3.10: *High-speed camera setup*

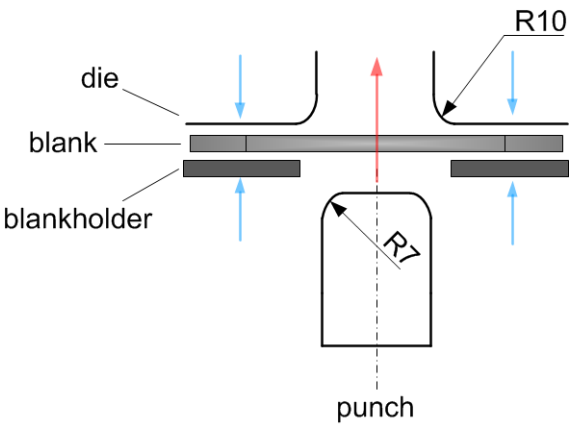

Figure 3.11: *Deep-drawing setup.*

3.5 Lab-scale deep-drawing

Sample preparation

To check the results of the EWF testing, small semi-cylindrical cups were deep-drawn from 90x90 mm^2 blanks, with 10 mm cut off diagonally from the corners. The material was cut to size with a shearing machine. This test was chosen because it is particularly useful to reveal the susceptibility to edge-cracking, and can thus be used as a rough validation of the results from the fracture toughness tests. In addition, the blank undergoes different types of deformation i.e. stress triaxialities. The observed cracking can then be traced back to the type of loading that caused it. One sample was prepared with a dotted grid on both sides before deep-drawing to show the deformations after the process. An image of the samples is shown in Figure 3.12 before and after deep-drawing.

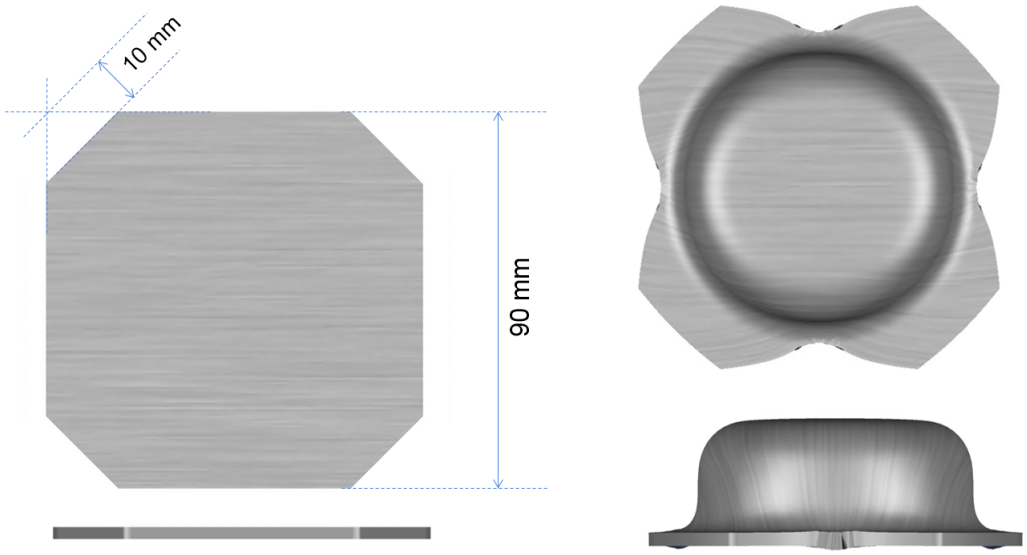

Figure 3.12: *Deep-drawing specimens (before and after).*

Experimental setup

The deep-drawing experiments were all conducted on an Erichssen press. In Figure 3.11 the setup is shown schematically. A 50 mm-wide rounded cylindrical punch was used with a 7 mm corner radius, together with a 62 mm-wide die with a 10 mm radius. To restrain the material, a (uniform) blankholder force of 250 kN was applied. The same die and settings were used regardless of the different sheet thicknesses (see Table 3.6). The deep-drawn cups were afterwards inspected for cracks with light optical microscopy (LOM). For the additional experiment of opening the cups even further, a conical punch was used instead during which the cylinder displacement and punch force were logged.

Table 3.4: *List of evaluated DENT (sheared notches) fracture toughness samples (orientation is given in ASTM notation).*

Material	Dimensions ($L \times W \times t$)	Ligament length	Temperature	Orientation	Repetitions
XPF1000-UC	$150 \times 35 \times 1.8$ mm^3	30 mm	20 °C	T-L	3
XPF1000-UC	$150 \times 30 \times 1.8$ mm^3	25 mm	20 °C	T-L	3
XPF1000-UC	$150 \times 25 \times 1.8$ mm^3	20 mm	20 °C	T-L	3
XPF1000-UC	$150 \times 20 \times 1.8$ mm^3	15 mm	20 °C	T-L	3
XPF1000-UC	$150 \times 30 \times 2.7$ mm^3	22 mm	20 °C	T-L	3
XPF1000-UC	$150 \times 25 \times 2.7$ mm^3	17 mm	20 °C	T-L	7
XPF1000-UC	$150 \times 20 \times 2.7$ mm^3	12 mm	20 °C	T-L	3
XPF1000-UC	$150 \times 20 \times 2.7$ mm^3	8 mm	20 °C	T-L	3
XPF1000-GI	$150 \times 30 \times 2.7$ mm^3	22 mm	20 °C	T-L	3
XPF1000-GI	$150 \times 25 \times 2.7$ mm^3	17 mm	20 °C	T-L	7
XPF1000-GI	$150 \times 20 \times 2.7$ mm^3	12 mm	20 °C	T-L	3
XPF1000-GI	$150 \times 20 \times 2.7$ mm^3	8 mm	20 °C	T-L	3
XPF1000-UC	$150 \times 25 \times 2.7$ mm^3	17 mm	60 °C	T-L	6
XPF1000-UC	$150 \times 20 \times 2.7$ mm^3	12 mm	60 °C	T-L	3
XPF1000-GI	$150 \times 25 \times 2.7$ mm^3	17 mm	60 °C	T-L	6
XPF1000-GI	$150 \times 20 \times 2.7$ mm^3	12 mm	60 °C	T-L	3
XPF1000-UC	$150 \times 25 \times 2.7$ mm^3	17 mm	100 °C	T-L	2
XPF1000-GI	$150 \times 25 \times 2.7$ mm^3	17 mm	100 °C	T-L	3
XPF1000-UC	$150 \times 25 \times 2.7$ mm^3	17 mm	120 °C	T-L	2
XPF1000-UC	$150 \times 20 \times 2.7$ mm^3	12 mm	120 °C	T-L	2
XPF1000-GI	$150 \times 25 \times 2.7$ mm^3	17 mm	120 °C	T-L	2
XPF1000-GI	$150 \times 20 \times 2.7$ mm^3	12 mm	120 °C	T-L	2
XPF1000-UC	$150 \times 30 \times 2.9$ mm^3	22 mm	20 °C	T-L	3
XPF1000-UC	$150 \times 25 \times 2.9$ mm^3	17 mm	20 °C	T-L	2
XPF1000-UC	$150 \times 20 \times 2.9$ mm^3	12 mm	20 °C	T-L	3
XPF800-UC	$150 \times 30 \times 3.2$ mm^3	22 mm	20 °C	T-L	2
XPF800-UC	$150 \times 25 \times 3.2$ mm^3	17 mm	20 °C	T-L	2
XPF800-UC	$150 \times 20 \times 3.2$ mm^3	12 mm	20 °C	T-L	3
DP1000-GI	$150 \times 30 \times 2.0$ mm^3	23 mm	20 °C	T-L	3
DP1000-GI	$150 \times 25 \times 2.0$ mm^3	18 mm	20 °C	T-L	3
DP1000-GI	$150 \times 20 \times 2.0$ mm^3	13 mm	20 °C	T-L	3
DP1000-GI	$150 \times 20 \times 2.0$ mm^3	8 mm	20 °C	T-L	3
CP800-UC	$150 \times 30 \times 3.3$ mm^3	22 mm	20 °C	T-L	2
CP800-UC	$150 \times 25 \times 3.3$ mm^3	17 mm	20 °C	T-L	2
CP800-UC	$150 \times 20 \times 3.3$ mm^3	12 mm	20 °C	T-L	3
CP800-UC	$150 \times 30 \times 4.0$ mm^3	22 mm	20 °C	T-L	3
CP800-UC	$150 \times 25 \times 4.0$ mm^3	17 mm	20 °C	T-L	3
CP800-UC	$150 \times 20 \times 4.0$ mm^3	12 mm	20 °C	T-L	3
S550MC-UC	$150 \times 30 \times 3.0$ mm^3	22 mm	20 °C	T-L	3
S550MC-UC	$150 \times 25 \times 3.0$ mm^3	17 mm	20 °C	T-L	3
S550MC-UC	$150 \times 20 \times 3.0$ mm^3	12 mm	20 °C	T-L	1

Table 3.5: *List of evaluated DENT (fatigue-cracked) fracture toughness samples (orientation is given in ASTM notation)[27].*

Material	Dimensions ($L \times W \times t$)	Ligament length	Temperature	Orientation	Repetitions
XPF1000-UC	$200 \times 55 \times 2.9$ mm^3	6 mm	20 °C	T-L	3
XPF1000-UC	$200 \times 55 \times 2.9$ mm^3	8 mm	20 °C	T-L	3
XPF1000-UC	$200 \times 55 \times 2.9$ mm^3	10 mm	20 °C	T-L	3
XPF1000-UC	$200 \times 55 \times 2.9$ mm^3	12 mm	20 °C	T-L	3
XPF1000-UC	$200 \times 55 \times 2.9$ mm^3	14 mm	20 °C	T-L	3
CP800-UC	$200 \times 55 \times 3.3$ mm^3	6 mm	20 °C	T-L	3
CP800-UC	$200 \times 55 \times 3.3$ mm^3	8 mm	20 °C	T-L	3
CP800-UC	$200 \times 55 \times 3.3$ mm^3	10 mm	20 °C	T-L	3
CP800-UC	$200 \times 55 \times 3.3$ mm^3	12 mm	20 °C	T-L	3
CP800-UC	$200 \times 55 \times 3.3$ mm^3	14 mm	20 °C	T-L	3
XPF800-UC	$200 \times 55 \times 3.2$ mm^3	6 mm	20 °C	T-L	3
XPF800-UC	$200 \times 55 \times 3.2$ mm^3	8 mm	20 °C	T-L	3
XPF800-UC	$200 \times 55 \times 3.2$ mm^3	10 mm	20 °C	T-L	3
XPF800-UC	$200 \times 55 \times 3.2$ mm^3	12 mm	20 °C	T-L	3
XPF800-UC	$200 \times 55 \times 3.2$ mm^3	14 mm	20 °C	T-L	3
S550MC-UC	$200 \times 55 \times 3.0$ mm^3	6 mm	20 °C	T-L	3
S550MC-UC	$200 \times 55 \times 3.0$ mm^3	8 mm	20 °C	T-L	3
S550MC-UC	$200 \times 55 \times 3.0$ mm^3	10 mm	20 °C	T-L	3
S550MC-UC	$200 \times 55 \times 3.0$ mm^3	12 mm	20 °C	T-L	3
S550MC-UC	$200 \times 55 \times 3.0$ mm^3	14 mm	20 °C	T-L	3

Table 3.6: *Deep-drawing test configuration*

Blank geometry:	$90 \times 90 \times t$ mm^3
Die diameter:	62 mm
Die corner radius:	10 mm
Punch diameter:	50 mm
Punch outer radius:	7 mm
Blankholder force:	250 kN

4. Results and discussion

4.1 Tensile testing

The tensile test results of four investigated steels, which were performed externally as part of the Cutting Edge project, are presented in Figure 4.1 for reference. Hereafter the additional tensile testing results of XPF1000 (2.7 mm) are presented.

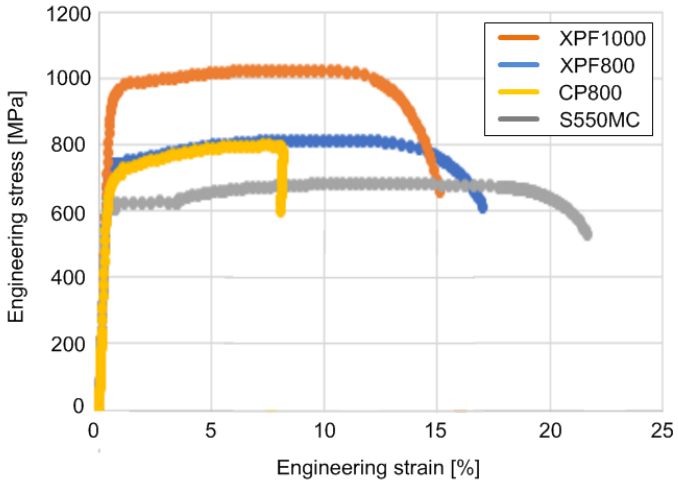

Figure 4.1: *Engineering stress-strain curves obtained during uniaxial tensile testing of the four hot-rolled steel grades, according to DIN EN ISO 6892-1. [27].*

The obtained mechanical properties of XPF1000 (2.7 mm thickness) are collected in Table 4.2. It was observed during testing that the two paint layers on either side (speckle pattern and black infrared paint) delaminated as a result of the specimens breaking (recall Figure A5). After inspection it was found that it did not influence the measurements significantly, as it occurred at the very end of the experiment where the relevant datapoints had already been collected.

Several observations can be made from the tensile tests results. Firstly, the XPF1000 in general has a higher strength in transverse direction (T-L) compared to longitudinal direction (L-T). Similarly, the ductility is higher in longitudinal direction. This is an expected effect due to (hot-)rolling; the plastic deformation introduced by the rolls causes re-orientation of the crystals to stable positions and thereby induces preferred crystallographic orientations within the microstructure (crystallographic texture)[55]. The strain-hardening coefficient is relatively low as well, as can be seen from Figure 4.2 too. A close-up of the yield point phenomenon is stored in Figure A7 in Appendix A.2. A trend can be observed with regard to the temperature effect: increasing the temperature to 60 ^{o}C or even 100 ^{o}C lowers both the yield strength and tensile strength. A tensile strength loss between 39 and 50 MPa is measured when increasing the temperature from 20 to 100 ^{o}C. The corresponding drop in 0.2% yield strength is between 22 and 71 MPa. The spread in ductility (total elongation & uniform elongation) was too large to draw any conclusions whether it increases or decreases as a result of the elevated temperature. The trends with respect to temperature are plotted in Figure 4.3. The effects of dynamic strain aging in this temperature range are likely responsible for the observed

trends in the strength and ductility, according to similar research [54]. The other properties such as the strain-hardening coefficient and plastic strain ratio were not measurably influenced by the temperature.

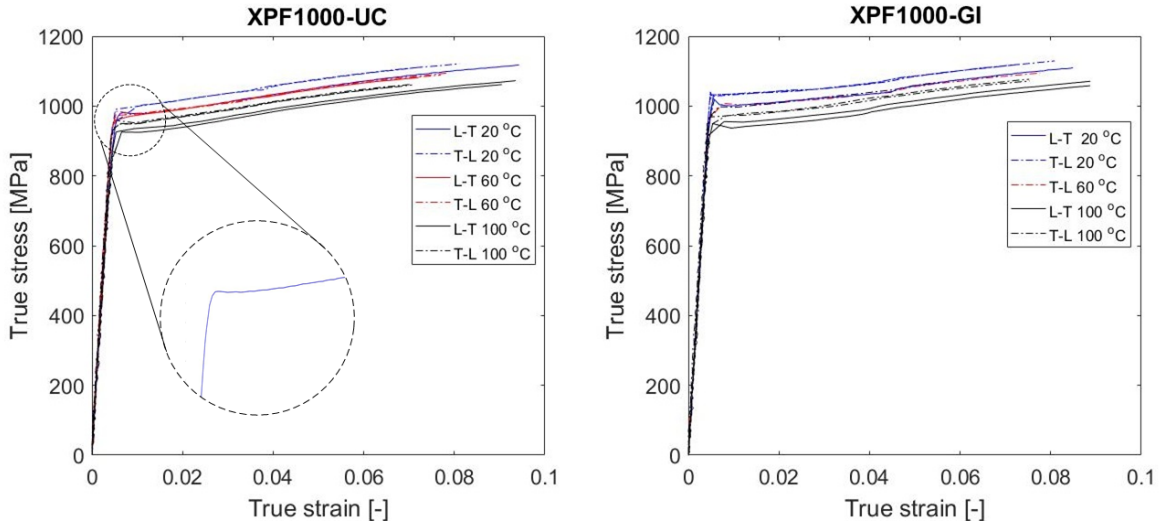

Figure 4.2: *True stress vs. true strain curves for XPF1000-UC (#1) and XPF1000-GI (#2) at 20, 60 and 100 °C.*

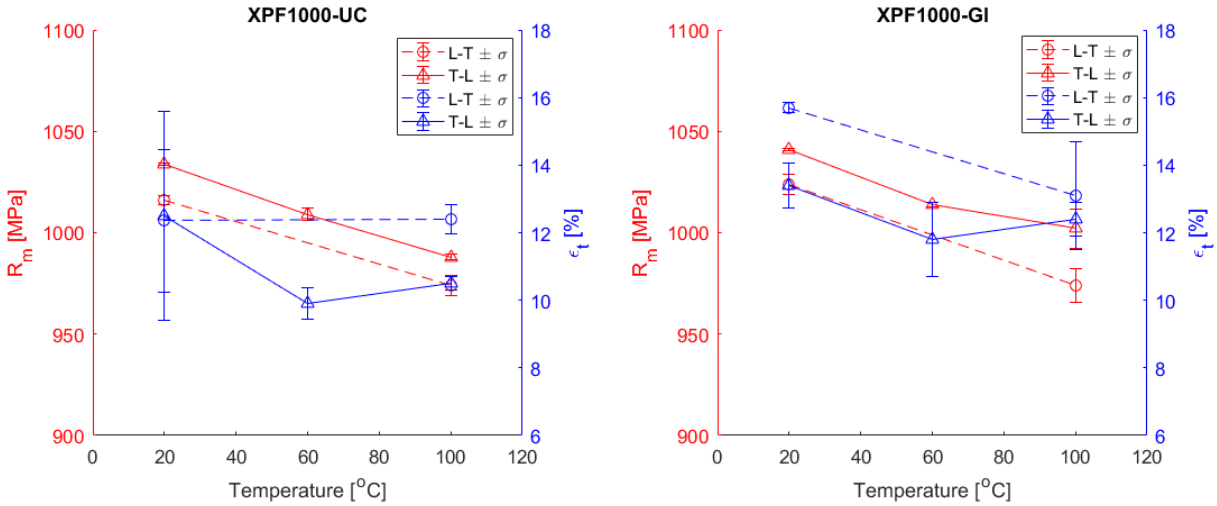

Figure 4.3: *The effect of temperature on the tensile strength and total elongation for XPF1000-UC/GI (2.7 mm thickness).*

As can be seen from the tensile curves, there are insufficient data points around the yield point to obtain a smooth curve (for most of the curves). This can lead to inaccuracies in the determination of the yield stress and the obtained values should therefore be viewed with some caution. The program settings during the tensile test were inadequate for this steel grade as it continued to the higher displacement rate too soon. The relatively low measuring frequency of the DIC system could not measure enough datapoints as a result.

Regarding the temperature control, it was difficult to keep stable at 100 °C due the experimental setup. The spread in temperature was estimated at ± 5 °C at 100 °C and ± 2 °C at 60 °C. The readings are taken from the infrared camera. It was discovered that the (more trustworthy) thermocouple measured a difference in the temperature however (Table 4.1 below). Throughout all the experiments the temperature was measured with the infrared camera however for consistency.

Table 4.1: *Temperature measurement validation of the infrared camera with thermocouple readings.*

IR-camera	Thermocouple	Difference
30 °C	33 °C	+ 3 °C
65 °C	69 °C	+ 4 °C
100 °C	110 °C	+ 10 °C

The extra measurement taken from different coils of XPF1000-GI at room temperature were done to assess the variance of properties in the coils of the same material. A 0.2% yield strength differential of 47 MPa and 49 MPa is observed in T-L and L-T direction, respectively. The difference in tensile strength is 42 MPa (T-L) and 43 MPa (L-T). Similarly, the variance in total elongation is 2.7 %-points (T-L) and 0.7 %-points (L-T). The remaining properties such as the strain-hardening coefficient experienced a similar spread as well.

To estimate the *global formability* of steels, a toughness parameter is often introduced that is proportional to the total elongation and tensile strength i.e. $R_m \times \varepsilon_t$. The five investigated steels (XPF800/1000, DP1000, CP800 and S550MC) are compared in Figure 4.4. Based on this information the S550MC grade shows the highest toughness while the CP800 shows the lowest toughness. This parameter does not account for variations in the strain hardening behaviour, but serves as an approximation only. The *local formability* i.e. (edge) cracking-resistance is assessed with the fracture toughness measurements, which is discussed and compared with in the next section.

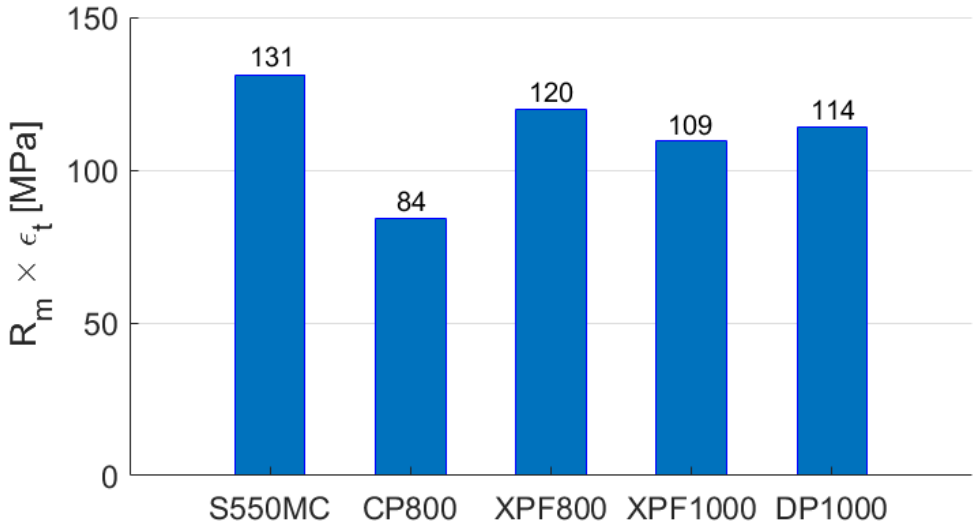

Figure 4.4: *Toughness values ($R_m \times \varepsilon_t$) of the five investigated steels to estimate the global formability.* ***NB The average values are taken here.***

Table 4.2: *Average mechanical properties obtained during A50R tensile testing including the standard deviation. All specimens were of 2.7 mm thickness.* ***NB no scatter is shown for values that have only one datapoint.***

Material (from coil)	Orientation	$R_{p0.2}$ [MPa]	R_m [MPa]	ε_u [%]	ε_t [%]	Strain-hardening coefficient n [-]	Lankford coefficient r [-]
[20 °C]							
XPF1000-UC (#1)	T-L	979±16	1034±0.58	8.2±1.3	12.5±3.0	0.077±0.0020	0.74±0.012
XPF1000-UC (#1)	L-T	943±44	1016±2.1	9.3±0.14	12.4±2.1	0.084	0.65
XPF1000-GI (#2)	T-L	1024±2.1	1041±0.58	7.3±0.49	13.4±0.66	0.074±0.0090	0.73±0.015
XPF1000-GI (#2)	L-T	1007±9.9	1024±4.9	8.1±0.50	15.7±0.14	0.102±0.004	0.66±0.002
XPF1000-GI (#3)	T-L	992±3.5	1015±7.1	6.8±0.42	10.8±0.64	0.089±0.017	0.80±0.033
XPF1000-GI (#3)	L-T	962±0.71	988±1.4	7.9±0.49	12.5±3.3	0.091	0.64±0.044
XPF1000-GI (#4)	T-L	977±0.71	1002	7.4±0.49	11.4±2.4	0.080±0.0030	0.79±0.0010
XPF1000-GI (#4)	L-T	958±7.8	981±1.4	8.2±0.57	14.2±0.21	0.083±0.0090	0.71
XPF1000-GI (#5)	T-L	1008±4.2	1030±4.9	6.3	12.2±0.21	0.073±0.0040	0.76±0.002
XPF1000-GI (#5)	L-T	980±14	1001	8.6±0.35	14.8±1.3	0.081	0.66±0.002
XPF1000-GI (#6)	T-L	1021±4.2	1044±2.1	7.4±0.014	13.5±0.85	0.083±0.0020	0.77±0.0010
XPF1000-GI (#6)	L-T	1000±0.70	1008±2.8	8.4±1.4	14.9	0.089±0.0040	0.70±0.0040
[60 °C]							
XPF1000-UC (#1)	T-L	968±9.5	1009±3.1	7.4±0.36	9.9±0.46	0.079±0.0010	0.75±0.0070
XPF1000-GI (#2)	T-L	984±7.5	1014±1.2	6.9±0.58	11.7±1.1	0.088±0.0020	0.73±0.0090
[100 °C]							
XPF1000-UC (#1)	T-L	946±4.7	988±1.5	6.7±0.21	10.5±0.21	0.078±0.0010	0.74±0.0090
XPF1000-UC (#1)	L-T	921±2.8	974±4.9	9.2±0.21	12.4±0.42	0.083±0.0020	0.68±0.0070
XPF1000-GI (#2)	T-L	972±25	1002±9.8	7.2±0.21	12.4±0.50	0.077±0.0030	0.74±0.0090
XPF1000-GI (#2)	L-T	936±3.5	974±8.5	8.8	13.1±1.6	0.081±0.0010	0.67±0.0090

4.2 Fracture toughness testing

Blunt EDM notch

In Figure 4.5 the load-displacement curves are shown, in which the anisotropy effects are immediately visible. The samples yield at a higher load in transverse direction (T-L) compared to longitudinal direction (L-T). Similarly, the samples in longitudinal direction show higher ductility as well. These findings correspond to the tensile test results presented earlier. Complete fracture occurs suddenly at the 25 mm ligament specimens after significant elongation, while the load is gradually decreased in the 10 mm ligament specimens. This indicates a considerable area reduction, caused by crack growth and/or necking.

From the strain fields it can be seen that plasticity develops in front of the notch-tip. This zone is highly localised initially, but grows larger and more elliptical as the load is increased, until it meets and connects with the opposing side. Yielding occurs within the ligament before the fracture takes place, validating the choice of ligament sizes. Figure 4.6 shows the developing plasticity in the ligament area at several stages. Notch-tip blunting is observed as a result of stress concentrations during load increase, opening the notch further. Crack growth is initiated only after the load drops. The fracture process is illustrated in Figure 4.7. A fracture surface with shear lips is found after closer inspection.

The local directions of both the major- and minor strains at peak load are illustrated in Figure A8 (Appendix A.3). A negative minor strain is found at the plastic zones and a positive strain at the ligament; an effect of the blunting shown in Figure 4.7b causing tension in the ligament. At the same time there is a positive shear strain at the plastic zones. The complete minor strain distribution as well as the shear strain distribution are shown in Figure 4.8.

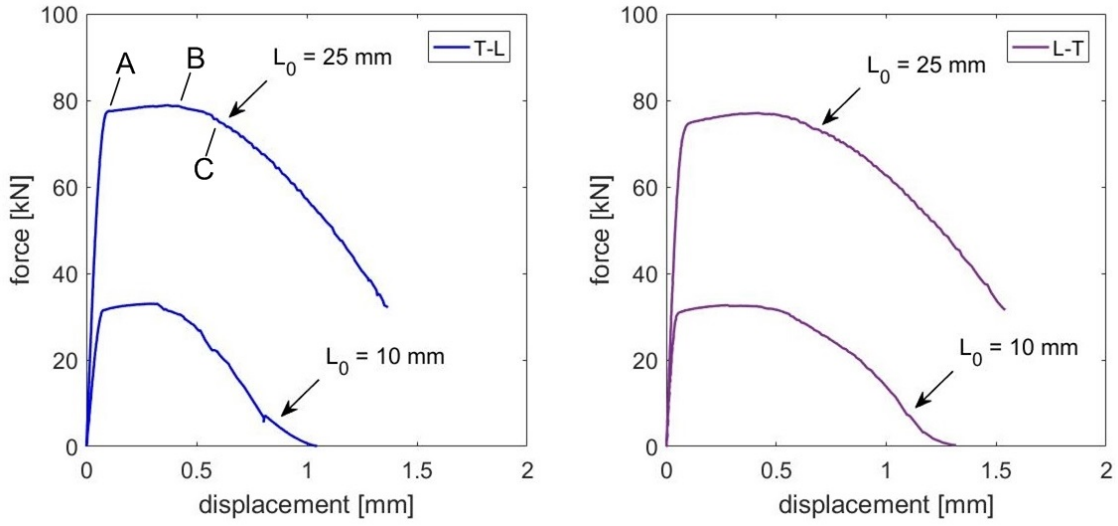

Figure 4.5: *Global load-displacement curves obtained during EWF testing of DENT samples with a blunt EDM-notch.* ***NB The curves represent single measurements.***

The essential work of fracture methodology was applied with just the two ligament lengths (10 and 25 mm). The results are shown in Figure 4.9. The high ductility observed in the force-displacement curves of the longitudinal specimens, especially for the smaller ligament, results in

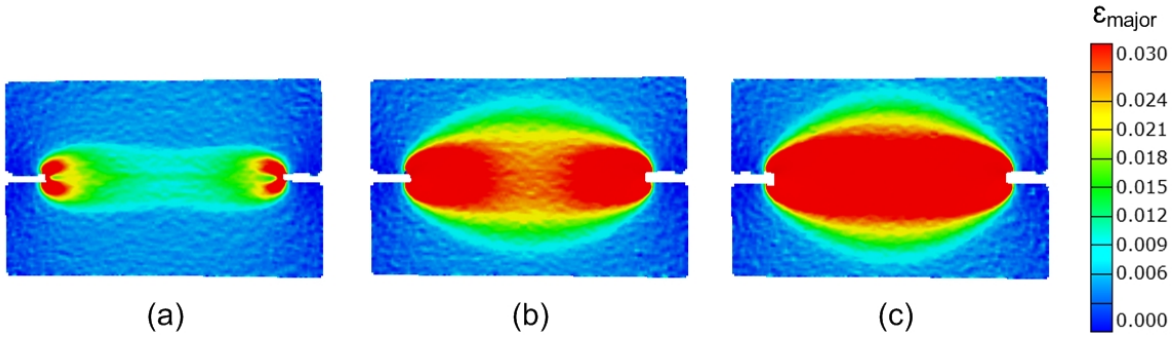

Figure 4.6: *Major strain plots extracted from DIC measurements indicating plasticity development in the ligament during* ***(a)*** *yielding (end of linear-elastic domain)* ***(b)*** *peak force and* ***(c)*** *observed crack growth (as indicated in Figure 4.5).*

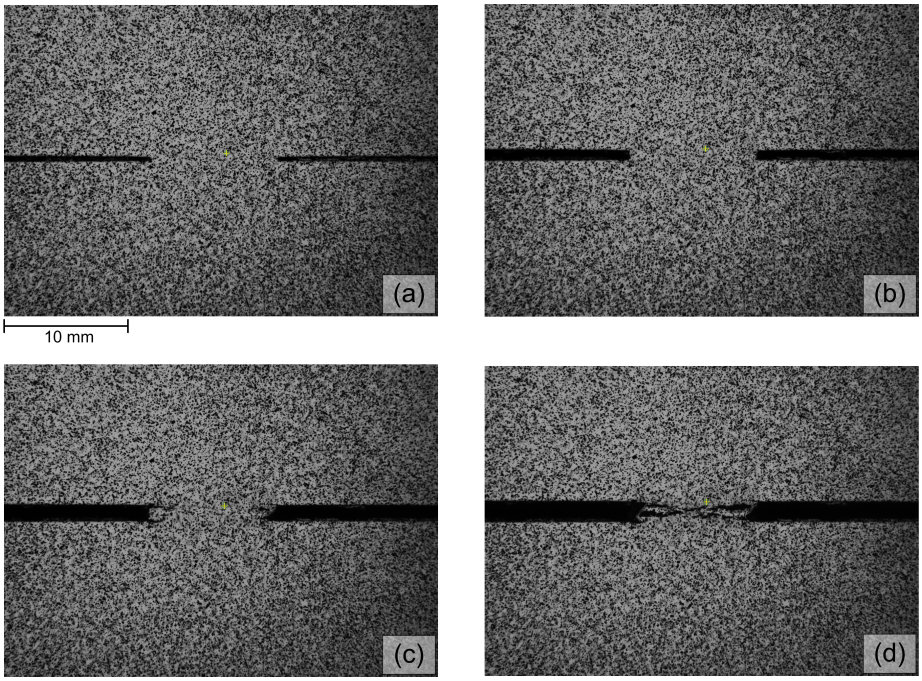

Figure 4.7: *Fracture process during EWF testing:* ***(a)*** *undeformed* ***(b)*** *crack blunting* ***(c)*** *crack growth* ***(d)*** *complete fracture. The load starts to decrease from point* ***(c)*** *onwards.*

a much higher essential work of fracture for this orientation. In addition, the slope of the curve (plastic dissipation factor) is higher for the T-L specimen, meaning that the plastic contribution is relatively larger here. It is of course important to remark that no repeated measurements have been done, therefore no confidence interval can be estimated from the linear fit. The linear fit can be offset significantly by w_f at the smaller ligament. Overall, it can be concluded that the essential work of fracture i.e. the fracture toughness is higher in L-T orientation, therefore the T-L orientation should be leading to assess the critical fracture toughness.

When applying the stress criterion based on the ultimate tensile strength, it shows that the stress levels are indeed independent of L_0 and satisfy the imposed criterion ($\sigma \approx 1150 MPa$). The experiments can thus be concluded valid with respect to the ligament choice.

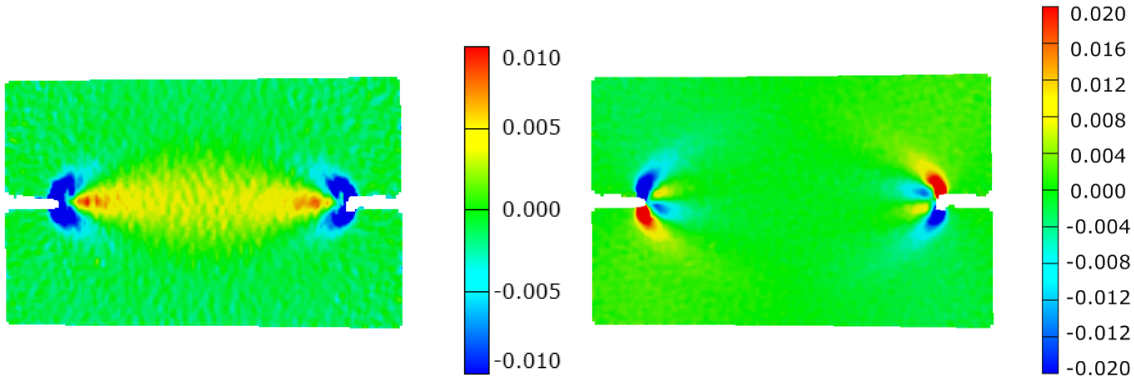

(a) Minor strain (b) Shear strain

Figure 4.8: *Minor strain and shear strain for the T-L specimen with a 25 mm ligament length at peak load, extracted from DIC measurements.* ***NB different scales were used in the two images.***

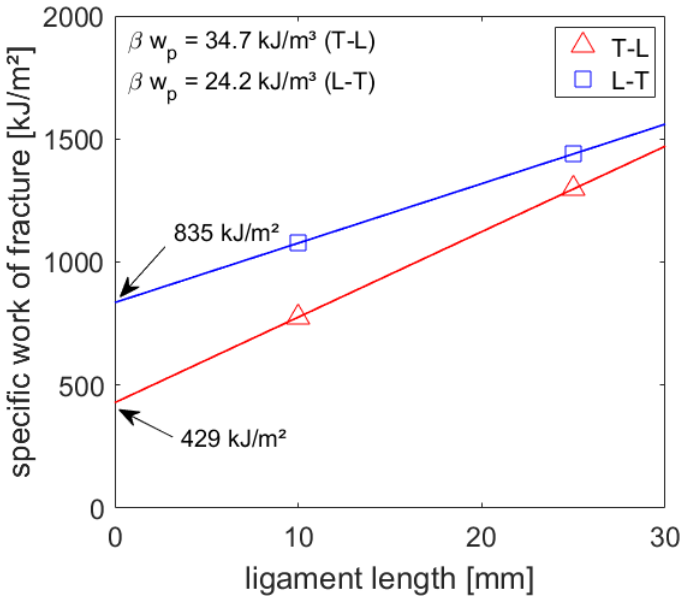

Figure 4.9: *Specific work of fracture w_f of XPF1000-UC as a function of ligament length L_0 including the linear regression line.* ***NB The datapoints represent the single-measurements***

Sheared notch

The EWF results from the sheared-notch samples are presented here for the different investigated materials, presented individually first. More experimental efforts and additional analysis was dedicated to the XPF1000 and DP1000 grades, due to company-related interests and logistical reasons. The remaining materials are treated more briefly and serve mostly as reference measurements. At the end of the chapter an overview of all measurements is given.

DP1000 (2.0 mm)

The force-displacement curves are shown in Figure 4.10a and the EWF results are shown in Figure 4.10b. Here it can be seen that all specimens show a similar mechanical response; the slope decreases as the maximum load is approached whereafter the load decreases again until fracture. This shows that strain hardening takes place before the peak load is attained. From experimental observations it is seen that stable crack propagation occurs when the load starts to decrease. Furthermore, the curves show fair reproducibility and the different ligament lengths can be distinguished easily.

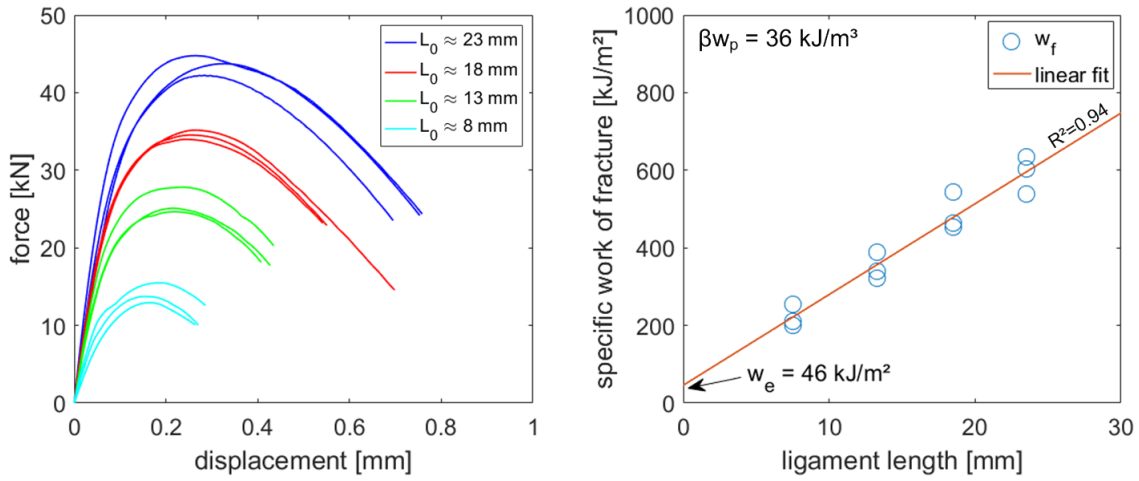

(a) Global force-displacement curves

(b) Specific work of fracture w_f

Figure 4.10: *EWF results of DP1000-GI (2.0 mm thickness) with sheared notches*

Full-field strain analysis from DIC shows that the ligament is fully yielded before crack propagation takes place (Figure 4.11). The plastic zone shape is slightly different than before, as the shearing step induces a certain torsional deformation in one half of the specimen. The created 'crack' front is twisted slightly due to the small clearance between the blade and specimen. This shearing pre-deformation affects the measurements as well; as the load is ramped during testing a small brittle-like crack extension takes place right before the peak load. This was first noticed visually during testing (a through-thickness crack was observed) and later on discovered during fracture surface examination. Additional evidence is provided in the 'XPF1000' paragraph. Stable crack propagation takes place hereafter. The essential work of fracture methodology relies on a fully yielded ligament in plane stress conditions before fracture; it is not suited to describe brittle behaviour of metallic plates. Figure 4.13 shows an example of a fractured surface wherein the two ligament areas can be separated. This deviating crack growth increment was subtracted from the ligament area calculations accordingly. This is done by taking an estimated average ligament length of all repeated samples per width.

Furthermore, the major strain distribution at fracture initiation is more localized for the lower ligament lengths. Complete ligament yielding is sooner reached in the samples with a lower ligament length. The strain levels are higher for the wider sample but the width of the plastic zone remains relatively constant, as can be seen from the plots in Figure 4.12. The crack growth follows the shape of the plastic zone and is illustrated in Figure 4.15. Here it can be seen that the two slanted cracks grow at an opposite angle of each other (due to the sheared notches) and final fracture takes place at a shear angle as a result (see Figure 4.16).

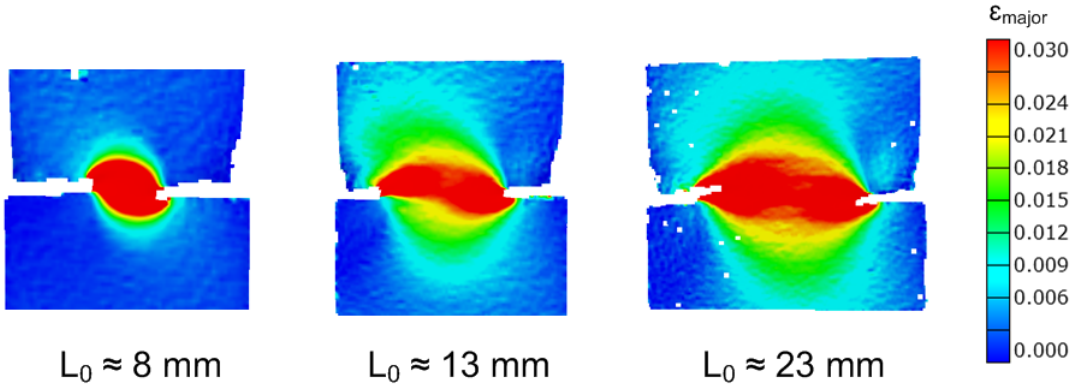

Figure 4.11: *Major strain distributions of DP1000-GI with sheared notches (2.0 mm thickness) before fracture initiation, for three different ligament lengths.*

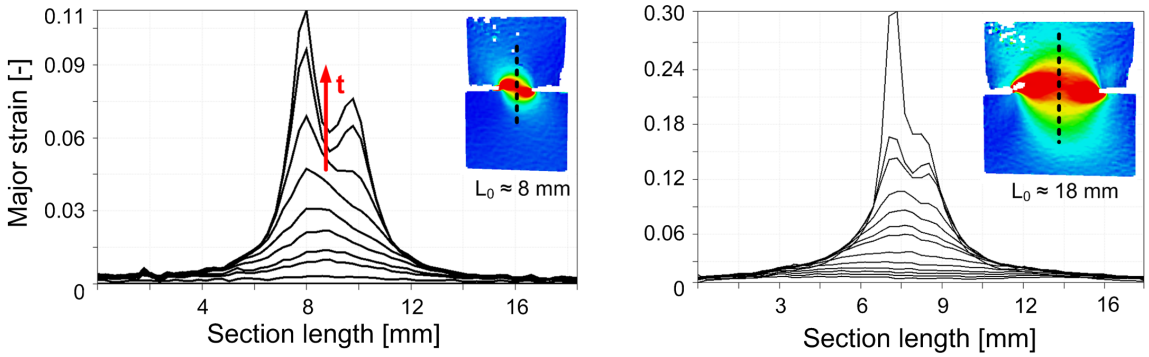

Figure 4.12: *Evolution of the major strain plotted against section length for two DP1000 specimen widths.*

Fracture surfaces investigations shows extensive evidence of ductile fracture through a dimpled morphology with limited necking in the middle region. Shear lips at approximately 45^{o} are found at full thickness of the specimen at either sides (completely slant fracture), possibly due to the nucleation of voids along the angled deformation bands combined with a thin sample in plane stress. The two angled fracture planes meet in the middle and show limited necking ($\pm$30% contraction). The region wherein the brittle-like crack increment is found shows traces of cleavage fracture while most of the remaining fracture surface is dimpled, indicating ductile fracture by microvoid coalescence (Figure 4.14b). The mechanical shearing tool produced a different type of notch as compared to the fatigue pre-cracked samples. Due to the angle of the blade, a 45^{o} mark is left behind.

The maximum stress levels show that they are relatively independent of the ligament length and

gather around $\sigma_{uts} \pm 10\%$ (see Figure A10 in Appendix A.3). The chosen ligaments are valid to use according to the stress criterion. The specific work of fracture values (w_f) are lower than the 'high toughness' work of fracture values for fatigue pre-cracked XPF1000 (previous paragraph) at similar ligament lengths. Furthermore, the essential work of fracture (w_e) is 46 kJ/m^2 and roughly 10 times lower than XPF1000 with a blunt notch. The plastic dissipation factor is roughly equal.

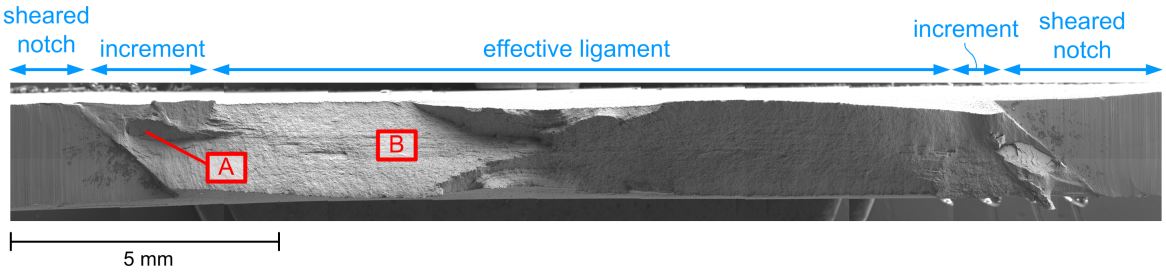

Figure 4.13: *SEM (secondary electrons) overview image of the DP1000-GI fractured surface (2.0 mm thickness) with the different zones indicated.*

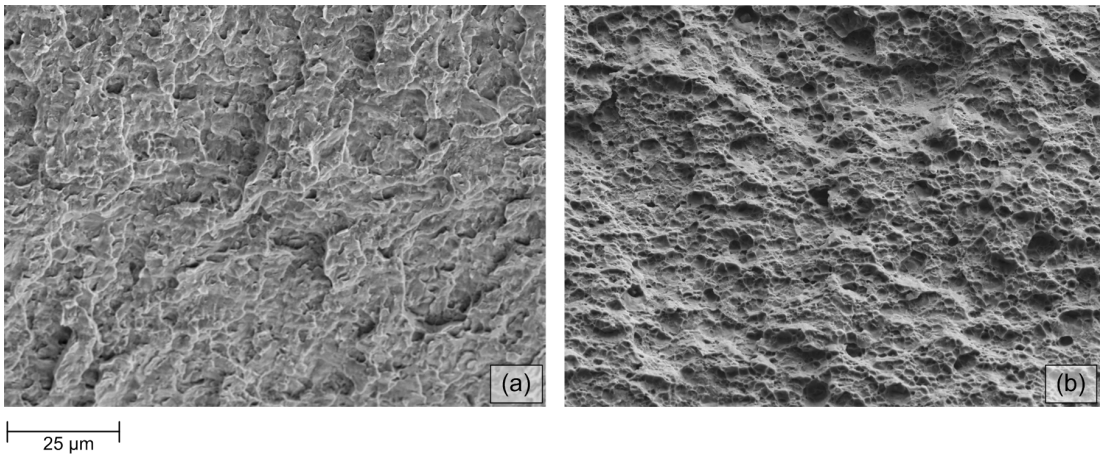

Figure 4.14: *Two different SEM (secondary electron) images showing the observed fracture mechanisms.* ***(a)*** *corresponds to location A in Figure 4.13 and* ***(b)*** *is at location B in the same figure.*

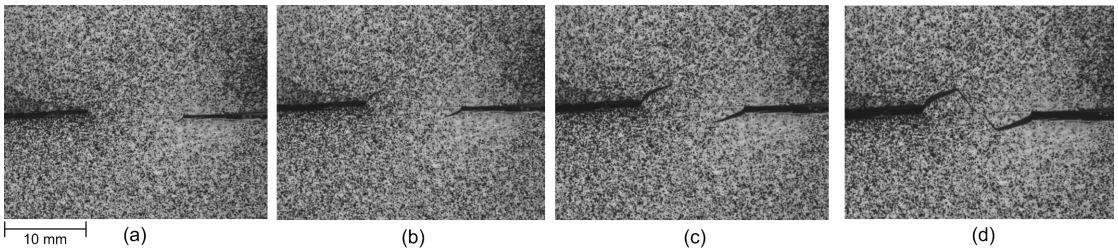

Figure 4.15: *Different stages of DP1000 during EWF testing;* ***(a)*** *Undeformed* ***(b)*** *After brittle crack increment, around the peak load* ***(c)*** *During stable crack propagation after the load is decreased* ***(d)*** *after complete fracture*

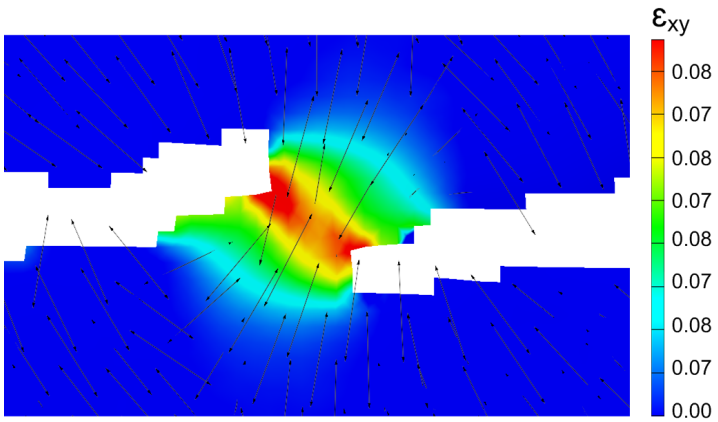

Figure 4.16: *Shear strain (ε_{xy}) distribution near the remaining ligament right before complete fracture takes place (Figure 4.15d). The local major strain directions are indicated with arrows.*

XPF1000 (1.8 mm)

The XPF1000 of 1.8 mm thickness measurements displays ambivalent behaviour during EWF testing whereby 'lower shelf' and 'higher shelf' cq. low work of fracture ($\pm$200 kJ/m^2) and high work of fracture data ($>$ 600 kJ/m^2) is obtained (see Figure 4.17). Statistically, the ratio of high toughness:low toughness samples is 1:3. This effect is visible in the force-displacement curves as well, as the high fracture toughness samples show much higher ductility during stable crack growth. No linear fit could be obtained from the largely scattered EWF data. Again, an unstable crack increment is created before the peak load as a result of the sheared notches. Macroscopic crack growth is observed if/when the force signal drops as before.

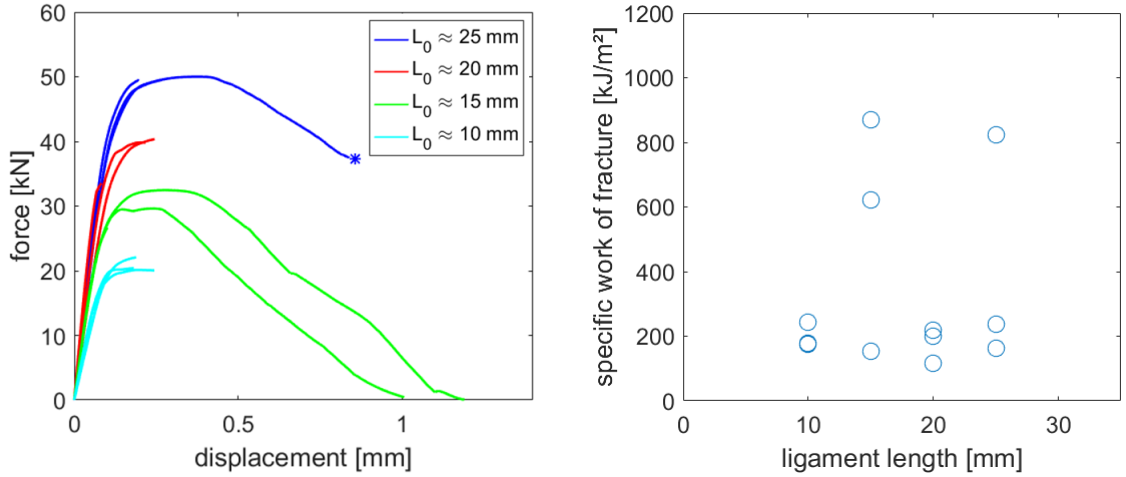

(a) Global force-displacement curves

(b) Specific work of fracture w_f

Figure 4.17: *EWF results for XPF1000 (1.8 mm thickness) with sheared notches. One measurement at $L_0 \approx 25$mm was ended before complete fracture and is marked (*).*

Strain analysis before fracture initiation confirms that no full ligament yielding takes place in the 'low toughness' specimens as in the 'high toughness' specimens (Figure 4.18). In addition, the strains in the high toughness sample are less diffuse and more concentrated around the ligament as can be

seen from the section plots in Figure 4.19. The steep increase in major strain around the center of the ligament is indicative of necking and is indeed confirmed by macroscopic fracture surface analysis (±55% contraction). The necking is however limited to the middle segment of the ligament, and it observed that during necking in this region the corresponding crack growth is less rapid. Local hardening in the necked ligament creates resistance to crack growth which essentially increases local fracture toughness. Different stages during testing are shown in Figure 4.22, showing a very different mechanism compared to the DP1000 samples. The XPF1000 (high fracture toughness samples) show clear necking in the center rather than the completely slant fracture observed in DP1000. The minor strain distribution is similar to the samples with a blunt EDM notch (see Figure A12 Appendix A.3).

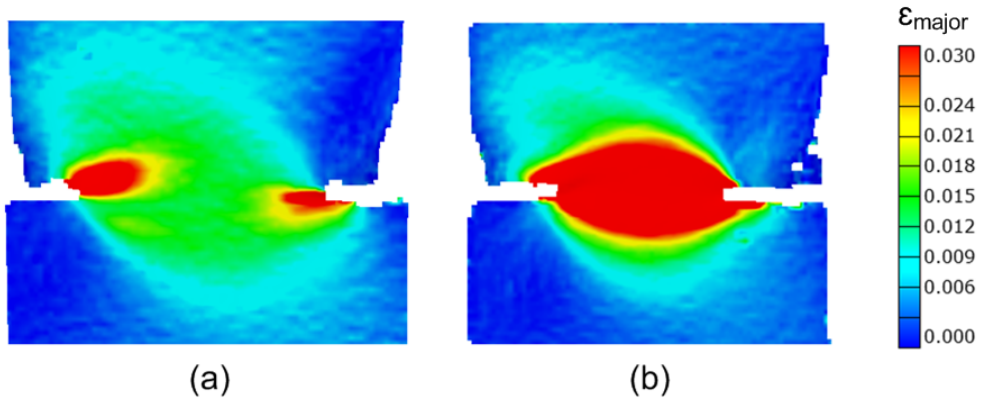

Figure 4.18: *Comparison of major strains before fracture initiation, showing the plastic zone difference between a low fracture toughness specimen (**a**) and high fracture toughness specimen (**b**).*

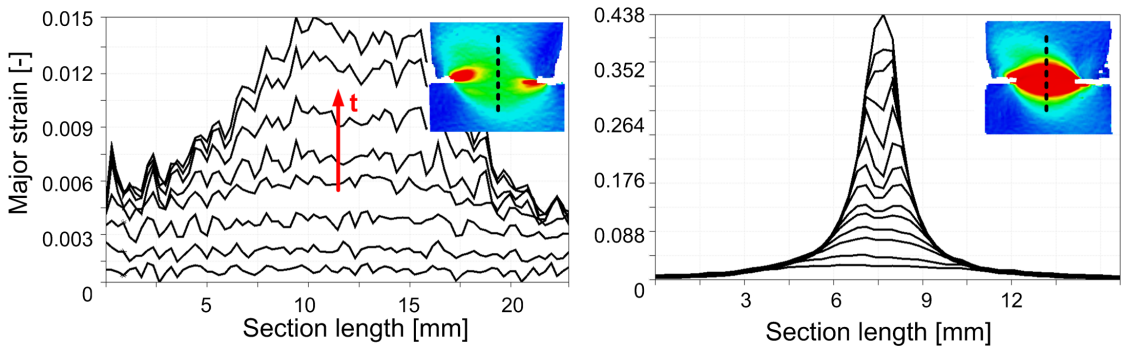

Figure 4.19: *Evolution of the major strain plotted against section length for a low fracture toughness (left) and high fracture toughness sample (right);* $L_0 \approx 15$ *mm.*

SEM investigations show again a mild distinction between the two types of samples at microscale. The low toughness samples show mostly signs of transgranular cleavage, except in the outer edges of the specimen a dimpled morphology is found indicative of microvoid coalescence (boundary region is shown in Figure 4.21c). At the edges a low plastic constraint i.e. plane stress state is present, presumably leading to the nucleation and growth of voids rather than triggering cleavage fracture (via brittle inclusion particles for example). Non-metallic inclusions (such as oxides) have been identified as nucleation sites leading to failure by microvoid coalescence. These particles are relatively large compared to the matrix, creating relatively large voids as a result (Figure A9 in Appendix A.3). The smaller voids are suspected to growth near grain boundaries, for example. Near the initiation region behind the sheared notch, a mixed-mode failure (microvoids and cleav-

age traces) is observed with a three-dimensional structure with both type of samples (Figure 4.21a). The fractured surface shows considerable height difference (in the direction of the paper) due to the combination of the shearing deformation followed by tensile deformation. This effect is even more pronounced around the center of the specimen, where the center-line delamination starts to play a role. This phenomenon is seen in the fatigue pre-cracked samples as well, and can thus be considered a material property independent of thickness or initiation method. The high toughness specimen show a (more flat) region of mixed-mode fracture in the bulk (Figure 4.21d) rather than completely ductile fracture. From these findings it can be concluded that a considerable degree of mixed-mode fracture is present at this temperature, which is typical in a ductile-to-brittle transition region.

Stress calculations at the ligament during peak load tell a similar story as the fatigue pre-cracked specimens; no distinction can be made between the low- and high fracture toughness samples (see Figure A11 in Appendix A.3). From the tensile curves this can also be predicted beforehand. It also demonstrates a certain degree of resilience of the material, as the maximum stress it can withstand before fracture after a crack/notch-type initiation remains practically constant. The stresses are however relatively independent of the ligament length and fall within the set criterion, which validates the choice of ligaments.

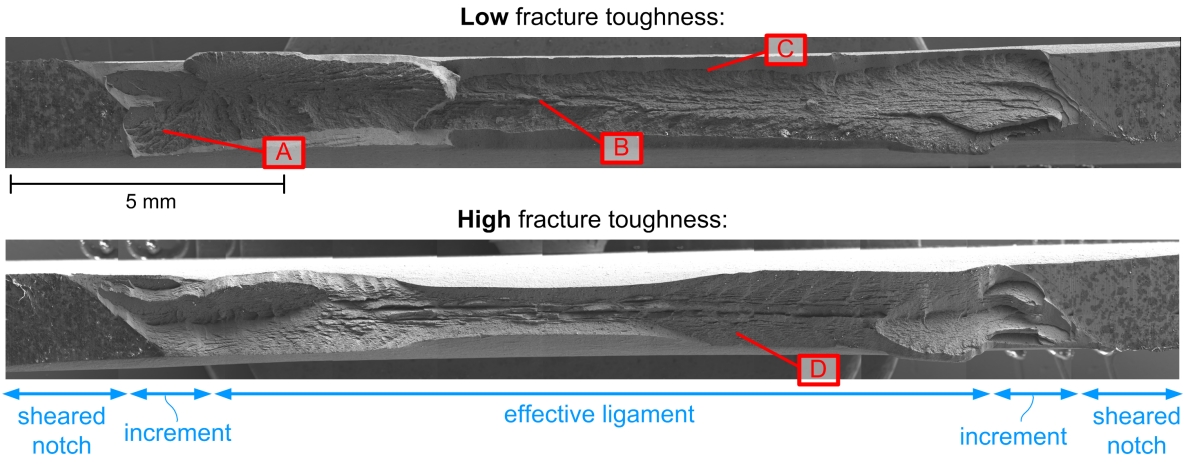

Figure 4.20: *SEM (secondary electrons) overview images showing an example of the two types of failed XPF1000 (1.8 mm thickness) specimens. The images share the same scale.*

XPF1000 (2.7 mm)

When examining the same material but at a larger thickness, an even lower range of w_f is measured throughout the test samples. The ratio of high toughness:low toughness samples is 0:1 in this situation. The force-displacement curves during EWF testing are shown in Figure 4.23 and the corresponding work of fracture data in Figure 4.24. No significant differences between the coated and uncoated samples are observed. The size of the brittle crack increment during testing, which is excluded from the yielding ligament area, is estimated by pausing the same EWF test at $\pm$ 90-95% of the peak load. White ink is pressure-infused into the notch afterwards and dried accordingly. The results show that the suspected cleavage-region indeed has failed before the remaining ligament and justifies the modified calculations (see: Figure A4 in Appendix A.1). It remains a matter of estimating the effective ligament area after a series of tests, rather than controlling the precise ligament area in the sample preparation step.

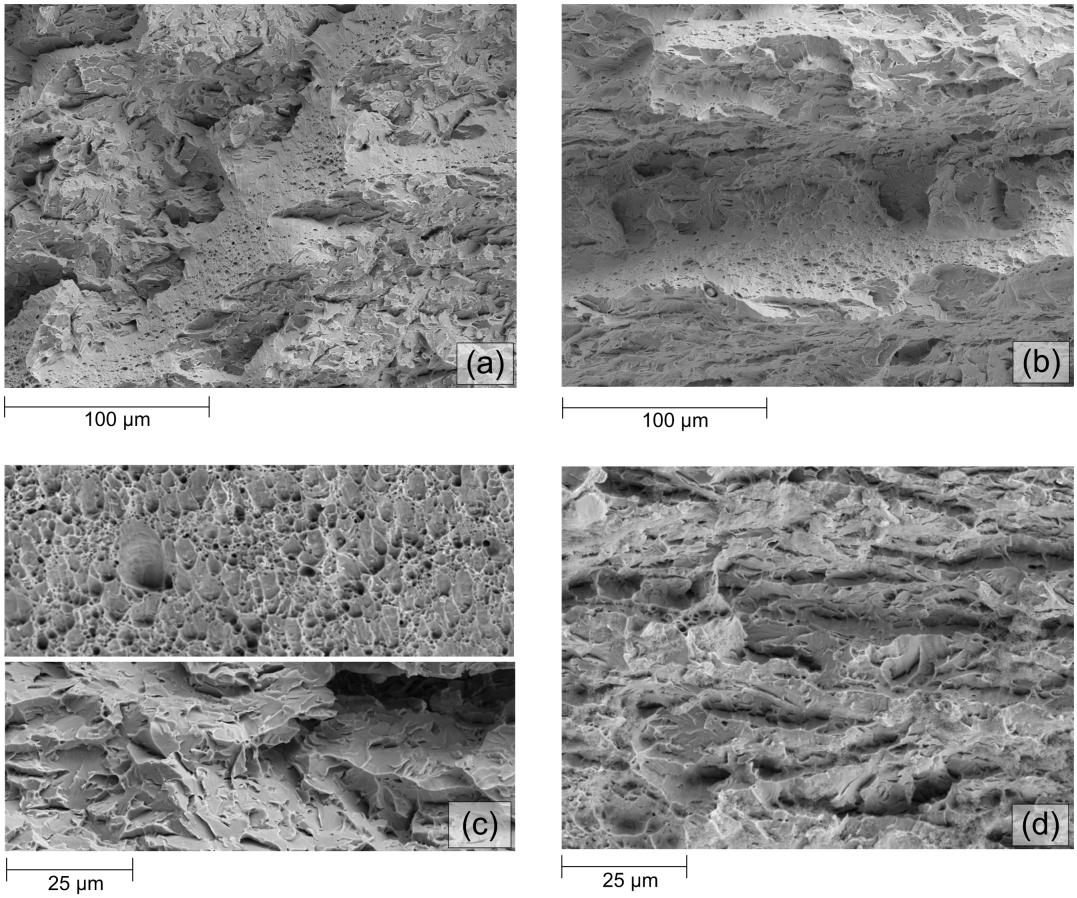

Figure 4.21: *SEM images:* ***(a)*** *Mixed-mode failure in the extended fracture initiation region after the sheared notch, following the 45^o orientation* ***(b)*** *Mixed-mode failure in the center-line showing a horizontal V-shaped morphology* ***(c)*** *The boundary between cleavage fracture and microvoid coalescence* ***(d)*** *Mixed mode fracture. The regions correspond to the labels in Figure 4.20.*

The same trend is observed as with the 1.8 mm thickness; scattered work of fracture data from which no linear fit can be generated to find an *essential* work of fracture. The samples often fail without significant strain hardening and stable crack growth, which is reflected by the lack of a plastic dissipation coefficient βw_p (no slope) as there is no large-scale plasticity in the ligament. SEM investigations show the same type of fractured surface as with the 1.8 mm samples, with mostly cleavage fracture and mixed-mode fracture near the center-line (delamination). Because of this obvious mixed-mode fracture, the tests were repeated at elevated temperatures to check for the effect of a ductile-to-brittle transition. This was done at 60, 100 and 120 ^{o}C as explained before. The potential increase in fracture toughness is then related to the responsible fracture micro-mechanisms in the material to establish the link.

The results for all the chosen temperatures are shown together in Figure 4.26. Increasing the temperature by approximately 100 ^{o}C leads to a drastic increase in the work of fracture measured. This effect can be ascribed to the added thermal energy to overcome the lattice barriers naturally occurring in a BCC metal. Plasticity via dislocation glide along the slip planes is facilitated and causes a completely different mechanical response (see Figure A15 in Appendix A.3). The increase in plastic zone confirms this as well (see Figure 4.25). At room temperature the ligament is not fully yielded, thereby establishing the failed EWF-method for this steel in these experimental conditions. At 60

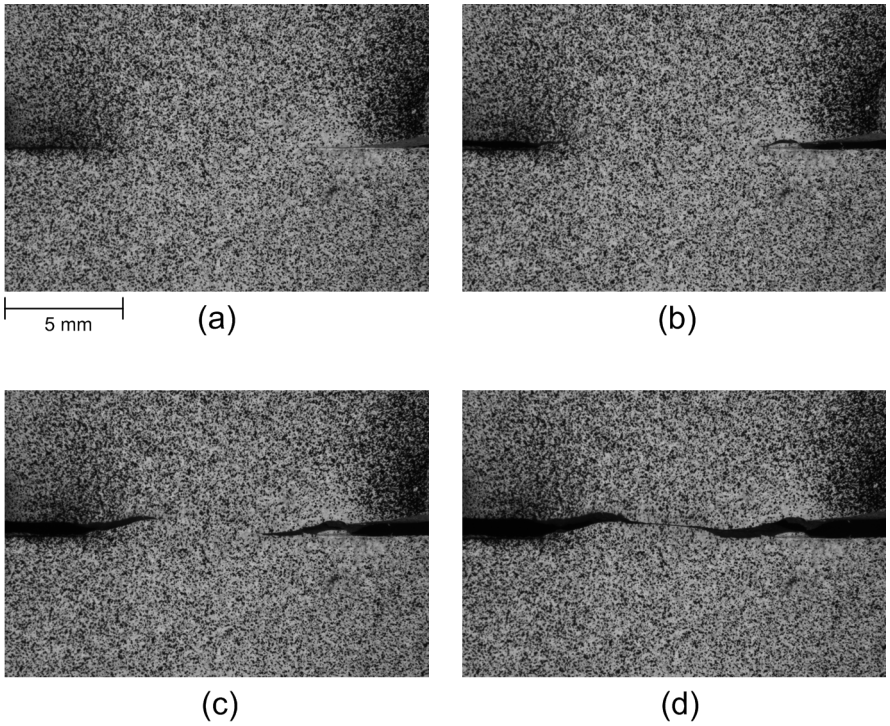

Figure 4.22: *Different stages of XPF1000 during EWF testing;* ***(a)*** *Undeformed* ***(b)*** *After brittle crack increment, around the peak load* ***(c)*** *During crack growth and necking* ***(d)*** *after complete fracture.*

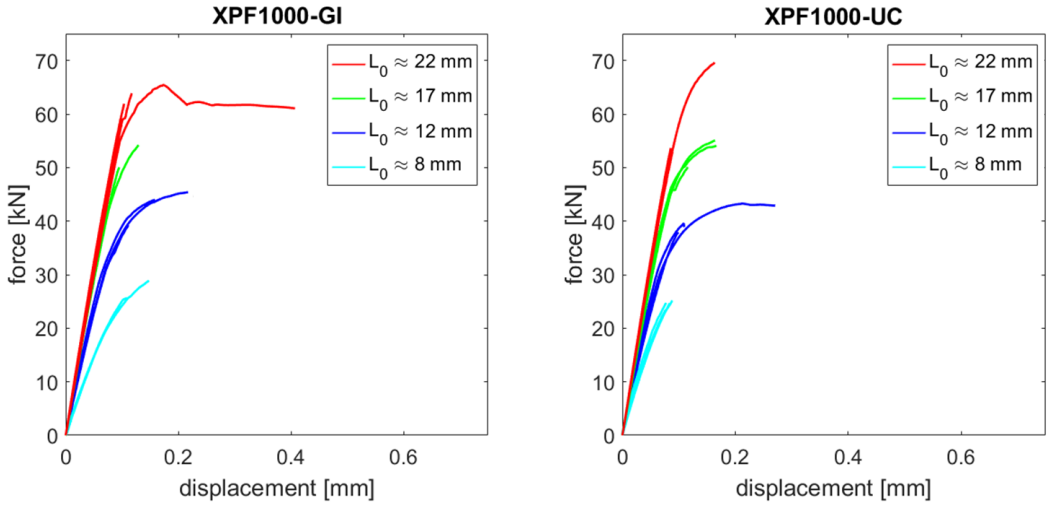

Figure 4.23: *Global force-displacement curves obtained during EWF testing of XPF1000 samples with sheared notches (2.7 mm thickness).*

^{o}C, already a decent portion ($\pm$50%) of specimens failed accompanied with stable crack growth and necking, showing higher ductility and work of fracture.

Fracture surface analysis endorses the positive effects of temperature on the fracture behaviour, as the high-temperature samples show larger amounts of ductile tearing i.e. microvoid coalescence rather than cleavage fracture. The amount of necking in the samples increases as a function of temperature too, up to the point that a slant fracture is more dominant (similar to DP1000) and suppresses

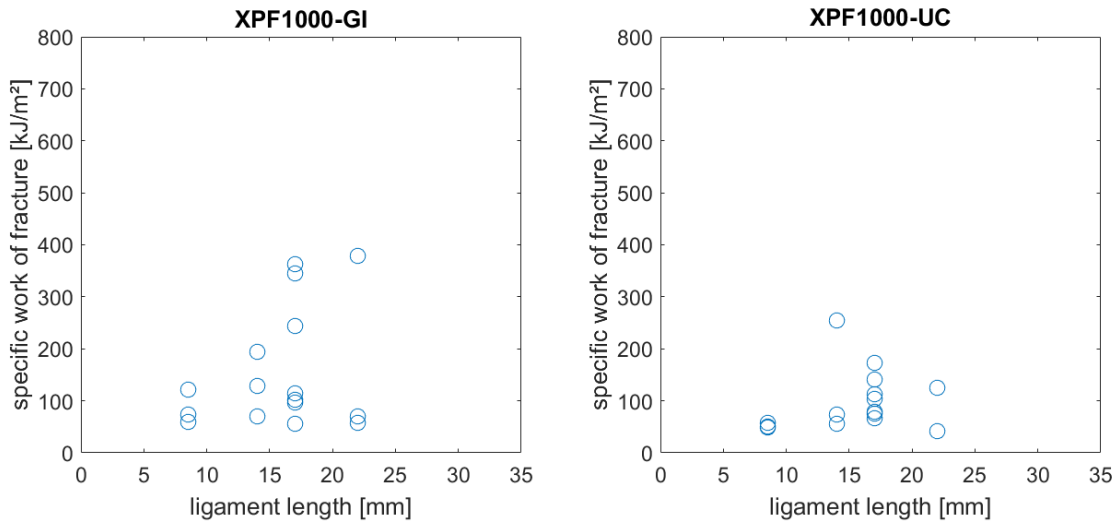

Figure 4.24: *Specific work of fracture w_f of sheared-notch sampels of XPF1000 (2.7 mm thickness) as a function of ligament length L_0. No linear fit could be obtained from the scattered data.*

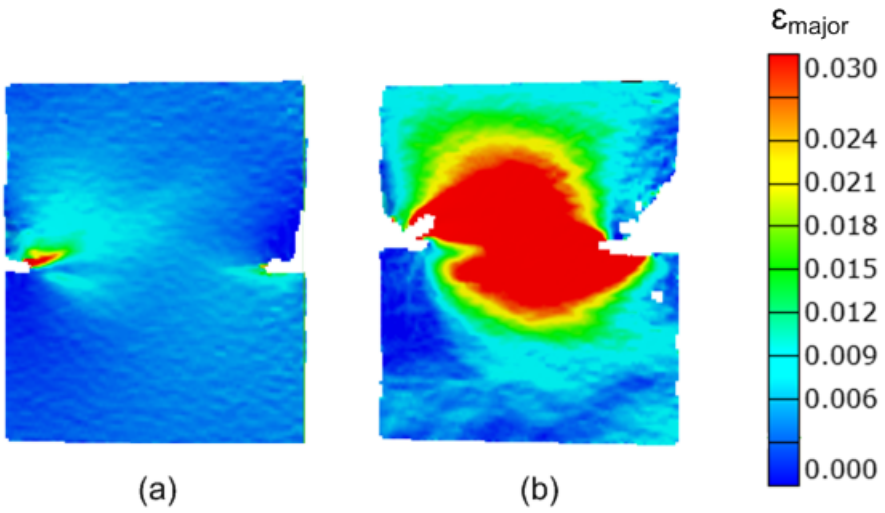

Figure 4.25: *Comparison of major strain distributions before fracture initation, showing the difference between (a) 20 °C and (b) 60 °C.*

necking in the center. Delamination at the center-line (probably due to core segregation) continues to weaken the material, although it seems to withdraw at 120 °C to a limited region only. The different fracture surfaces are illustrated in Figure 4.28. An additional overview image taken from an angle is stored in Figure A14 in Appendix A.3.

To estimate the ductile-to-brittle transition (DBT), the work of fracture data from a constant ligament length is evaluated at different temperatures. The work of fracture still contains the plastic dissipation coefficient however, therefore it is assumed to be (more or less) constant since the ligament volume is constant as well. Figure 4.27 shows that the there is indeed indication that there exists a lower-shelf 'toughness' value and a upper-shelf based on the spread of results (for both type of samples the same distribution function is applied). However, for the uncoated samples the up-

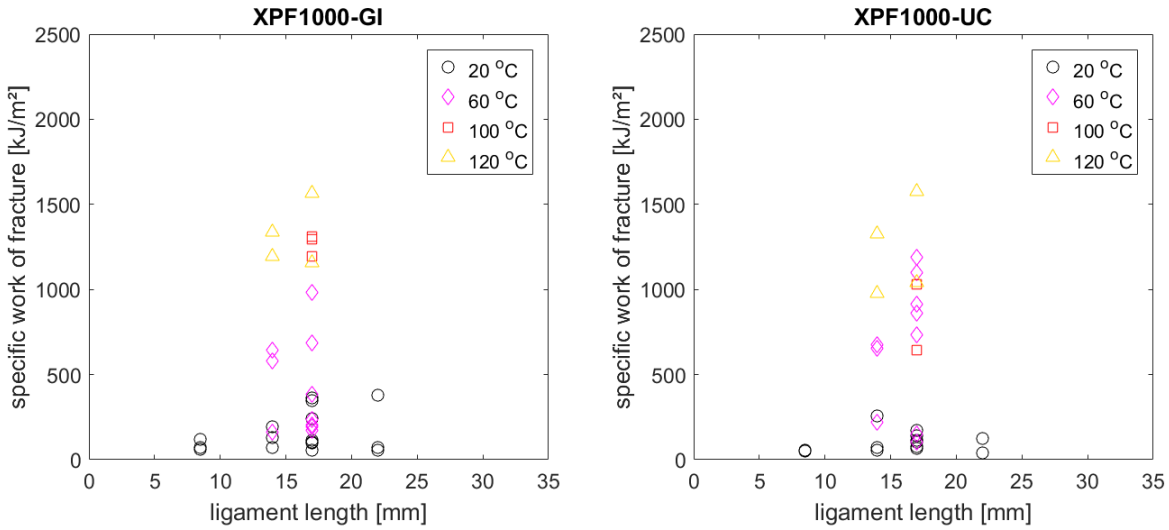

Figure 4.26: *Specific work of fracture w_f of sheared-notch sampels of XPF1000 (2.7 mm thickness) as a function of ligament length L_0 for a range of temperatures.*

per shelf values contain high variance and can therefore not be considered definite. The transition curve is merely included as an indicative trendline rather than a precise approximation of the DBT. A Weibull cumulative distribution function is used in the form of:

$$F(T,k,\lambda) = 1 - \exp(-T/\lambda)^k + C \tag{4.28}$$

Where T is the temperature in °C, λ the scale parameter, k the shape parameter and C a constant used as a vertical offset (lower shelf values).

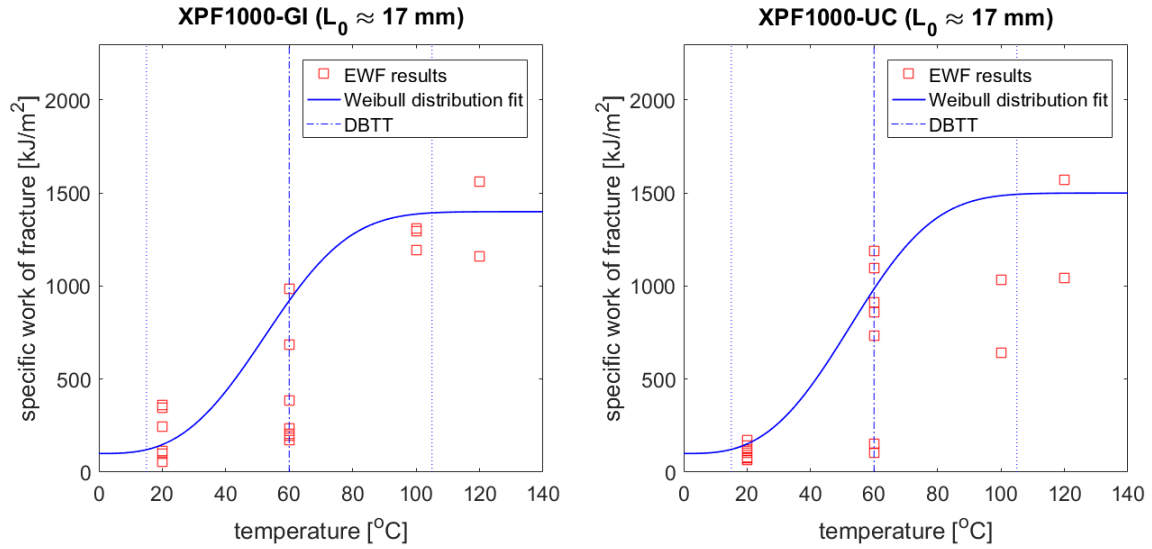

Figure 4.27: *Ductile-to-brittle transformation curve of XPF1000 (2.7 mm thickness) estimated with w_f from EWF testing.*

It was discovered with infrared field measurements that the temperature in the ligament fluctuates considerably during testing at 100 and 120 °C. As this is where the plasticity and crack growth actually occurs, deviations must be kept to a minimum for a reliable test result. The temperature

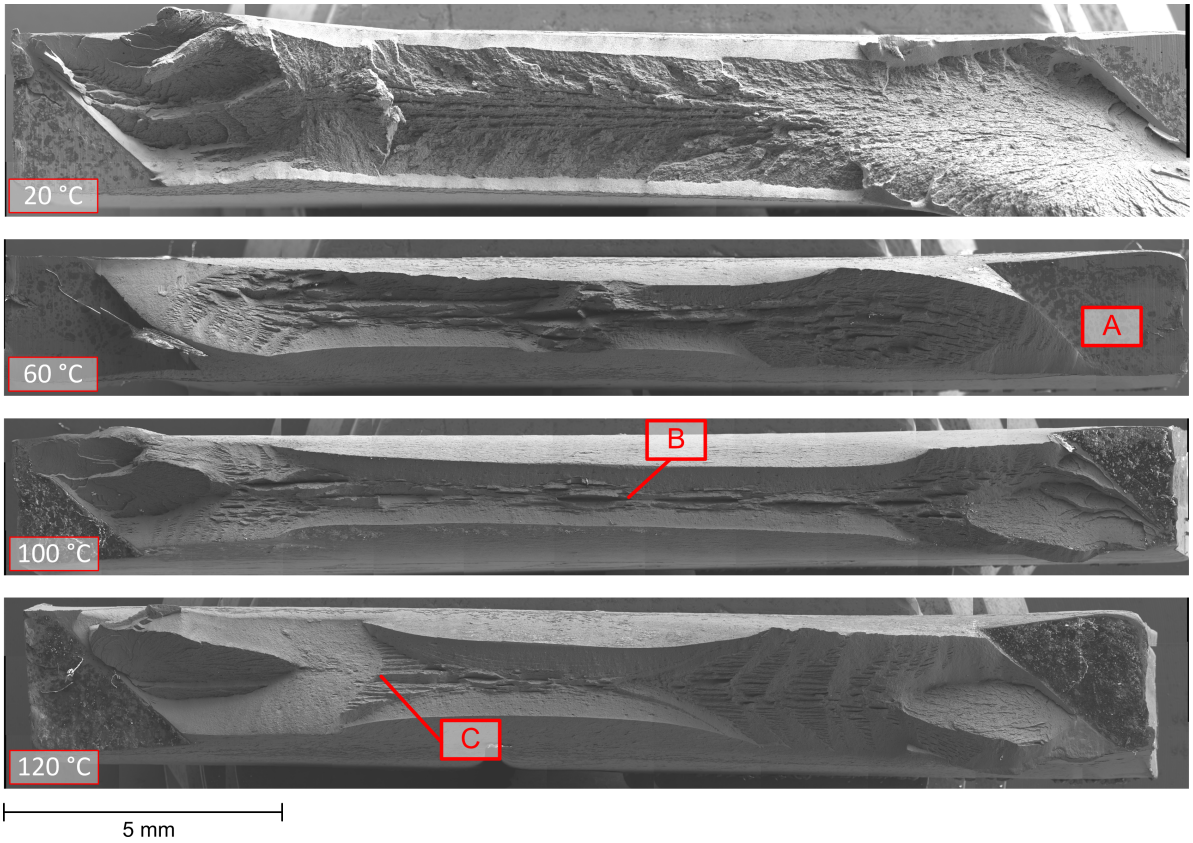

Figure 4.28: *SEM (secondary electrons) overview images showing examples of the fractured surface for a range of temperatures (XPF1000 2.7 mm thickness). The images share the same scale.*

control at 60 °C was fairly successful though. The temperature gradient across the ligament (horizontally and vertically) were estimated to be ± 2 °C (see Figure A18 in Appendix A.3) Temperature deviations in time were estimated by logging the peak temperatures inside a specified region inside the ligament. Additionally, the temperature of the surroundings were logged as well by taking the average temperature before the notch, which is essentially a free surface uninfluenced by plastic processes (see Figure A17 in Appendix A.3). The infrared images show the heat dissipation as a result of plastic processes in the material, which are similar to the observations from the strain fields and global displacement data. At 60 °C there is still some degree of brittleness (seen as sudden load drop) which shows as short peaks in temperature from the initiation of fracture until failure (Figure 4.30). At 120 °C the crack growth is stable (seen as gradual load decrease) and shows taller peaks in temperature until fracture. In Figure A13 (Appendix A.3) the heat images are shown visually.

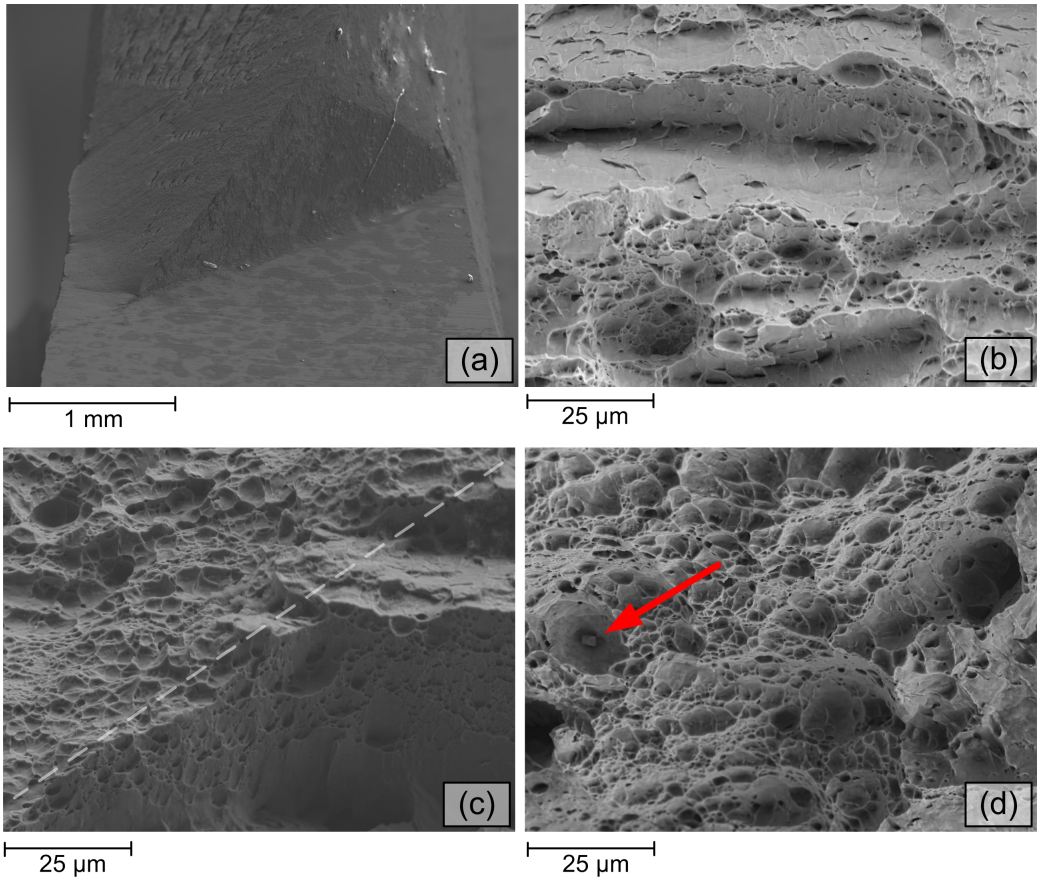

Figure 4.29: *SEM images:* ***(a)*** *Side profile of notch, showing the initiation of slant fracture* ***(b)*** *Mixed-mode fracture along the center-line* ***(c)*** *boundary between ductile tearing (left) and mixed-mode fracture (right)* ***(d)*** *large inclusion that has acted as a void nucleation site, creating a large void as a result. The regions correspond to the labels in Figure 4.28*

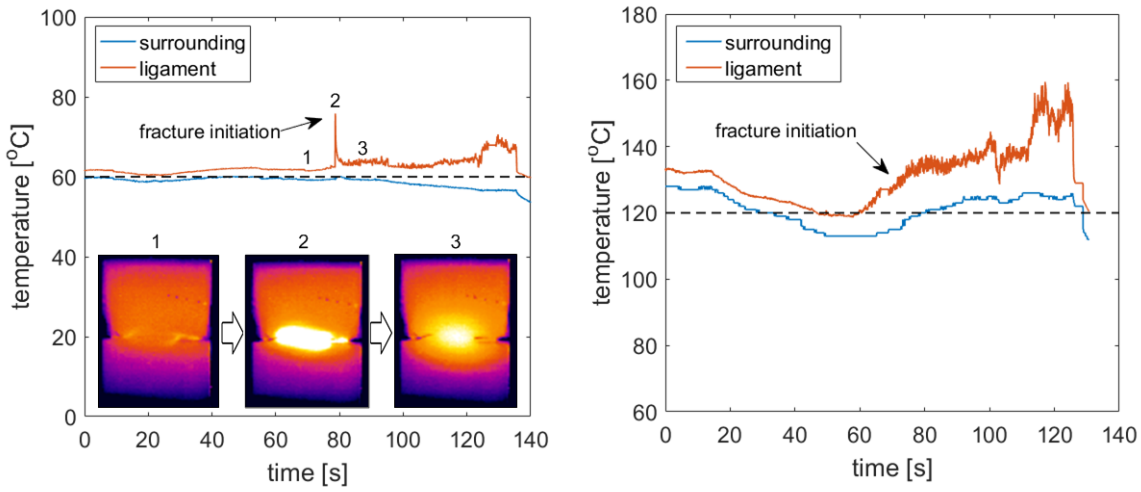

Figure 4.30: *Temperature measurements in time during EWF testing at 60 °C (left) and 120 °C (right).*

XPF1000 (2.9 mm)

The last single-phase grade is the XPF1000 with a slightly higher thickness (2.9 mm instead of 2.7 mm). It behaved rather similar as the 2.7 mm material, showing the same brittle behaviour and unstable rapid crack growth. Figure 4.31a shows the load-displacement curves along with the EWF results in Figure 4.31b. From the load-displacement curves no strain hardening can be identified. A global engineering strain of merely ±0.5% is measured at the point of complete failure. The net sectional stresses as a function of the ligament are shown in Figure A24 in Appendix A.3, validating the chosen ligament with respect to the imposed stress criterion. No fracture toughness could be obtained (w_e) with the essential work of fracture methodology.

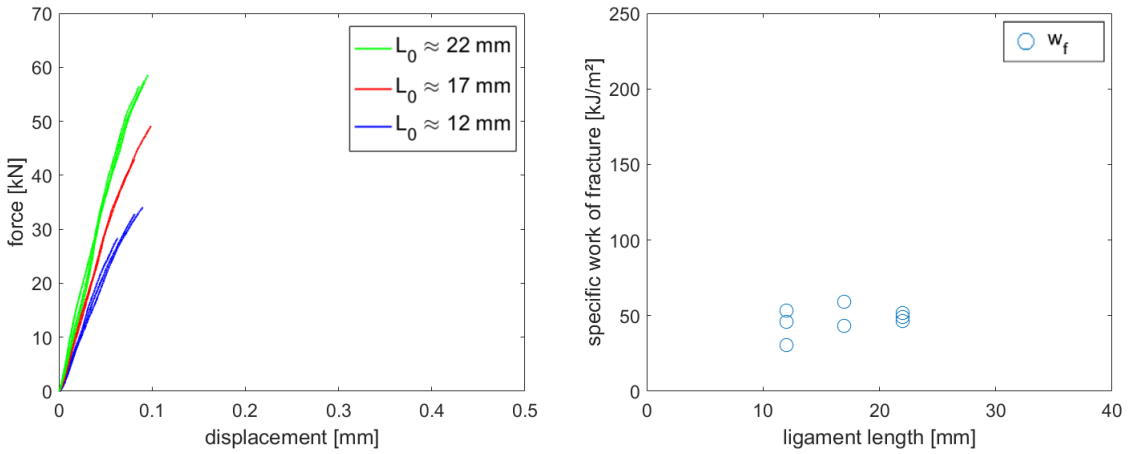

(a) Global force-displacement curves

(b) Specific work of fracture w_f

Figure 4.31: *EWF results of XPF1000-UC (2.9 mm thickness) with sheared notches.*

XPF800 (3.2 mm)

The XPF800 results with sheared notches corresponds well with the findings from the fatigue pre-cracked samples; the samples show a much higher ductility compared to XPF1000 and failure is accompanied with stable crack growth. Figure 4.32 shows the load-displacement curves along with the EWF results. From the load-displacement curves the strain hardening and stable crack growth can be identified (flattening of the curve and subsequent gradual decrease of load). A global engineering strain of up to 10% is measured at the point of complete failure. The linear regression line is fairly successfully found (R^2 = 0.75) and delivers an essential work of fracture of 497 kJ/m^2. The net sectional stresses are independent of the ligament length and fall within the previously set criteria for plane stress failure (see Appendix A.3). No additional fracture surface analysis was performed here.

CP800 (3.3 mm)

For the CP800 (3.3 mm thickness) material another successful application of the essential work of fracture methodology is achieved. Figure 4.33a shows the load-displacement curves along with the EWF results in Figure 4.33b. From the load-displacement curves the strain hardening and stable crack growth can be identified (flattening of the curve and subsequent gradual decrease of load). A global engineering strain of up to 11% is measured at the point of complete failure. The linear regression line is fairly successfully found (R^2 = 0.83) and delivers an essential work of fracture of 397 kJ/m^2. The net sectional stresses are independent of the ligament length and fall within the

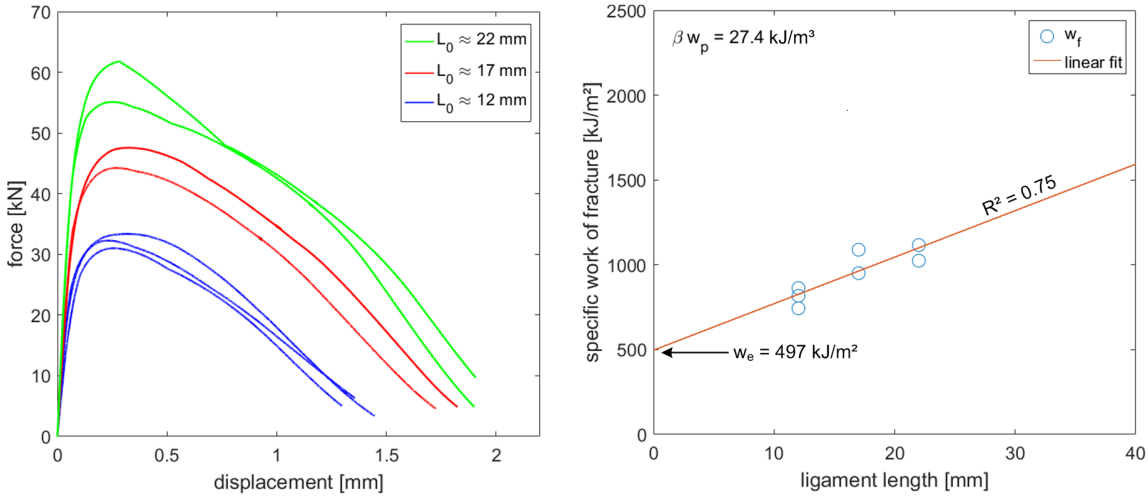

(a) Global force-displacement curves

(b) Specific work of fracture w_f

Figure 4.32: *EWF results of XPF800-UC (3.2 mm thickness) with sheared notches.*

previously set criteria for plane stress failure (see Appendix A.3). No additional fracture surface analysis was performed here.

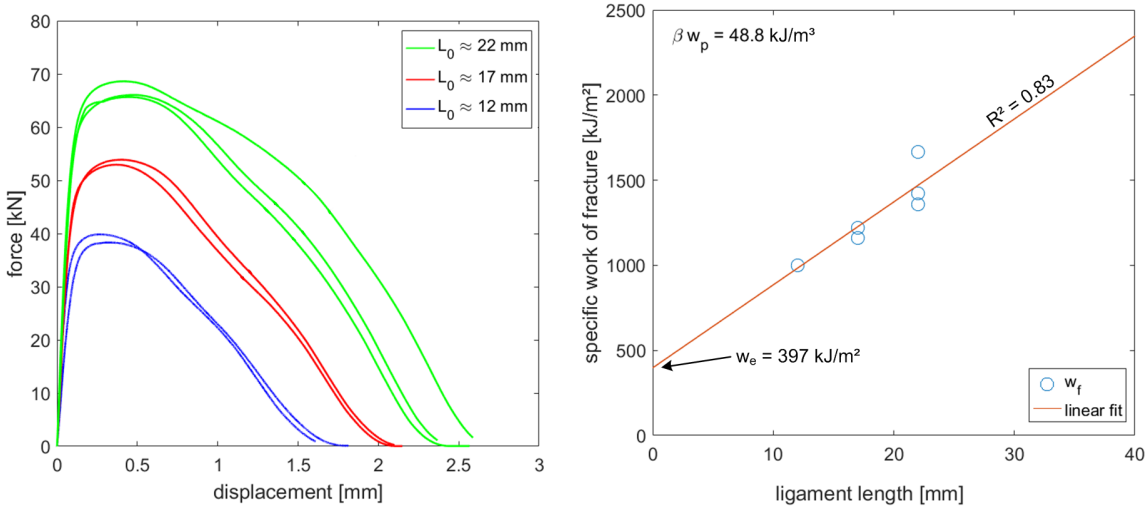

(a) Global force-displacement curves

(b) Specific work of fracture w_f

Figure 4.33: *EWF results of CP800-UC (3.3 mm thickness) with sheared notches.*

CP800 (4.0 mm)

The complex-phase steel with 4.0 mm thickness was evaluated as well, and showed a very robust mechanical response in the sense that the force-displacement curves showed very similar characteristics for all samples. The force-displacement curves are shown in Figure 4.34a as well as the essential work of fracture results in Figure 4.34b. All specimens failed with an appreciable degree of stable crack growth and showed necking throughout the samples. As this was the material with the

higher thickness, it was expected to be more susceptible to brittle-like behaviour due to higher stress-triaxiality ahead of the sheared notch i.e. a plane strain state. From a general material-applications perspective however, it was known beforehand that it did not show unexpected cracking behaviour during forming.

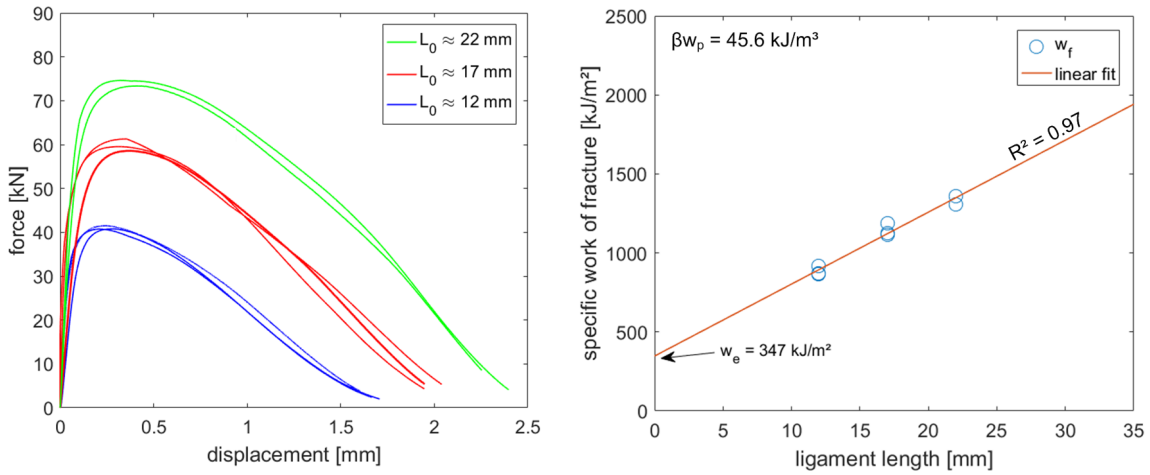

(a) Global force-displacement curves

(b) Specific work of fracture w_f

Figure 4.34: *EWF results of CP800-UC (4.0 mm thickness) with sheared notches.*

The obtained essential work of fracture is significantly higher (approximately 10 times) than the value obtained from DP1000, as well as having a much higher plastic dissipation factor. A lower tensile strength often corresponds to higher ductility and fracture toughness, demonstrated by this 200 MPa difference. The linear fit was accurately obtained (R^2 = 0.97) due to the nearly identical force displacement curves. From the DIC measurements the major strain distributions before fracture are retrieved, and show ligament yielding before fracture to satisfy the criteria for EWF testing (Figure 4.35). The strains are highly localized around the ligament and grow up to 90% (engineering strain) before fracture. Furthermore, the net sectional stresses around the peak force are within the stress criterion imposed earlier, suggesting that plane stress conditions are met even in this relatively thick (4.0 mm) material (see Figure A19 in Appendix A.3). This confirms that indeed a far-developed plastic zone is achieved during the fracture toughness testing.

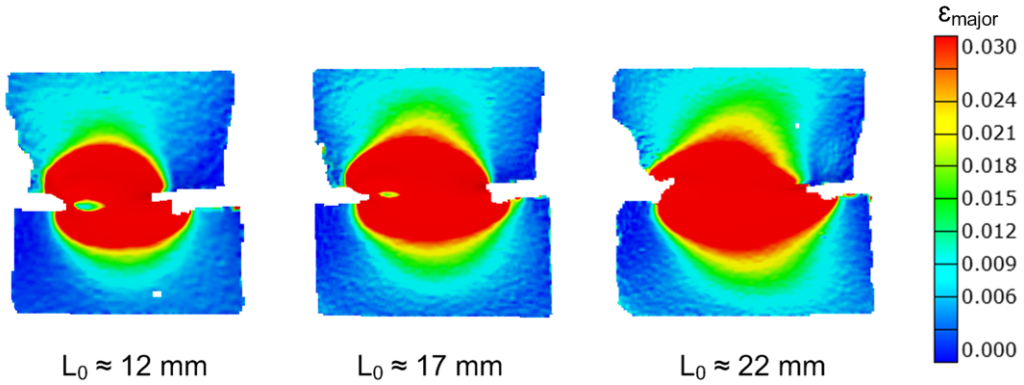

Figure 4.35: *Major strain distributions of CP800-UC with sheared notches (4.0 mm thickness) for three different ligament lengths.*

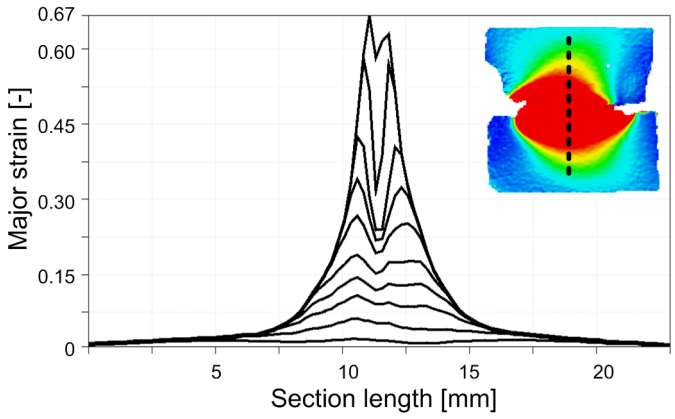

Figure 4.36: *Evolution of the major strain plotted against section length for CP800 (4.0 mm thickness) with $L_0 \approx 22$ mm.*

S550MC (3.0 mm)

The HSLA steel also shows ductile behaviour that results in linearly increasing work of fracture between ligament lengths. Figure 4.45 shows the load-displacement curves along with the EWF results in Figure 4.37b. From the load-displacement curves the strain hardening and stable crack growth can be identified (flattening of the curve and subsequent gradual decrease of load). A global engineering strain of up to 10% is measured at the point of complete failure. The linear regression line is fairly successfully found (R^2 = 0.76) and delivers an essential work of fracture of 650 kJ/m^2. This is also the highest measured fracture toughness parameter of all investigated materials. The net sectional stresses are independent of the ligament length but fall slightly above the previously set criteria for plane stress failure (see Figure A27 in Appendix A.3). This effect was found with the fatigue pre-cracked samples as well, as will be presented in the next section.

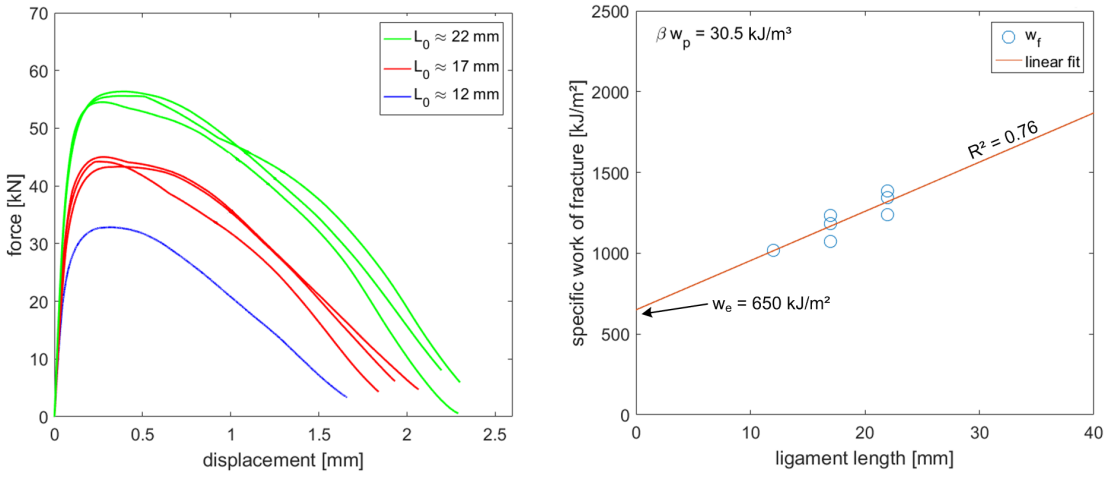

(a) Global force-displacement

(b) Specific work of fracture w_f

Figure 4.37: *EWF results of S550MC (3.0 mm thickness) with sheared notches.*

Fatigue pre-crack

The fracture toughness results from the CuttingEdge project are presented here. As a result of fatigue pre-cracking the exact ligament lengths varied somewhat compared to the specimen list presented earlier (these were determined from the fractured surfaces afterwards). Therefore the graphs consist of a distribution of ligament lengths, rather than discrete sets as before. The actual XPF1000 samples were obtained from the project for a more detailed examination; while the results of the remaining materials are only treated briefly. At the end of the chapter an overview and validation with the sheared notches is presented.

XPF1000 (2.9 mm)

The first of the investigated materials is the single-phase XPF1000 grade. During testing it was also found that not all specimens failed in the expected ductile mode, but instead displayed ambivalent fracture behaviour. Samples that failed in a brittle-like fashion showed a relatively low toughness, while the samples that failed in a ductile-type of fracture showed a much higher toughness. Statistically, the distribution of both samples is roughly 50/50. This duality is clearly observed both in the load-displacement curves and work of fractures collected in Figure 4.38. The two types of failure are highlighted in both graphs for illustration purposes.

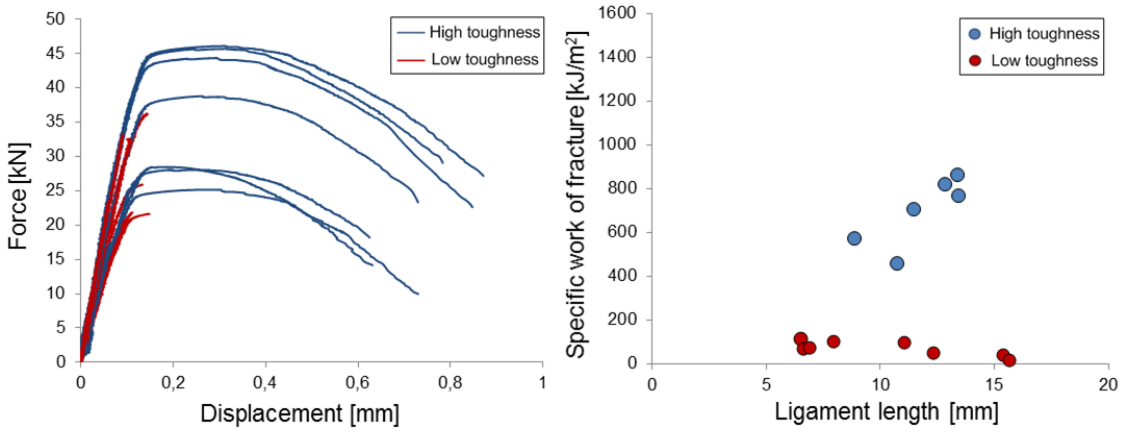

Figure 4.38: *EWF results for fatigue pre-cracked XPF1000-UC (2.9 mm thickness) [27]*

From the EWF results (Figure 4.38) it can be seen that the 'low toughness' values are independent of the ligament length. This can be explained by the absence of (large-scale) plasticity before fracture, as the specimens fail before (or directly after) reaching the maximum tensile strength without appreciable strain hardening. Full-field strain analysis shows the difference in strain and endorses the suspected absence of plasticity (Figure 4.39). Macroscopic fracture surface investigations show a clear distinction between the two types of failure: the 'low toughness' samples show a flat fracture surface with chevron-marks and without necking, while the 'high fracture toughness' samples show a large degree of necking ($\pm$55% contraction) before fracture (Figure 4.40). Specimens that experience necking benefit from local hardening in the ligament, resisting crack growth during ductile tearing. SEM investigations confirm that the fracture mechanisms are indeed primarily transgranular cleavage and microvoid coalescence for the brittle and ductile samples, respectively (Figure 4.41). The introduction of the fatigue pre-crack is investigated and confirmed as well (Figure A20 in Appendix A.3).

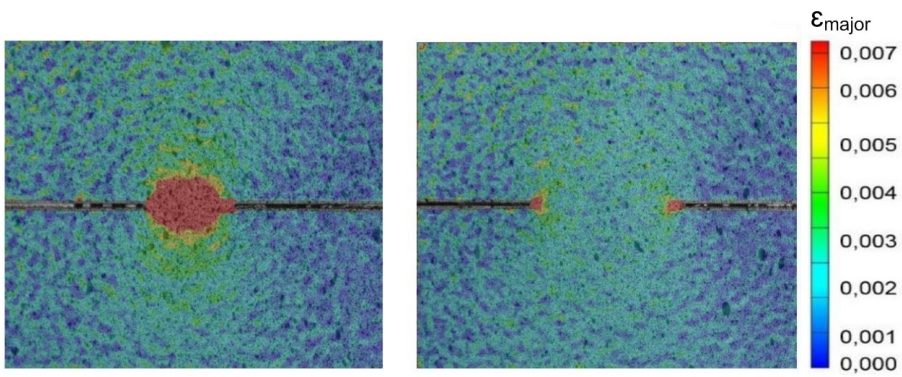

Figure 4.39: *Major strain distributions of fatigue pre-cracked XPF1000-UC at fracture initiation, showing the difference between a high fracture toughness samples (left) and low fracture toughness sample (right).[27]*

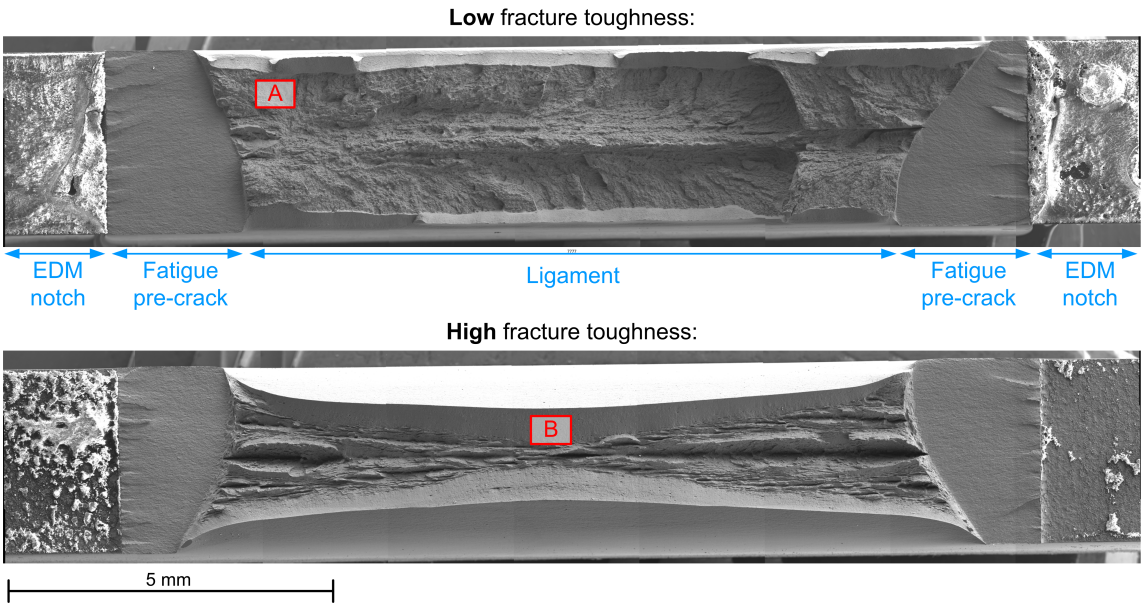

Figure 4.40: *SEM (secondary electrons) overview images showing an example of the two types of failed specimens. The images share the same scale.*

While the fracture surface of the brittle sample is largely consistent, the ductile samples show more obvious features of delamination (Figure 4.41). The regions wherein this occurs show a V-shaped lamellar morphology wherein a mixed-mode of brittle and ductile behaviour is displayed in the form of cleavage traces and microvoids. The delamination is likely the effect of core segregation; a phenomena that is not uncommon for these steels according to prior research at Tata Steel. This effect is stronger towards the initiations i.e. fatigue pre-cracks and reduces somewhat towards the center of the ligament where the necking reaches a maximum. Plane stress conditions near the free edges of the specimen may counter the effect of delamination while a high stress-triaxiality near the crack-tip and center-line can worsen it.

Core segregation is a consequence of inhomogeneous solidification throughout the thickness dur-

ing casting of the steel. This causes alloying elements to diffuse towards the solidified front i.e. the center of the slab and enriches it with cleavage-triggering particles essentially. A soft-reduction step is often included to redistribute these particles more dispersedly over the thickness, however the issues is not eliminated completely. The elevated stress levels ahead of the crack-tip can cause these particles to fracture and trigger the event of cleavage fracture. A chemical analysis from the fractured surfaces should reveal the traces of these inclusions at the origins of cleavage fracture initiation. A more detailed understanding of (macroscopic) core segregation and delamination can be gained from specialized literature.

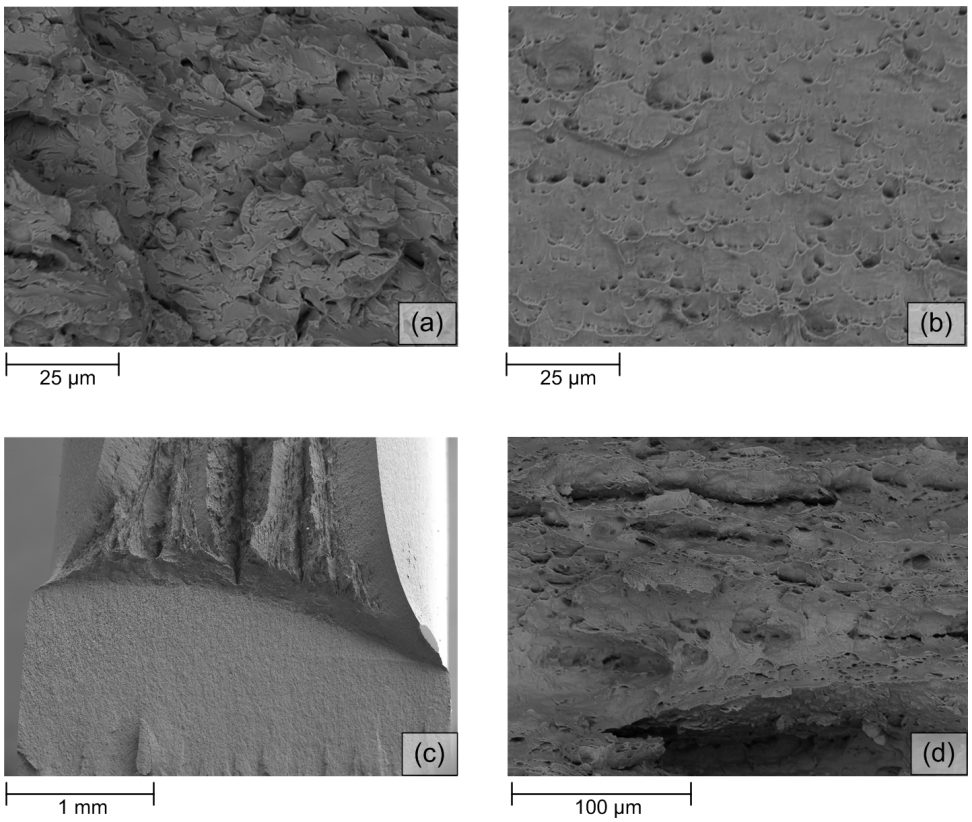

Figure 4.41: *SEM images:* ***(a)*** *transgranular cleavage fracture from location A in the Figure 4.40* ***(b)*** *stretched shear dimples indicating ductile failure from location B in Figure 4.40* ***(c)*** *close-up of the fracture initation region highlighting the V-shaped morphology* ***(d)*** *close-up of the mixed-mode fracture at the center-line of the high fracture toughness sample.*

The shapes of the crack fronts reveal an error as well; the convex shape is not symmetrical and reveal a possible misalignment in the resonance fatigue machine during cyclic loading. Presumably an out-of-plane bending moment caused the cracks to grow unevenly. Figure 4.40 clearly displays this. The presented examples were not isolated incidents and are representative for the whole pool. The uneven crack growth can also be explained by a possible gradient of mechanical properties as a function of the thickness, due to faulty process control in production for example. The introduction of the fatigue pre-crack was quite challenging - several other samples (not shown here) were useless because of singular crack growth at one notch instead of both, to give an example.

Stress analysis of the ligaments is applied again to assess the validity of the plane stress state and ligament-yielding. The same procedure is followed as before and the maximum net sectional stresses

are plotted as a function of the ligament lengths (Figure 4.42). While the majority of samples are within $\pm$ 10% of the assigned stress criterion and independent of the ligament length, four test results were outside the chosen boundaries. While the first two stress values are still within $0.9\sigma_Y$, the two lowest stress values (at $L_0 \approx 16$ mm) are severely outside the limits. No clear distinction can be made between the low fracture toughness and high fracture toughness samples in this graph. In conclusion, the maximum net sectional stress cannot be used to verify whether the specimens failed as a result of full ligament yielding. This can be explained by the fact that the stress is calculated at the peak load; this same peak load is often reached in both type of samples regardless of the subsequent occurrence of large-scale plasticity. In reality the stress levels in the high fracture toughness samples become much higher due to area reduction (necking), which is not reflected due to the use of the initial ligament area A_0 in the calculations. The datapoints with drastically low stress values should be examined further with the fractured surfaces, and excluded from the EWF calculations in any case.

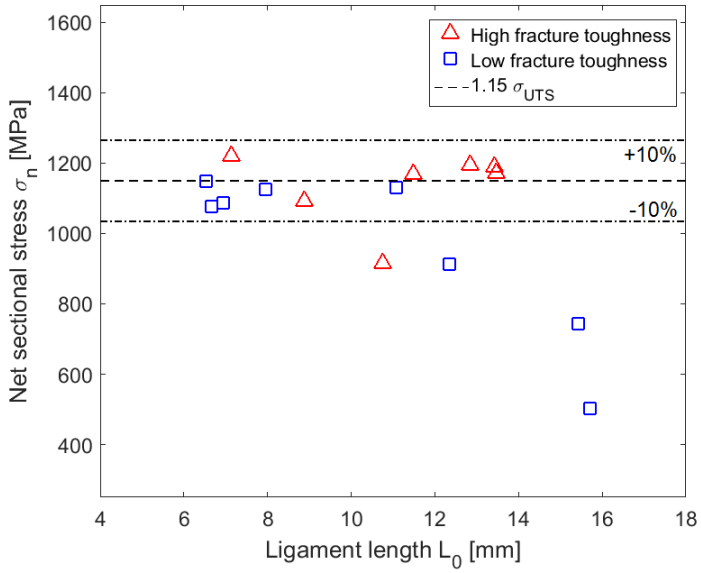

Figure 4.42: *Maximum net sectional stress as a function of the ligament length experienced during EWF testing of XPF1000 (2.9 mm thickness) with a fatigue pre-crack. The stress criterion is included here with a $\pm$ 10% interval.*

XPF800 (3.2 mm)

The next single-phase grade is the XPF800 which similar to the XPF1000 albeit with a lower degree of precipitation, responsible for the 200 MPa strength difference. Figure 4.43 shows the load-displacement curves along with the EWF results. From the load-displacement curves the strain hardening and stable crack growth can be identified (flattening of the curve and subsequent gradual decrease of load). A global engineering strain of up to 3% is measured at the point of complete failure. The linear regression line is fairly successfully found (R^2 = 0.85) and delivers an essential work of fracture of 478 kJ/m^2. The net sectional stresses are independent of the ligament length and fall within the previously set criteria for plane stress failure (see Figure A21 in Appendix A.3). It is suspected that the lower degree of precipitates (compared to XPF1000) facilitates the movement of shielding dislocations that move from the neighboring grain boundaries towards the crack-tip. Less dislocation pile-up is created which allows for crystal plasticity and decreases the tendency of brittle cleavage initiation. Thus, the fracture toughness is increased relative to the XPF1000.

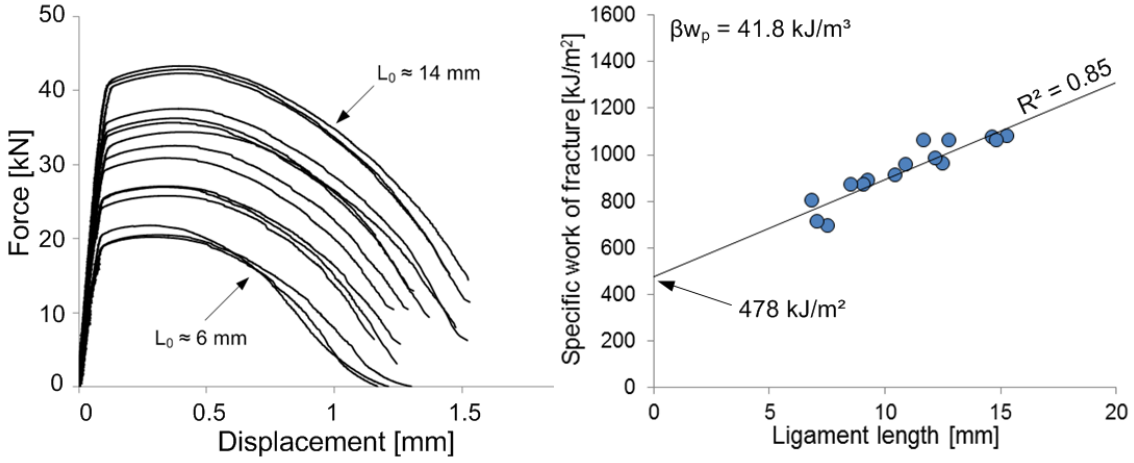

Figure 4.43: *EWF results of fatigue pre-cracked XPF800-UC (3.2 mm thickness).* ***NB The smallest and largest ligament is indicated in the graph only.*** *[27]*

CP800 (3.3 mm)

For the CP800 (3.3 mm thickness) material another successful application of the essential work of fracture methodology is achieved. Figure 4.44 shows the load-displacement curves along with the EWF results. From the load-displacement curves the strain hardening and stable crack growth can be identified (flattening of the curve and subsequent gradual decrease of load). A global engineering strain of up to 2% is measured at the point of complete failure. The linear regression line is fairly successfully found (R^2 = 0.92) and delivers an essential work of fracture of 511 kJ/m^2. The net sectional stresses are independent of the ligament length and fall within the previously set criteria for plane stress failure (see Figure A22 in Appendix A.3). No additional fracture surface analysis was performed here.

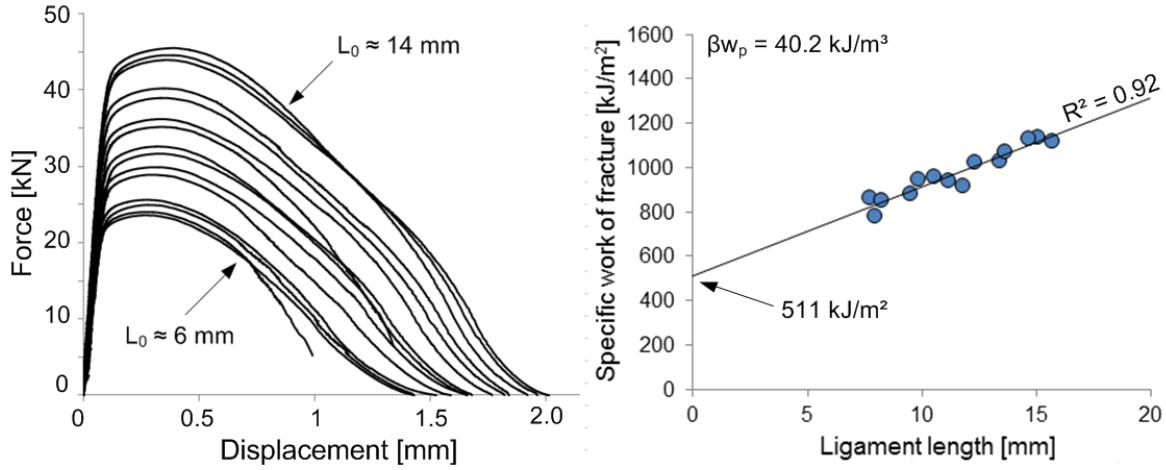

Figure 4.44: *EWF results of fatigue pre-cracked CP800-UC (3.3 mm thickness).* ***NB The smallest and largest ligament is indicated in the graph only.*** *[27]*

S550MC (3.0 mm)

For the reference HSLA (3.0 mm thickness) it was also possible to obtain a valid fracture toughness result. Figure 4.45 shows the load-displacement curves along with the EWF results. From the load-displacement curves the strain hardening and stable crack growth can be identified (flattening of the curve and subsequent gradual decrease of load). A global engineering strain of up to 3.5% is measured at the point of complete failure. The linear regression line is fairly successfully found (R^2 = 0.88) and delivers an essential work of fracture of 395 kJ/m^2. The net sectional stresses are independent of the ligament length and slightly above the previously set criteria for plane stress failure (see Figure A23 in Appendix A.3), probably due to a larger degree of local strain-hardening. No additional fracture surface analysis was performed here.

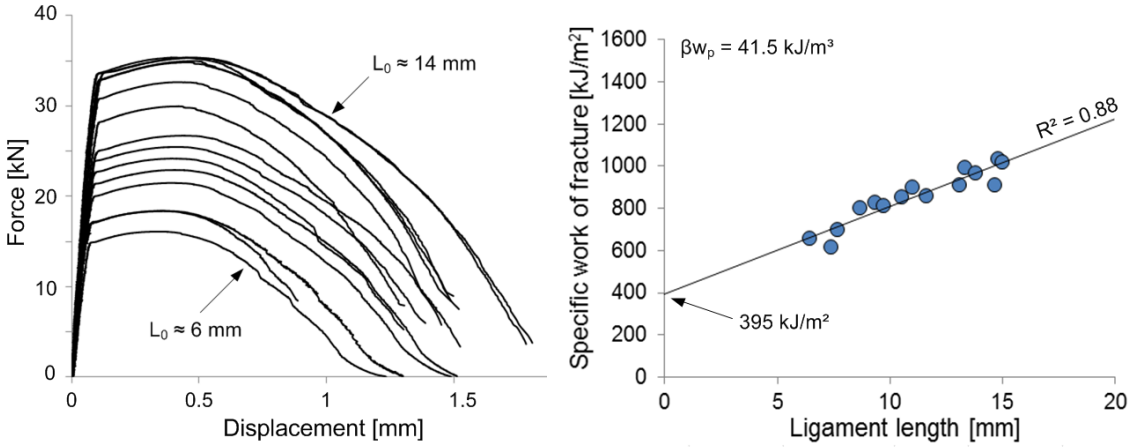

Figure 4.45: *EWF results of fatigue pre-cracked S550MC-UC (3.0 mm thickness).* ***NB The smallest and largest ligament is indicated in the graph only.*** *[27]*

In the next section, all EWF results obtained thus far are collected and summarized. After that, the main limitations are discussed with regard to the performed experiments. The EWF results are related to global formability parameters as well, which were obtained from regular tensile testing. A more detailed comparison with respect the initiation type in EWF testing is given as well for the XPF1000, XPF800, CP800 and S550MC materials at the end of the chapter.

Overview of results

Table 4.3: *Overview of EWF results for samples with a sheared notch (S.N.), fatigue pre-crack (F.C.) and EDM notch. Given values are valid at room temperature unless stated otherwise. All specimens were oriented in transverse direction relative to rolling (T-L).*

Material	Thickness	Initiation	w_e	βw_p	Failure mode	Remarks
XPF1000	1.8 mm	S.N.	n/a	n/a	Mixed	Core segregation
XPF1000	2.7 mm	S.N.	n/a	n/a	Brittle	Core segregation
" 60 °C	2.7 mm	S.N.	n/a	n/a	Mixed	Core segregation
" 100 °C	2.7 mm	S.N.	n/a	n/a	Mixed	Core segregation
" 120 °C	2.7 mm	S.N.	n/a	n/a	Mixed	Core segregation
XPF1000	2.7 mm	EDM	428 kJ/m^2	34.7 kJ/m^3	Ductile	Core segregation
XPF1000	2.9 mm	F.C.	n/a	n/a	Mixed	Core segregation
XPF1000	2.9 mm	S.N.	n/a	n/a	Brittle	Core segregation
XPF800	3.2 mm	F.C.	478±54 kJ/m^2	41.8 kJ/m^3	Ductile	n/a
XPF800	3.2 mm	S.N.	497±71 kJ/m^2	27.4 kJ/m^3	Ductile	n/a
DP1000	2.0 mm	S.N.	46±36 kJ/m^2	23.4 kJ/m^3	Ductile	n/a
CP800	3.3 mm	F.C.	511±41 kJ/m^2	40.2 kJ/m^3	Ductile	n/a
CP800	3.3 mm	S.N.	397±100 kJ/m^2	48.8 kJ/m^3	Ductile	n/a
CP800	4.0 mm	S.N.	347±34 kJ/m^2	45.6 kJ/m^3	Ductile	n/a
S550MC	3.0 mm	F.C.	395±49 kJ/m^2	41.5 kJ/m^3	Ductile	n/a
S550MC	3.0 mm	S.N.	650±65 kJ/m^2	48.8 kJ/m^3	Ductile	n/a

Limitations and assumptions

The tensile testing results at 60 °C and 100 °C suffer from an inaccuracy as was confirmed by the thermocouple readings. Especially the deviations at 100 °C are significant (+10 °C), therefore the actual properties might deviate. The temperature gradients inside the specimens during testing (60±2 °C and 100±5 °C) that were measured with the infrared camera are considered minimal and acceptable for a reliable measurement.

Regarding the fracture toughness testing with sheared notches, the most significant uncertainty lies in the ligament area determination. This is mostly due to the difficult interpretation of the ligament areas from the fractured surfaces, as the shearing deformation at the notches obscures the boundaries with the actual yielded ligament. The ligament area was correspondingly estimated from the fractured surfaces and an average value was calculated for every material. In Appendix B.1 the sensitivity of w_e with respect to the ligament length L_0 is estimated for the CP800 material (4.0 mm thickness). The specific work of fracture w_f is proportional to the ligament area, however an offset in the ligament lengths causes both a shift in w_f as well as the plastic dissipation factor βw_p. The linear regression line of the w_f values is then manipulated both in magnitude as well as slope. This causes a strongly non-linear dependence of the essential work of fracture w_e on the ligament lengths, as a shift in $L_0 \pm 1$ mm results in a change in w_e of $\pm$ 232 kJ/m^2 for this specific material. The change in βw_p is $\pm$ 6 kJ/m^3. These findings shows that inaccurate ligament length determination can drastically influence the obtained fracture toughness parameters and should receive proper attention.

From the high-speed camera recording the front- and back sides of the specimens during EWF testing were captured successfully with the chosen setup. However, the measuring frequency of 20,000 fps was subcritical for the rapid crack growth in the brittle XPF1000 materials. Complete failure was observed within 1 measuring frame (5×10^{-5} s). Therefore no useful information could be obtained with respect to the brittle crack growth for XPF1000. See figure 4.46.

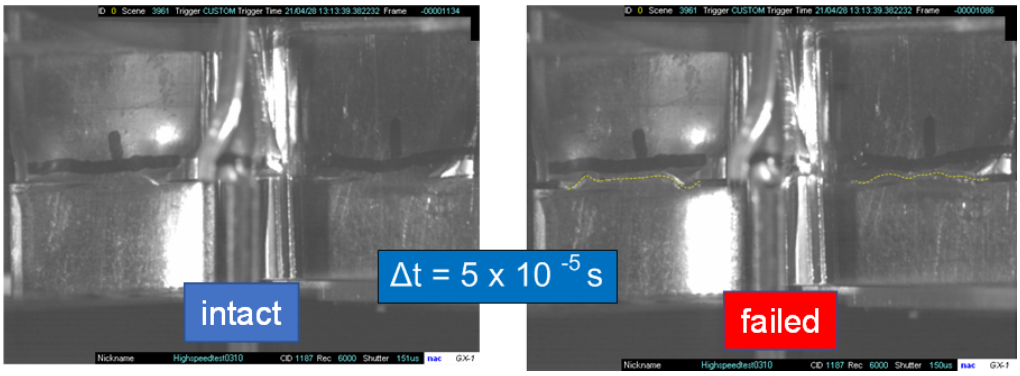

Figure 4.46: *High-speed camera results showing that the brittle fracture has occurred within one measuring frame (20,000 fps). The fracture path is traced in yellow for better visibility.*

Influence of initiation type

To further understand the differences between the fatigue pre-cracked samples and sheared samples, the load-displacement curves of samples with a similar ligament length ($\pm$ 1 mm accurate) are compared (where possible) as seen in Figure 4.47. Qualitatively there is a clear distinction between the two types of initiation; the fatigue pre-cracked samples transition from the linear-elastic domain to plasticity sharply, while the sheared samples display a more gradual transition. This difference could be explained by the previously mentioned brittle-like crack increment at the sheared notches that takes place before the peak load is reached. Due to this small decrease in ligament length before the peak load the measured force decreases, before ductile tearing actually takes place. The attained loads are similar as well as the total elongation. The CP800 grade appears to show a much higher ductility with sheared notches compared to sheared notches, however this single measurement is not representative for the whole batch of fatigue pre-cracked results (see Figure 4.44). Overall it can be confirmed that a similar mechanical response is evoked with both types of initiation for this specific ligament length. The linearity of the work of fracture with respect to the ligament length ($\beta w_p L_0$) differs more significantly, which could explain the difference in the obtained essential work of fracture w_e.

For the XPF1000 the effect of a blunt EDM notch is also investigated as seen in Figure 4.48. Here it can clearly be seen that the samples with a blunt notch require a much higher load to yield compared to the fatigue pre-cracked samples, due to the decreasing stress triaxiality with increasing notch radius and the additional plasticity and the notch tip. These two effects cause local strengthening of the material which enhances cracking resistance. This essentially translates to a higher *apparent* fracture toughness. This phenomenon is widely confirmed as well in similar research on the fracture toughness of AHSS [7][56][57]. Samples with a blunt EDM notch are therefore not suitable to represent the 'true' fracture toughness of a material, as it can widely over-estimate the cracking resistance.

The notch radius (or flaw size) introduced during the shearing of the notches is equivocal; from optical microscopy images only shearing deformation was observed without a distinct notch opening. This parameter is certainly non-trivial in fracture toughness testing, however from the obtained essential work of fracture it can be derived that the flaw size is likely supercritical and can fairly be used to approximate the 'true' fracture toughness.

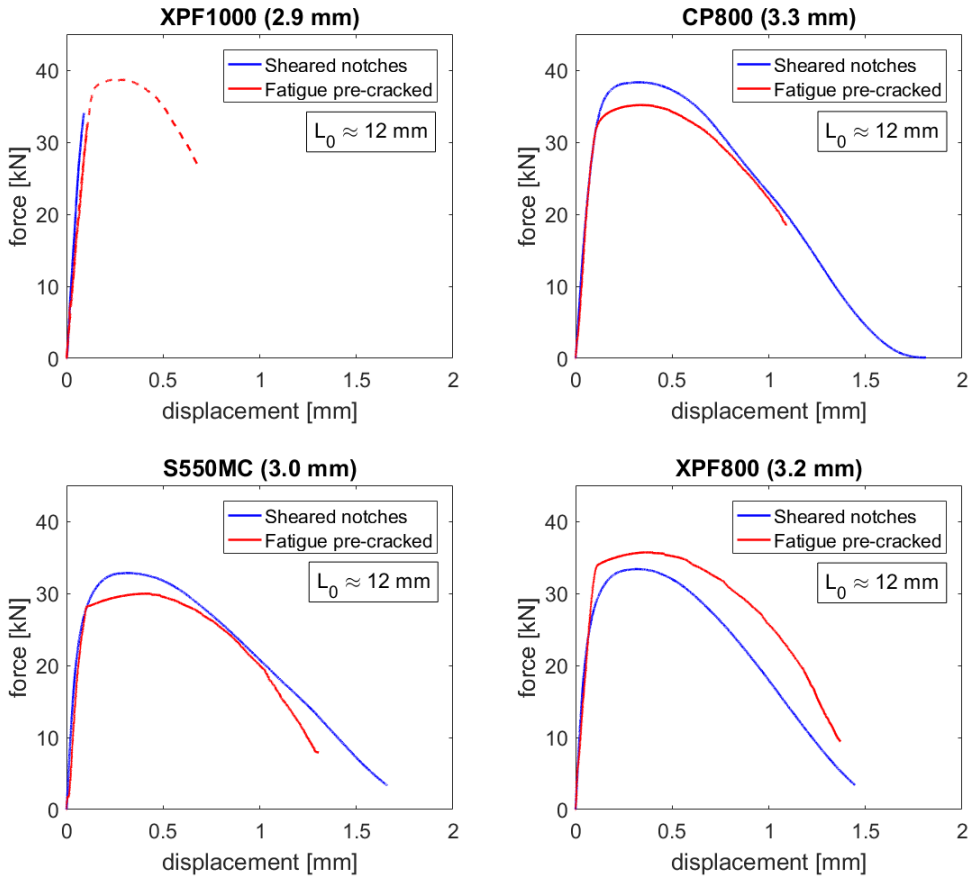

Figure 4.47: *Load-displacement curves of the four investigated steels comparing the fatigue pre-crack initiation and the sheared notch initiation. Ligament lengths are approximately 12 mm.*

Relation to global formability parameters

Toughness parameters obtained from (uniaxial) tensile testing are often used as a benchmark for forming operations, as explained in the previous chapter. The fracture toughness results from EWF testing are plotted against the toughness parameter $R_m \times \varepsilon_t$ in Figure 4.49. The graph shows that the essential work of fracture is independent of toughness obtained from tensile testing. This demonstrates and confirms the incapability of tensile testing to predict fracture toughness, which is sometimes be used to predict local formability in sheet metal forming. Designated fracture toughness testing is thus required to really predict (edge) cracking resistance.

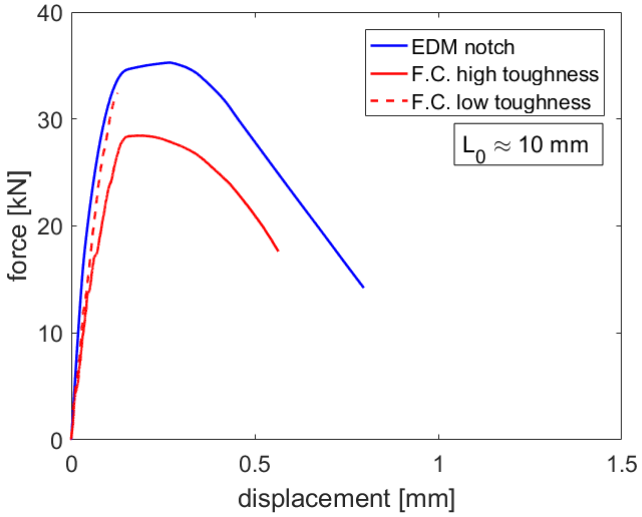

Figure 4.48: *Load-displacment curves of XPF1000-UC (2.7 & 2.9 mm thickness) comparing the EDM initiation and fatigue pre-crack (F.C.). The curves from the 2.7 mm material were scaled up linearly to match with the slightly thicker material.*

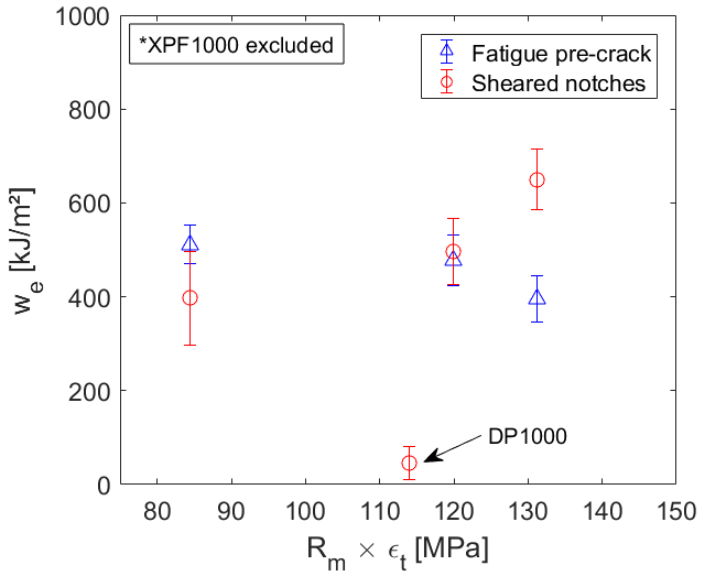

Figure 4.49: *Fracture toughness ($w_e \pm \sigma$) plotted against toughness ($R_m \times \varepsilon_t$) for the the investigated steels. Both sheared and fatigue pre-cracked results are included. NB The XPF1000 grade is excluded here, as no essential work of fracture could be obtained.*

4.4 Lab-scale deep-drawing

The experienced deformation modes in the fully deep-drawn cups were estimated with a blank that received a dotted grid pattern. From the dilation and distortion of the dots the total deformation was determined visually. In Figure 4.50 the findings are summarized at three different locations on the blank. Although the blank undergoes different types of deformation during the whole process (such as bending and unbending and the radii), it is nonetheless useful to locate weak points in the material or forming process. Cracking was observed exclusively inside the corners of the free edges, where

in-plane compression is the main deformation mode. This compression originates from negative hoop stresses as a result of blank-flow into the die. Inside the corners the stress concentrations are the highest. Accordingly, it is hypothesized that wrinkling at the blank edges increases the roughness (especially inside the four corners) and is responsible for the creation of notches in those edges (see Figure 4.51). Upon release of the cups from the tools, elastic springback occurs which triggers the growth of cracks. This phenomenon is observed with light optical microscopy, summarized in Figure 4.52 for the four materials. Close-up images are stored in Appendix A.4 for reference.

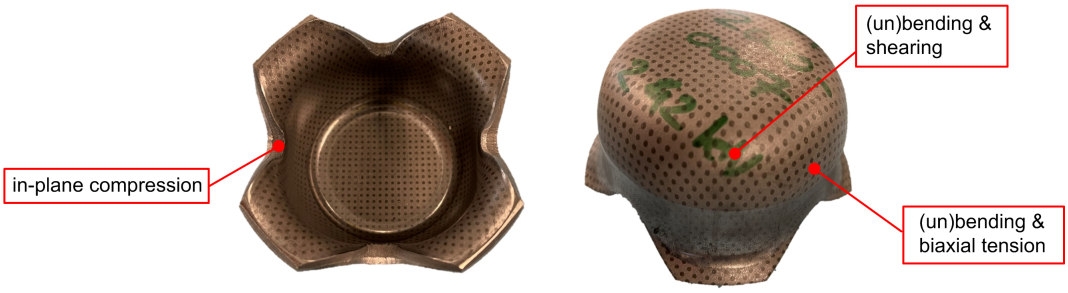

Figure 4.50: *Deep-drawn cup with dotted grid, to extract the deformation modes at the end of the forming process. The modes are indicated at different locations.*

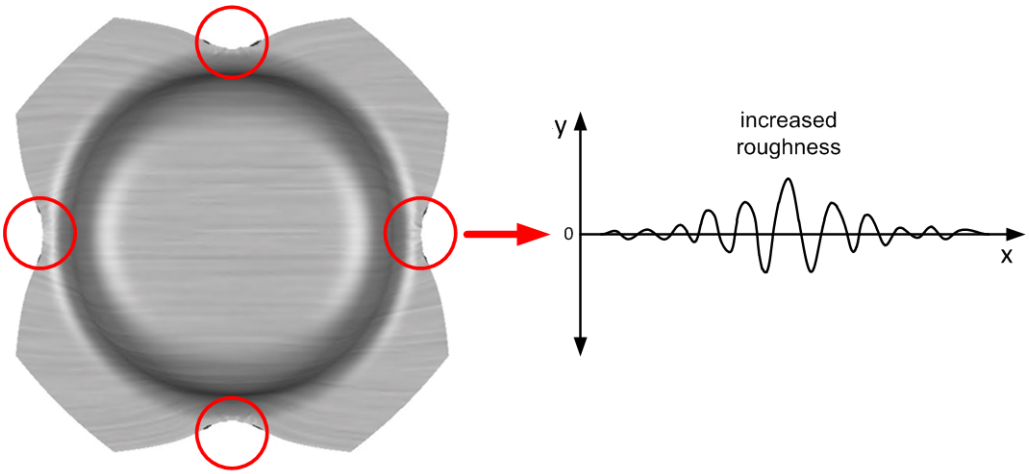

Figure 4.51: *In-plane compression at the free edges causing roughness, which can act as a fracture initiation point.*

The XPF1000 material showed the strongest susceptibility to edge cracking. Several through-thickness cracks were observed here, suggesting the intrinsically low fracture toughness i.e. low cracking resistance for these conditions. In the XPF800 similar wrinkling at the edges was found albeit with far less cracks. The S550MC cups on the other hand showed very limited wrinkling and a relatively smooth surface area. Where wrinkles *did* form, due to uneven blankholder pressure and/or blank flow, cracks were found (corner 4). In the CP800 material evenly wrinkled corners were found, with no cracks. This suggests a high fracture toughness for this material. The results are summarized in Table 4.4 along with the measured fracture toughness values.

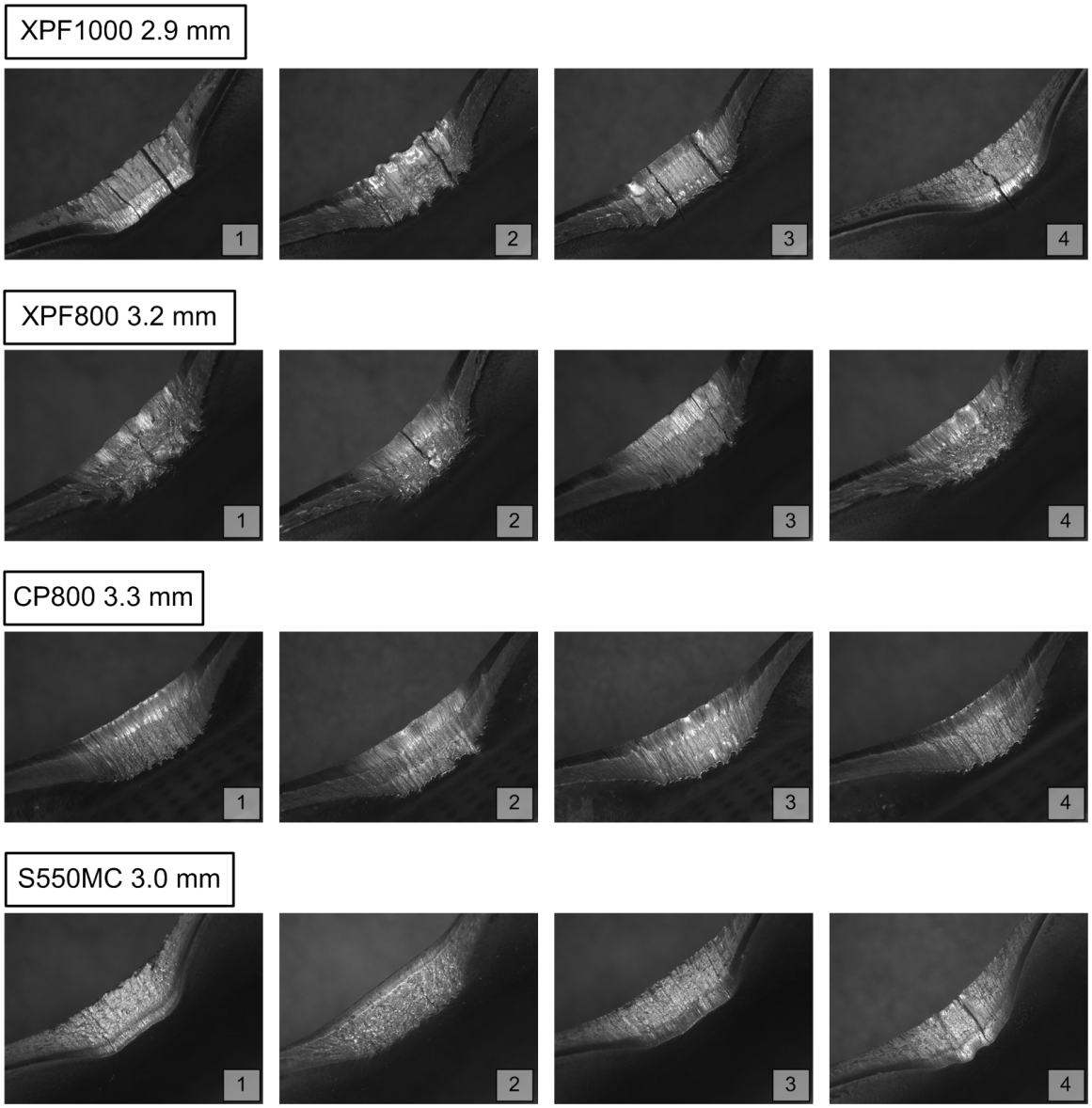

Figure 4.52: *LOM images of the inner compressed corners of the deep-drawn cups for the four materials.*

Table 4.4: *Results from deep-drawing and fracture toughness experiments (fatigue pre-cracked and sheared notches) with ranking positions based on the number of cracks and w_e values.*

Material	N$^{o.}$ cracks*	w_e (F.C.)	w_e (S.N.)	Pos. cracks	Pos. w_e (F.C.)	Pos. w_e (S.N.)
XPF1000	7	n/a	n/a	4	4	4
XPF800	1	478 kJ/m^2	497 kJ/m^2	2	2	2
CP800	0	511 kJ/m^2	397 kJ/m^2	1	1	3
S550MC	1	395 kJ/m^2	650 kJ/m^2	2	3	1

(*Through-thickness cracks)

To estimate the crack propagation resistance even further, the cups are deformed in a hydraulic press using a conical punch which is displaced 10 mm into the cups. During this test, the cracks in the compressed edges (or only the 'notches') experience a loading in mode I (opening mode) due to the circumferential stress introduced by the punch. The force in the load cell is recorded as well as the punch displacement. Figure 4.53 shows the opening of the cups schematically. In Figure 4.54 and Table 4.5 the results are collected for the four materials. Only the CP800 and S550MC cups were tested twice due to limited material availability.

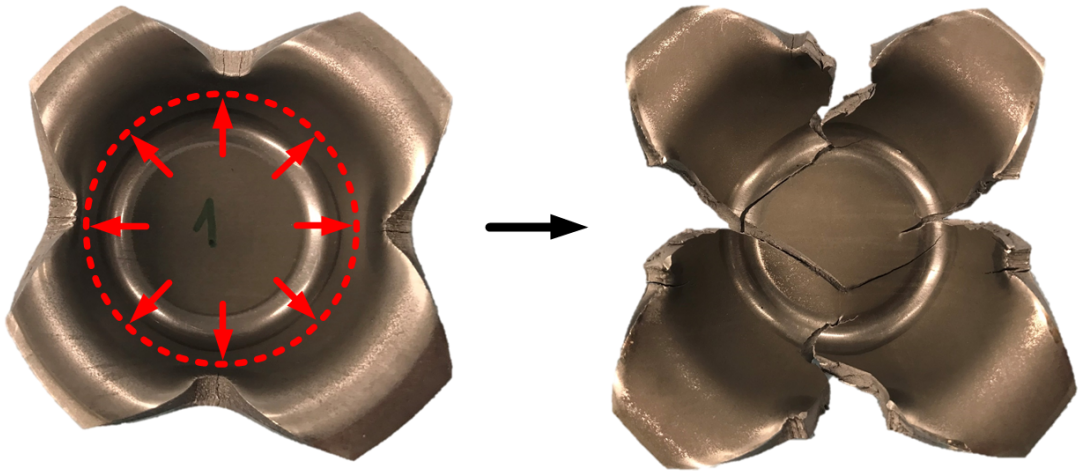

Figure 4.53: *Schematic image showing the further opening of the cups with the conical punch.*

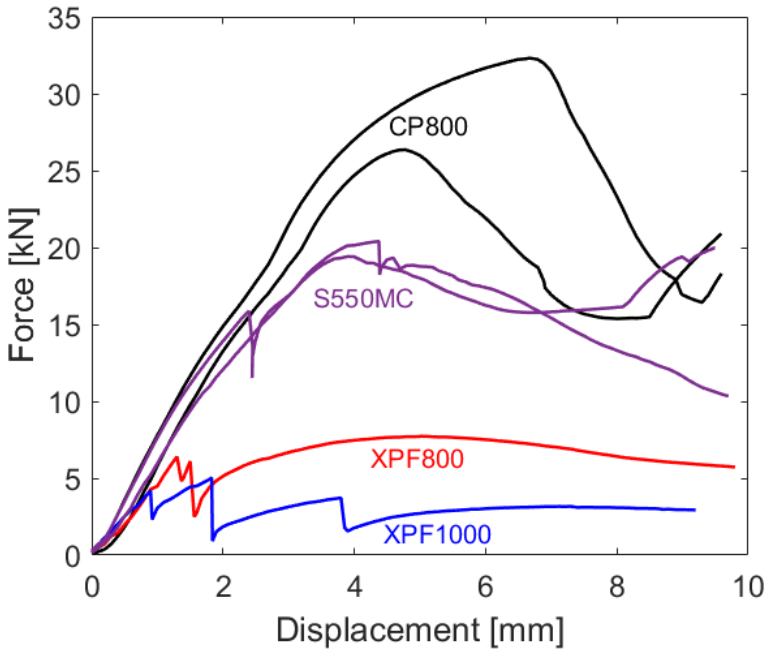

Figure 4.54: *Force-displacement curves recorded during opening of the deep-drawn cups for the four materials.* ***NB The CP800 and S550MC cups measurements were performed twice.***

Table 4.5: *Total work and peak force measured during opening of the cups.* ***NB The averaged values are given.***

Material:	Peak force:	Total work:
XPF1000	5.0 kN	26.8 J
XPF800	7.7 kN	60.3 J
CP800	29.4 kN	184.7 J
S550MC	20.2 kN	138.7 J

It can be seen that the results from that the fracture toughness results i.e. w_e values correlate with the observed cracking during deep-drawing. Only (observable) through-thickness cracks in the cups are registered here however. Both initiation methods are suitable to highlight the weak fracture toughness related to the low cracking resistance in XPF1000. However, the method with sheared notches seems to over-estimate the fracture toughness of S550MC, as the CP800 showed less cracks even though the w_e is lower (397 kJ/m^2 instead of 650 kJ/m^2). The method of fatigue pre-cracked samples was however able to predict the high fracture toughness accurately, which translated into a non-cracked cup after deep-drawing.

The resistance to subsequent crack propagation (Figure 4.54) correlates with the initial cracking behaviour and the fracture toughness results. The XPF1000 cup opens in a brittle fashion and at a relatively low punch force. Furthermore, the force-displacement curve shows sudden load drops indicating unstable crack growth increments. The XPF800 already shows a higher resilience than the XPF1000, displaying both a higher peak force (7.7 kN vs. 5.0 kN) as well as higher work (60.3 J vs. of 26.8 J). The S550MC has less cracks and shorter cracks than the XPF grades, reaching a much higher force than the latter. This is accurately predicted by the essential work of fracture, albeit that the fatigue pre-cracked w_e value over-estimates the propagation resistance of XPF800. This difference could be attributed by the different initially cracked geometry. The CP800 on the other hand has no initial cracks, but shows stable crack growth behaviour after a sufficiently increased load. The corresponding load-displacement curve shows ductile characteristics, with a much higher peak force and work than the HSLA (29.4 kN vs. 20.2 kN and 184.7 J vs. 138.7 J, respectively). The fatigue pre-cracked w_e value accurately predicts the relatively high fracture toughness for CP800, yet it is under-estimated by the sheared-notch w_e value.

The materials are of slightly different thicknesses, however this effect is considered negligible for these specific demonstration purposes. Although the validation is mostly qualitative and dependent on the initially deformed and cracked geometry, it can be said that fracture toughness measurements do provide valuable insights in predicting cracking behaviour during deep-drawing which cannot be predicted with regular tensile testing. The undeniably low fracture toughness of XPF1000 is correctly revealed with both initiation types used in EWF testing, showing a clear link with the local formability in deep-drawing. Accordingly, the EWF test with sheared notches could be used as a rapid fracture toughness test to reveal deterioration of such properties early in the development stages. Deviations from a threshold value can be used to indicate poor local formability during deep-drawing operations. For a more quantitative comparison, fatigue pre-cracking seems to be more suitable method to be able to rank materials in to a higher accuracy. Although there is evidence from literature reporting that a negative relation exists with the amount of pre-deformation and fracture toughness due to decreased ductility[58], a clear link with the initial flaw size, accumulated plastic deformation and fracture toughness needs further exploration.

5. Conclusions

Fracture toughness testing based on the essential work of fracture methodology was applied to different grades of AHSS produced by Tata Steel IJmuiden (a single phase with nano-precipitates, dual phase and complex phase) as well as an HSLA, to estimate the suitability for characterizing vastly different microstructures. The novel shearing method was applied here and compared with the established method of fatigue pre-cracked samples, to estimate its accuracy and robustness. The results were validated against the cracking behaviour observed in (laboratory-scale) deep-drawn cups.

It was found that the shearing device was able to create DENT samples of intermediate thickness (up to 4.0 mm) with varying ligament lengths rapidly and efficiently. The sample preparation time is drastically reduced compared to fatigue pre-cracking (several minutes instead of hours), also requiring less involvement of trained technicians. While the method of fatigue pre-cracking creates a clearly defined crack-initiation, the shearing tool introduces an artifact ahead of the notches presumably due to the bending deformation. This led to a brittle crack growth increment in this area which obscures the determination of the initial ligament area. Consequently, the EWF calculations can suffer from an inaccuracy as the ligament area is a highly sensitive parameter. It must be emphasized here that fatigue pre-cracking could also result in asymmetrical and unevenly grown cracks, due to machine misalignment for example.

The three initiation types (EDM notch, EDM notch with a fatigue pre-crack, and sheared notch) were evaluated and compared, to estimate their influence on the fracture toughness properties. The blunt EDM notch resulted in a fully ductile fracture accompanied by large amounts of plasticity for the XPF1000 material. This can be ascribed by the low stress triaxiality and additional plasticity at the notch tip. A fatigue crack initiation showed a completely different response; evoking ambivalent behaviour with either ductile or brittle fracture. This was derived from the global load-displacement curves (large difference in ductility) as well as SEM fracture surface investigations. The latter showed mixed-mode behaviour in both cases, but the ratio of failure via microvoid coalescence vs. transgranular cleavage fracture revealed the global fracture toughness properties. The calculated work of fracture data suffered from large scatter due to this effect, obstructing a successful linear fit to obtain an *essential* work of fracture value. Increasing the temperature to 60 or even 120 ^{o}C drastically increases the work of fracture through increased ductility until fracture. This effect can be explained by added thermal activation of otherwise inert slip-systems inside the BCC lattice that facilitate dislocation glide, and contribute to the creation of a plastic zone. The responsible micro-mechanisms changed accordingly; the relative amount of microvoid coalescence increased noticeably. Evidence of a ductile-to-brittle transitions was found as well. Delamination at the center-line, most likely due to core segregation, was observed as well, although no clear link with the fracture toughness properties was established. The samples with sheared notches displayed a similar mechanical response as the fatigue pre-cracked samples, which was evaluated for similar ligament lengths. Surprisingly, the XPF1000 material behaved even more brittle when the sheared notches were introduced instead of the fatigue pre-crack.

For the remaining materials (DP1000, XPF800, CP800 and S550MC) the EWF was successfully applied to find an essential work of fracture with both sheared notches and fatigue pre-crack initiations. The materials all displayed stable, ductile fracture interpreted from the global force-

displacement curves. For the DP1000 material this was confirmed by SEM fracture surface analysis, revealed by a predominantly dimpled fracture surface indicative of failure via microvoid coalescence. The highest essential work of fracture (with fatigue pre-cracked samples) was found with the CP800 material, followed by the XPF800, S550MC and XPF1000. For the sheared notches the ranking changed to S550MC, XPF800, CP800 and XPF1000. Overall, it can be said that the EWF methodology (with both types of initation) exposes the micro-mechanisms governing the fracture toughness properties. A chemical analysis of the fracture surface can provide more information on the responsible compounds that assist the relevant micro-mechanisms of failure.

The predictive capabilities of the EWF results were investigated by comparing the susceptibility to cracking during deep-drawing of cups. The cups were checked for cracking at the inner corners, as these compressed edges suffered from wrinkling that presumably creates small notch-like initiations that experience subsequent crack growth during deformation reversal i.e. elastic springback. The EWF results were in good agreement with the observed cracking, as well as the extended crack propagation resistance when the cups were opened with a conical punch. The fatigue pre-cracked results seem to provide a higher predictive accuracy, however both initiation types were able to reveal the intrinsically low fracture toughness of XPF1000. The intitial flaw size in these corners and accumulated plastic pre-deformation is certainly non-trivial to the fracture toughness properties and needs further study. However, it can be concluded that there is a correlation between the observed edge ductility and essential work of fracture, which could not be explained with global formability parameters obtained from conventional tensile testing.

Alternatively, the EWF method with sheared notches could be implemented as a routine test to identify deterioration of fracture toughness properties early in the development stages. These findings can be used to predict poor local formability in deep-drawing without extensive experimental efforts, as the sample preparation time is shortened drastically. In the next chapter, several recommendations are provided to further improve the experimental methods and fundamental understanding of material behaviour.

6. Recommendations

Refining of experimental methods

To successfully implement the fracture toughness test in robust routine testing, several points of action are brought forwards:

- Confirm that the correct temperatures are measured with the infrared camera, and account for the measuring offset to improve reliability of the EWF measurements at elevated temperatures. The infrared camera should be re-calibrated accordingly.
- Repeat EWF measurements for a broader range of ligament lengths to obtain more datapoints for a better linear fit. Some fits had a comparatively high variance (R^2 = 0.75) which can lead to a high error in the determined w_e value. Also, it is advised to do at least three repeated measurements per ligament length.
- As an addition to the recommendations above, the ligament range of $\pm$ 6-10 mm would be useful to be able to compare with the fatigue pre-cracked experiments. From the net sectional stresses in the fractured ligaments it would also reveal whether a plane strain to plane stress transition takes place.
- Try to characterize the notch of the sheared samples in more detail to extract a notch radius if possible. In addition, the influence of the shearing deformation needs further study to understand the effect on the fracture behaviour.
- Improve efforts to determine the fractured ligament area more accurately, to improve accuracy in both the w_f data as well as w_e. This could be done numerically with optical microscopy for example. It would slightly increase the data processing time however.
- Investigate and attempt to quantify the initial damage introduced in the sheared edges of the deep-drawing blanks. The different microstructures are most likely to experience work-hardening embrittlement to a varying degree, altering the observed cracking behaviour after forming.
- For EWF testing of new materials it is advised to check the fractured surface and verify that ductile fractured took place. If a mixed-mode is found, it should be checked whether a ductile-to-brittle transition takes place.
- Investigate the fractured surfaces in the cracked cups to verify the micro-mechanisms and distinguish whether the fracture was predominantly ductile or brittle.
- Implement a more quantitative comparison with the deep-drawn cups, that can account for both the different amounts of plastic deformation at the wrinkled edges and incorporate the flaw/notch-size created at the edges.

Gaining understanding of material behaviour

To better understand the fracture mechanics that take place at micro-scale, several recommendations are given:

- Identify cleavage triggering particles from the fractured surfaces of XPF1000, using energy dispersive x-ray (EDX) analysis for example. This can lead to insights on the unwanted compounds that cause brittle behaviour, in order to try to reduce these in production.
- Further examine the fractured surfaces with (micro-)hardness measurements, to estimate whether the obtained hardness profile can be related to center-line delamination for example. It could provide an alternative view of the local hardening behaviour during EWF testing.
- Identify the relevant void nucleation sites, especially the larger inclusion particles as these lead to larger voids as well. Again, this knowledge could be used to limit the formation of these particles during production.
- Further study the ductile-to-brittle transition of XPF1000, by performing additional EWF measurements at both lower and higher temperatures (e.g. -20 and 150 ^{o}C) to capture the lower- and higher shelf fracture toughness. The EWF measurements should be compared with existing Charpy impact tests to estimate the relation between the DBTT, flaw size, and strain rate. An additional experiment here could be with fatigue pre-cracked Charpy V-notch specimens to obtain an *impact fracture toughness* result.
- Study the relation between the different available (fracture) toughness testing methodologies: hole-expansion testing, Charpy impact testing & EWF testing. Understanding the intrinsic material processes involved is essential to predict defects during sheet metal forming.

Predicting with numerical models

Numerical modeling can complement the experimental results and replace some testing when used efficiently. A few suggestions are provided here with regard to numerical model construction:

- The EWF experiments could be simulated (in MSC Marc Mentat for example) using solid-shell elements (or brick 3D elements). The sample geometries of the three types of initiation should be replicated (EDM notch, EDM notch + fatigue pre-cracks, and sheared notch) and compared with the experimental results. The tearing at the notches/cracks could be approximated with cohesive zone modeling and/or higher-order damage models for example. Depending on the chosen approach, it is critical to impose an appropriate 'moving crack-tip mesh' to maintain accuracy. The highly anisotropic nature of cracks should also be considered when using certain damage models, thereby favoring methods that anisotropically alter the stiffness- and compliance matrices. [59][60][61]
- It is highly important to load the correct material properties into the model that incorporate both temperature effects and anisotropy. The element type may also influence the convergence of the model, and should be chosen carefully.
- The deep-drawing experiments can be compared with sheet metal forming simulations, to compare the tendency of wrinkling near the edges and subsequent cracking. Again, when using a damage model the contribution of the initial damage near the sheared edges should be accounted for. Moreover, an advanced failure model that incorporates a wide range of load parameters is advised.[62]

Bibliography

[1] ICCT (2014). *Improving the conversions between the various passenger vehicle fuel economy/CO2 emission standards around the world.* URL: https://theicct.org/blogs/staff/improving-conversions-between-passenger-vehicle-efficiency-standards. Retrieved October 1st, 2020.

[2] Rhodium Group (2018). *Final US Emissions Numbers for 2017.* URL: https://rhg.com/research/final-us-emissions-numbers-for-2017/. Retrieved October 1st, 2020.

[3] NHTSA (2020). *Newer cars are safer*. URL: https://www.nhtsa.gov/newer-cars-are-safer-cars. Retrieved October 1st, 2020.

[4] World Auto Steel (2018). *Advanced High-Strength Steel (AHSS) Definitions*. URL: https://www.worldautosteel.org/steel-basics/automotive-advanced-high-strength-steel-ahss-definitions/. Retrieved October 2nd, 2020.

[5] Casellas, D., Frómeta, D., Lara, A. et al. (2019). *New testing device to evaluate edge cracking resistance and crashworthiness of thin metallic sheets.* In: 28th International Forum for Material Testing, Ulm.

[6] Janssen, M., Zuidema, J. & Wanhill, R.J.H. (2006). Fracture Mechanics (2nd edition). VSSD, Delft. ISBN 9040722218.

[7] Frómeta, D., Lara, A., Parareda, S. et al. (2020). *Identification of fracture toughness parameters to understand the fracture resistance of advanced high strength steels.* Engineering Fracture Mechanics, 229, pp. 106949.

[8] Muñoz, R., Lara, A. & Casellas, D. (2011). *Fracture toughness characterization of advanced high strength steels.* In: International deep drawing research group (IDDRG) conference, Bilbao, Spain.

[9] Casellas, D., Lara, A., Frómeta, D. et al. (2017). *Fracture Toughness to Understand Stretch-Flangeability and Edge Cracking Resistance in AHSS.* Metallurgical and Materials Transaction A, 48, pp. 8694.

[10] Jonsén, P., Frómeta, D., Golling, S. et al. (2017). *Fracture mechanics based modelling of failure in advanced high strength steels.* In: 6th International Conference Hot Steel Metal Forming of High-Performance Steel CHS2 2017, pp. 15-23.

[11] Sunil Kumar, M.R., Schmidova, E., Konopík, P. et al. (2020). *Fracture Toughness Analysis of Automotive-Grade Dual-Phase Steel Using Essential Work of Fracture (EWF) Method*. Metals, 10 (8), pp. 1 - 12.

[12] National Material Company (2020). *AHSS Leads the Automotive Industry in 2020*. URL: http://www.nationalmaterial.com/ahss-leads-the-automotive-industry-in-2020/. Retrieved October 5th, 2020.

[13] Hilditch, T.B., de Souza, T. & Hodgson, P.D. (2015). *2 - Properties and automotive applications of advanced high-strength steels (AHSS)*. In: Welding and Joining of Advanced High Strength Steels (AHSS). Woodhead Publishing, Australia. ISBN 9780857094360.

[14] Lingbeek, R.A. (2008). *Virtual Tool Reworking: New Strategies in Die Design using Finite Element Forming Simulations (PhD thesis)*. Enschede: University of Twente.

[15] Dykeman, J., Hoydick, D., Link, T. et al. (2009). *Material property and formability characterization of various types of high strength dual phase steel.* SAE Technical Paper, 2009-01-0794.

[16] Baluch, N., Udin, Z.M. & Abdullah, C.S. (2014). *Advanced High Strength Steel in Auto Industry: an Overview*. Engineering, Technology & Applied Science Research, 4(4), pp. 686-689.

[17] AISI (1998). UltraLight steel auto body - Final Report. American Iron and Steel Institute.

[18] Díaz, J. & Costas, M. (2019). *Crashworthiness*. In: Altenbach H., Öchsner A. (eds) Encyclopedia of Continuum Mechanics. Springer, Berlin, Heidelberg.

[19] IIHS (2020). Vehicle Ratings: 2020 Dodge Durango. URL: https://www.iihs.org/ratings/vehicle/dodge/durango-4-door-suv/2020. Retrieved October 6^{th}, 2020.

[20] World Auto Steel (2018). *Blanking, Shearing and Trim Operations*. URL: https://www.ahssinsights.org/news/blanking-shearing-and-trim-operations/. Retrieved October 9^{th}, 2020.

[21] Shih, H.C., Chirac, C. & Shi, M. (2010). *The Effects of AHSS Shear Edge Conditions on Edge Fracture*. Proceedings of the 2010 International Conference on Manufacturing Science and Engineering, MSEC2010-34062.

[22] Afshin, E. & Kadkhodayan, M. (2015). *An experimental investigation into the warm deep-drawing process on laminated sheets under various grain sizes.* Materials and Design, 87, pp. 25 - 35.

[23] Frómeta, D., Tedesco, M., Calvo, J. et al. (2017). *Assessing edge cracking resistance in AHSS automotive parts by the Essential Work of Fracture methodology.* Journal of Physics: Conference Series, 896.

[24] Rijkenberg, A., Bellina, P., Jones, P. et al. (2017). *Stretching Strength and Formability for Increased Performance and Mass Savings in Automotive Chassis Applications*. Steels in Cars & Trucks 2017 Conference.

[25] Smallman, R.E. & Ngan, A.H.W. (2007). Physical Metallurgy and Advanced Materials (7^{th} edition). Butterworth-Heinemann, Oxford. ISBN 9780750669061.

[26] Tata Steel (2020). *Advanced and Ultra High-strength Steel (AHSS / UHSS)*. URL: https://www.tatasteeleurope.com/ts/automotive/products/hot-rolled/advanced-and-ultra-high-strength-steel. Retrieved October 30^{th}, 2020.

[27] Cutting Edge 4.0 Period Technical Report - Part B. *Facing edge-cracking in AHSS: towards zero-defect manufacturing through novel material characterization and data driven analytics for process monitoring.*

[28] Kang, Y., Han, Q., Zhao, X., et al. (2013). *Influence of nanoparticle reinforcements on the strengthening mechanisms of an ultrafine-grained dual phase steel containing titanium*. Materials and Design, 44, pp. 331-339.

[29] Bardelcik, A., Worswick, M.J. & Wells, M.A. (2014). *The influence of martensite, bainite and ferrite on the as-quenched constitutive response of simultaneously quenched and deformed boron steel-Experiments and model*. Materials Design, 55, pp. 509-525.

[30] Pathak, N., Butcher, C. & Worswick, M. (2016). *Assessment of the Critical Parameters Influencing the Edge Stretchability of Advanced High Strength Steel*. Journal of Materials Engineering and Performance, 25, pp. 4919-4932.

[31] Tata Steel (2014). Ympress S550MC (datasheet). Retrieved July 7^{th}, 2021.

[32] Anderson, T. (2005). Fracture Mechanics - Fundamentals and Applications (3^{rd} edition). CRC Press, Florida. ISBN 9781420048215.

[33] Dodds, R.H., Jr., Anderson, T.L. & Kirk, M.T. (1991). *A framework to correlate a/W ratio effects on elastic-plastic fracture toughness (J_c).* International Journal of Fracture, 48, pp. 1 - 22.

[34] Reiser, J. & Hartmaier, A. (2020). *Elucidating the dual role of grain boundaries as dislocation sources and obstacles and its impact on toughness and brittle-to-ductile transition*. Scientific Reports, 10, pp. 1 - 18.

[35] Bonnekoh, C., Jǎntsch, U., Hoffmann, J., et al. (2019). *The brittle-to-ductile transition in cold rolled tungsten (W) plates: Impact of crystallographic texture, grain size and dislocation density on the transition temperature.* International Journal of Refractory Metals and Hard Materials, 78, pp. 146 - 163.

[36] Pathak, N., Butcher, C., Worswick, M. J. et al. (2017). *Damage Evolution in Complex-Phase and Dual-Phase Steels during Edge Stretching.* Materials, 10(4), pp. 346.

[37] Argon, A.s., Im, J. & Safoglu, R. (1975). *Cavity formation from inclusions in ductile fracture*. Metallurgical Transactions, 6, pp. 825 - 837.

[38] Rice, J.R. & Tracey, D.M. (1969). *On the Ductile Enlargement of Voids in Triaxial Stress Fields.* Journal of the Mechanics and Physics of Solids, 17, pp. 201 - 217.

[39] Tvergaard, V. (1982). *On Localization in Ductile Materials Containing Spherical Voids,* International Journal of Fracture, 18, pp. 237 - 252.

[40] Anderson, T.T. & Williams, S. (1986). *Assessing the Dominant Mechanism for Size Effects in the Ductile- to-Brittle Transition Region.* ASTM STP 905, American Society for Testing and Materials, pp. 715 - 740.

[41] Anderson, T.L. & Stienstra, D. (1989). *A Model to Predict the Sources and Magnitude of Scatter in Toughness Data in the Transition Region.* Journal of Testing and Evaluation, 17, pp. 46 - 53.

[42] Evans, A.G. (1983). *Statistical Aspects of Cleavage Fracture in Steel.* Metallurgical Transactions, 14A, pp. 1349 - 1355.

[43] Fan, D., Kaushik, P. & Pielet, H. (2018). *Bend failure mechanism of zinc coated advanced high strength steel*. ISIJ International, 58(8), pp. 1538 - 1544.

[44] Luo, C. (2001). *Modeling the behavior of inclusions in plastic deformation of steels (PhD Thesis)*. Royal Institute of Technology, Sweden.

[45] Curran, D., Seaman, L. & Shockey, D. (1987). *Dynamic failure of solids*. Physics Report, 147, pp. 253 - 388.

[46] Pineau, A., Benzerga, A.A. & Pardoen, T. (2016). *Failure of metals I: Brittle and ductile fracture*. Acta Materialia, 107, pp. 424 - 483.

[47] GOM GmbH (2016). Aramis version 6.3.1 (software). Braunschweig, Germany.

[48] Broberg, K.B. (1975). *On stable crack growth*. Journal of the Mechanics and Physics of Solids, 23(3), pp. 215 - 237.

[49] Clutton, E. (2001). *Essential Work of Fracture*. European Structural Integrity Society (ESIS), 28, pp. 177 - 195.

[50] Frometa, D., Lara, A., Parareda et al. (2020). *New tool to evaluate the fracture resistance of thin high strength metal sheets*. IOP Conference Series: Materials Science and Engineering, 967, 012088.

[51] The Mathworks Inc. (2016). MATLAB version R2016b (software). Massachusetts, United States.

[52] Hill, R. (1952). *On Discontinuous Plastic States, with Special Reference to Localized Necking in Thin Sheets.* Journal of the Mechanics and Physics of Solids, 1, pp. 19 - 30.

[53] Chandra, S.K., Sarkar, R., Bhowmich, A.D., et al. (2018). *Fracture toughness evaluation of interstitial free steel sheet using Essential Work of Fracture (EWF) method*. Engineering Fracture Mechanics, 204, pp. 29 - 45.

[54] Queiroza, R.R.U., Cunhab, F.G.G. & Gonzalez, B.M. (2012). *Study of dynamic strain aging in dual phase steel.* Materials Science and Engineering A, 543, pp. 84 - 87.

[55] Delannay, L. (2019). *How plasticity induces texture in polycrystals (Lecture notes)*. Louvain-la-Neuve: École polytechnique de Louvain.

[56] Muñoz, R., Lara, A., Casellas, D. (2011). *Fracture toughness characterization of advanced high strength steels.* In: International deep drawing research group (IDDRG) conference. Bilbao, Spain.

[57] Gutiérrez, D., Ll, Pérez, Lara, A., Casellas, D., et al. (2012). *Toughness evaluation of high strength steels sheets by means of the essential work of fracture.* In: 19^{th} European conference on fracture: fracture mechanics for durability, reliability and safety, ECF 2012.

[58] El-Fadaly, M.S., El-Sarrage, T.A., Eleiche, W. et al. (1995). *Fracture toughness of 20Mn-MoNi55 steel at different temperatures as affected by room-temperature pre-deformation.* Journal of Materials Processing Technology 54, pp. 159 - 165.

[59] Schreurs, P.J.G. (2012). *Fracture Mechanics (Lecture notes)*. Eindhoven: Eindhoven University of Technology.

[60] Mediavilla, J. (2005). *Continuous and discontinuous modelling of ductile fracture (PhD Thesis).* Eindhoven: Eindhoven University of Technology.

[61] Kurz, W. (1993). *Debonding along a fiber/matrix interface in a composite.* WFW 93.109, pp. 34.

[62] Li, Y., Luo, M., Gerlach, J. et al. (2010). *Prediction of shear-induced fracture in sheet metal forming*. Journal of Materials Processing Technology, 210, pp. 1858 - 1869.

Appendix A

A.1 Notch characterization

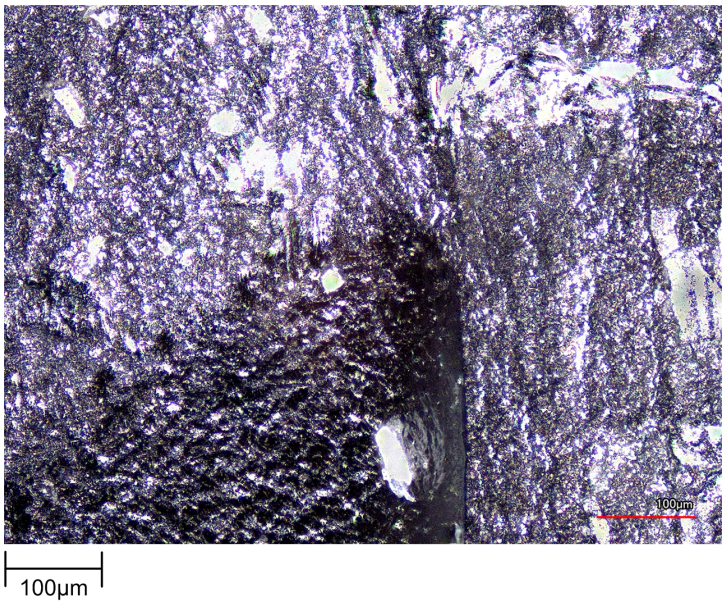

Figure A1: *3D laser confocal microscope image (20x magnification) showing the notch from the top side.*

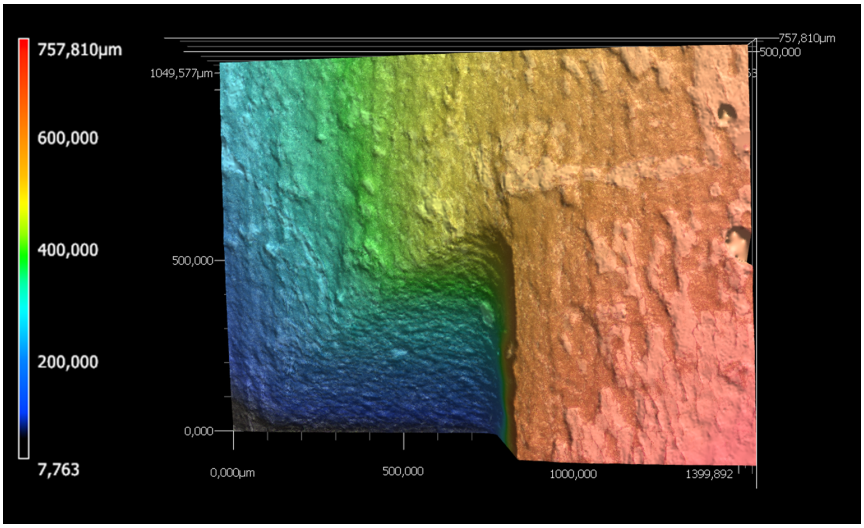

Figure A2: *3D laser confocal microscope image (10x magnification) showing the notch from the top side with height mapping.*

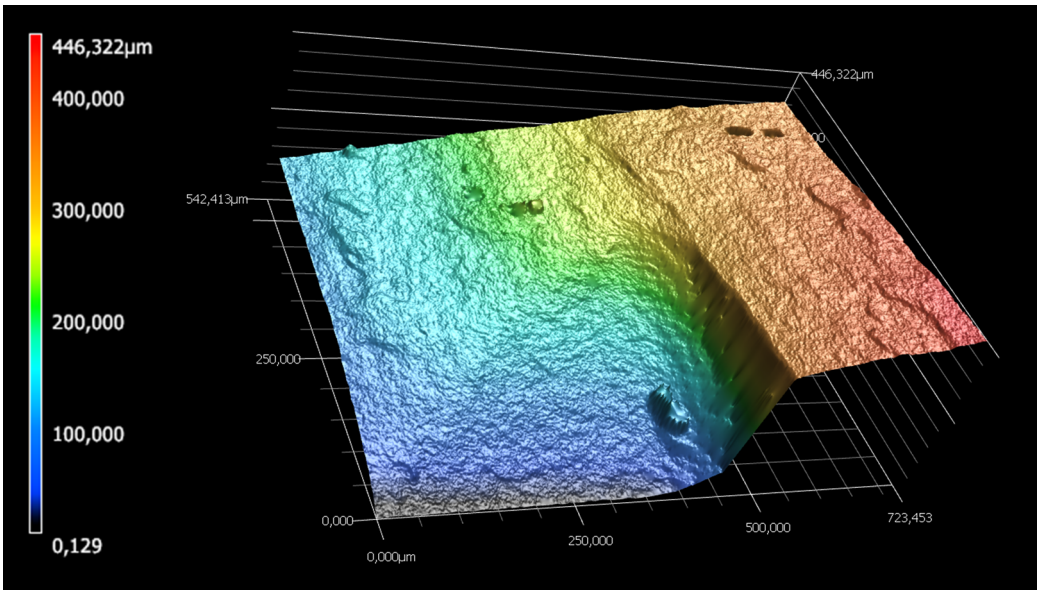

Figure A3: *3D laser confocal microscope image (10x magnification) showing the notch from the side with height mapping.*

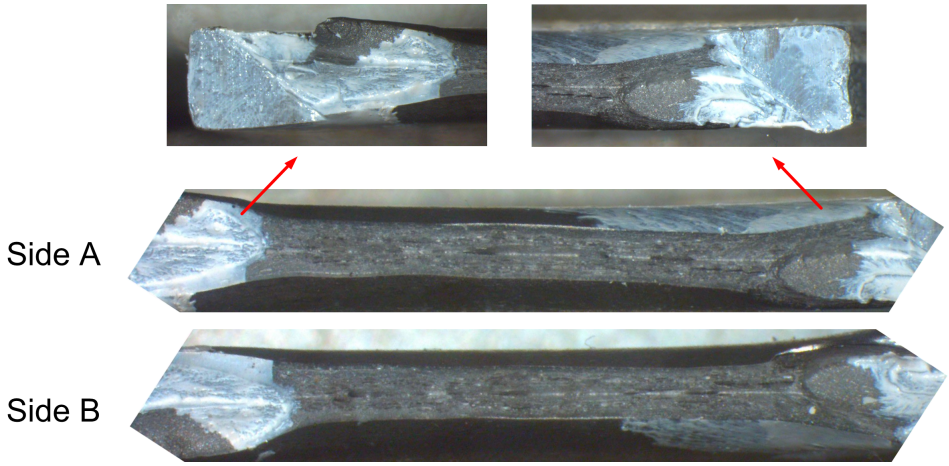

Figure A4: *White-ink infused into the sheared notch showing the extent of the brittle-like crack intiation during EWF testing, before the ligament has yielded.*

A.2 Additional results from tensile testing

before fracture:

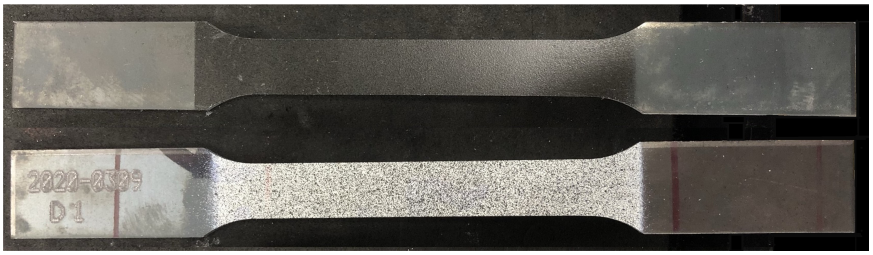

after fracture:

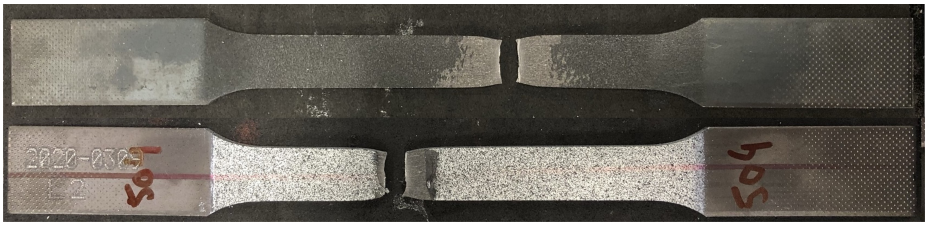

Figure A5: *Two different A50R specimens (front & back sides) before and after testing.*

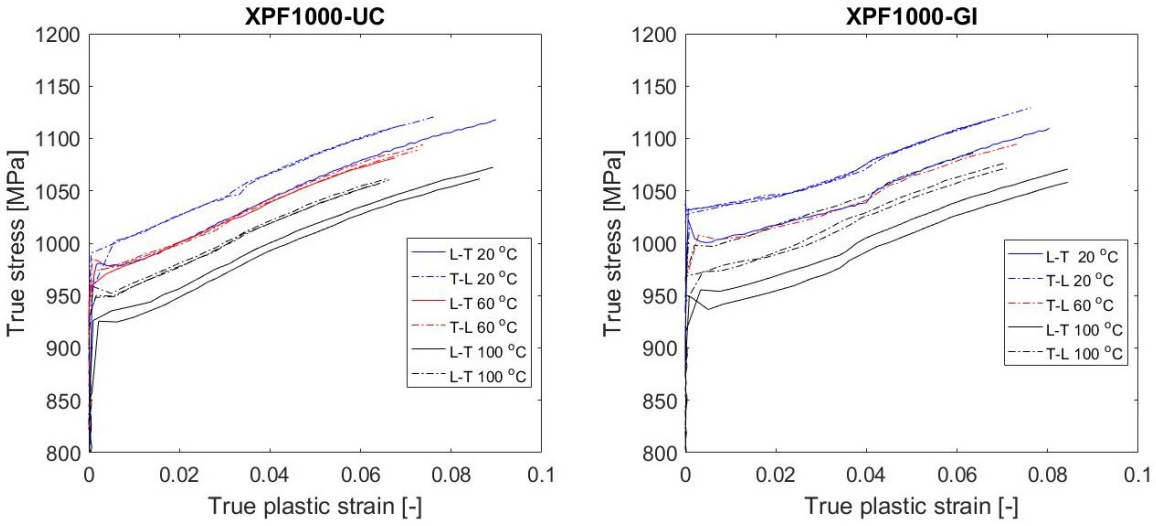

Figure A6: *True stress vs. true plastic strain curves for XPF1000-UC (#1) and XPF1000-GI (#2) at 20, 60 and 100 °C.*

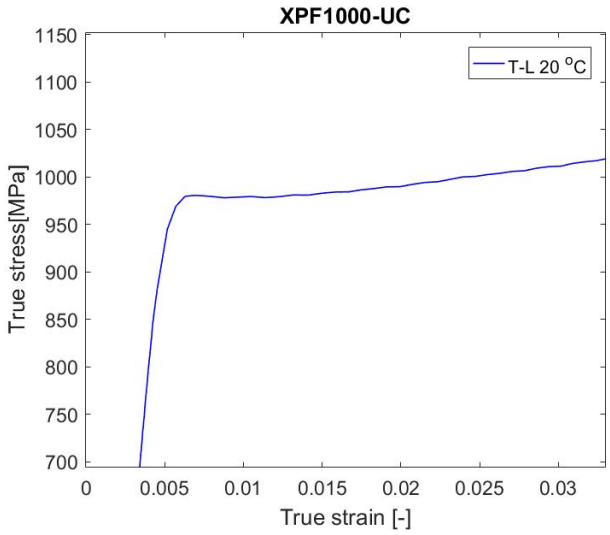

Figure A7: *Zoomed-in portion of true stress vs. true strain curve, showing the yield point phenomenon.*

A.3 Additional results from EWF testing

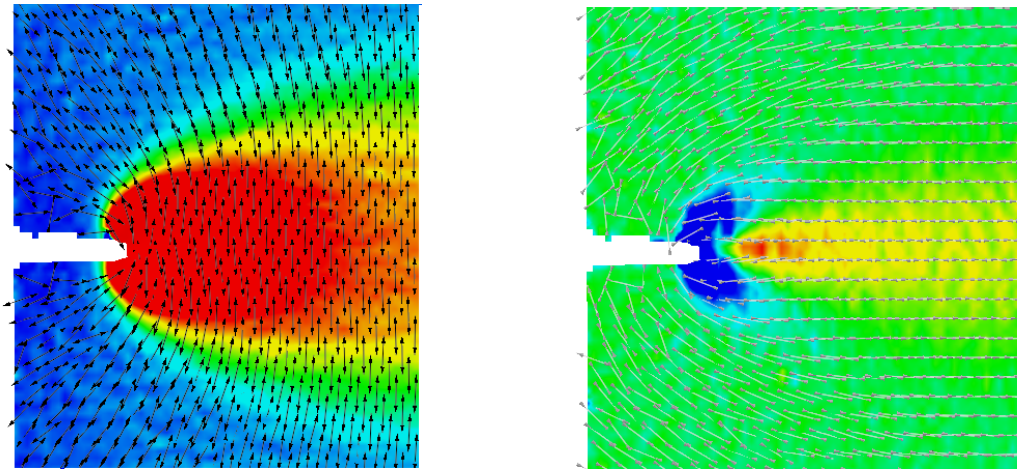

(a) Major strain directions (b) Minor strain directions

Figure A8: *Local strain directions for the T-L specimen with a 25 mm ligament length at peak load. The negative shear strain ε_{xy} is due to the definition of the X-Y coordinate system. NB different strain scales were used in the two images.*

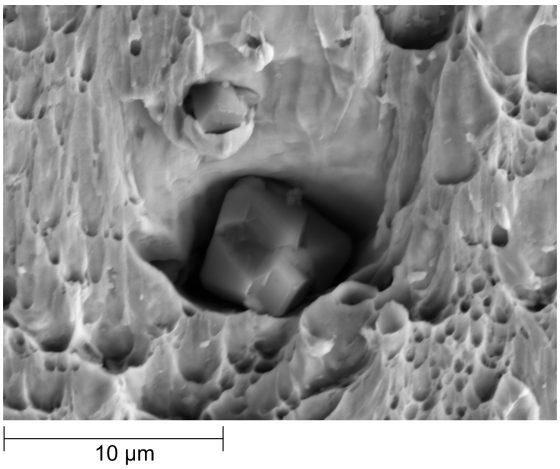

Figure A9: *SEM image of a non-metallic particle (approximate size 6.5 µm) that acted as a void nucleation site leading to failure by microvoid coalescence in XPF1000 (1.8 mm thickness).*

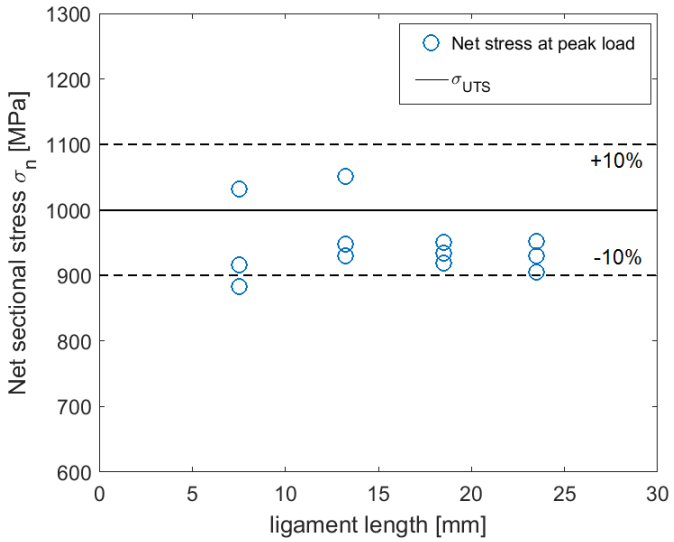

Figure A10: *Maximum net sectional stress as a function of ligament lengths experienced during EWF testing of DP1000 (2.0 mm thickness) with sheared notched. The stress criterion is included here with a ± 10% interval.*

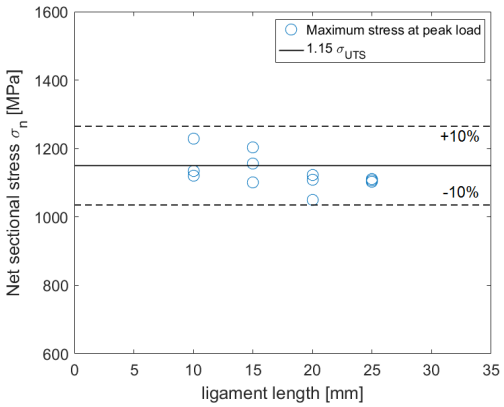

Figure A11: *Maximum net sectional stress as a function of the ligament length experienced during EWF testing of XPF1000 (1.8 mm thickness) with sheared notches. The stress criterion is included here with a ± 10% interval.*

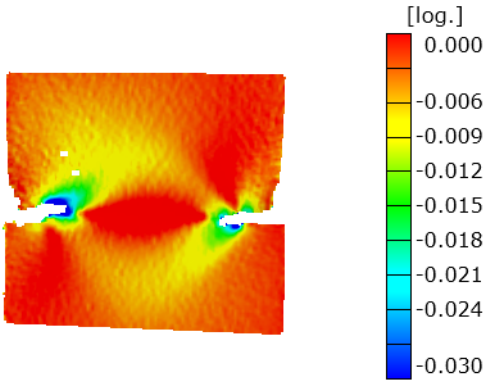

Figure A12: *Minor strain before final fracture of a high fracture toughness XPF1000-UC (1.8 mm thickness) sample (right);* $L_0 \approx 10$ *mm.*

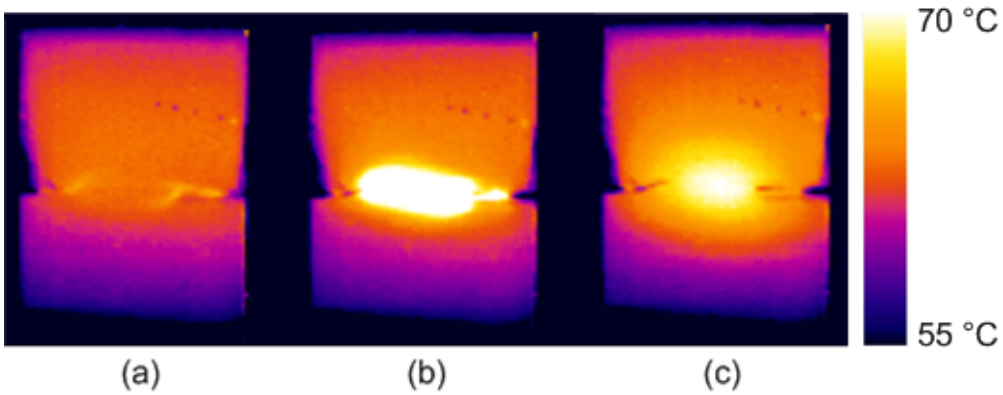

Figure A13: *Heat images (infrared field) during EWF testing of XPF1000 (2.7 mm thickness) at* 60^oC*, showing* ***(a)*** *brittle crack initiation* ***(b)*** *ligament yielding and* ***(c)*** *stable crack growth before fracture.*

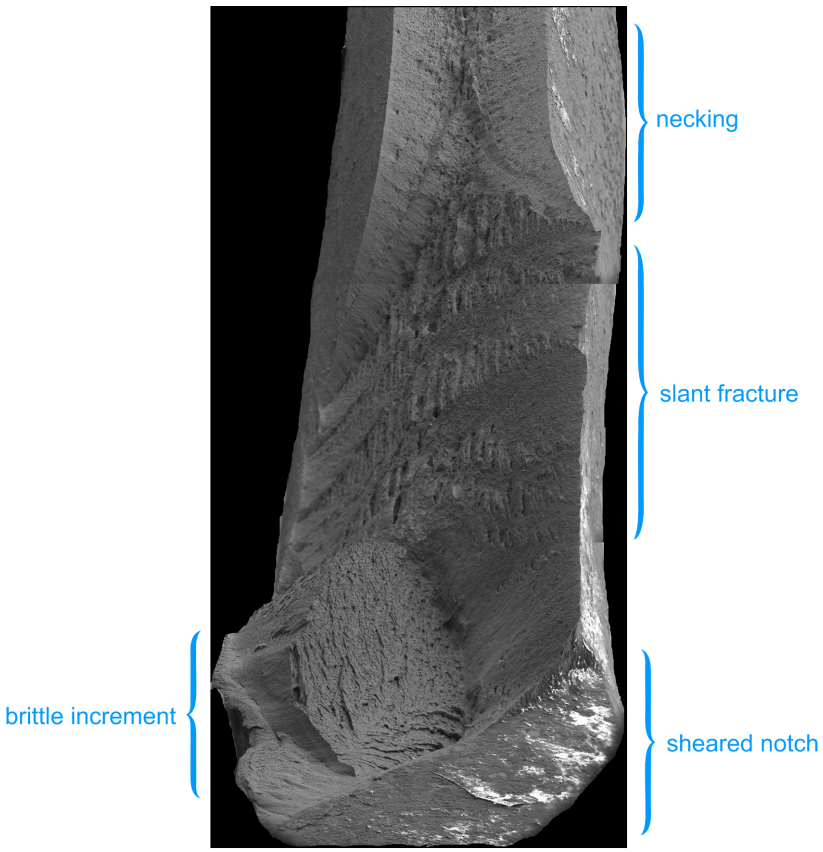

Figure A14: *Stitched SEM image of one half of a XPF1000-UC fracture surface at 120 °C. The images were taken from the notch-side at an angle of 70 ° by tilting.*

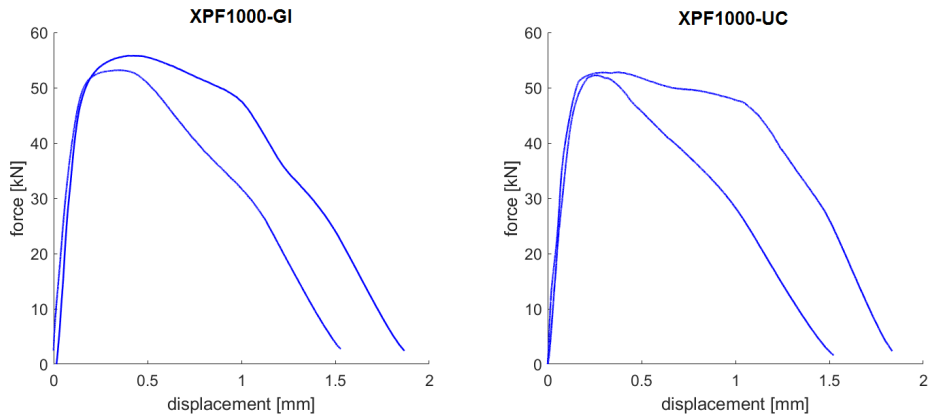

Figure A15: *Global force-displacement curves obtained during EWF testing of XPF1000 samples with sheared notches (2.7 mm thickness) at 120 °C.*

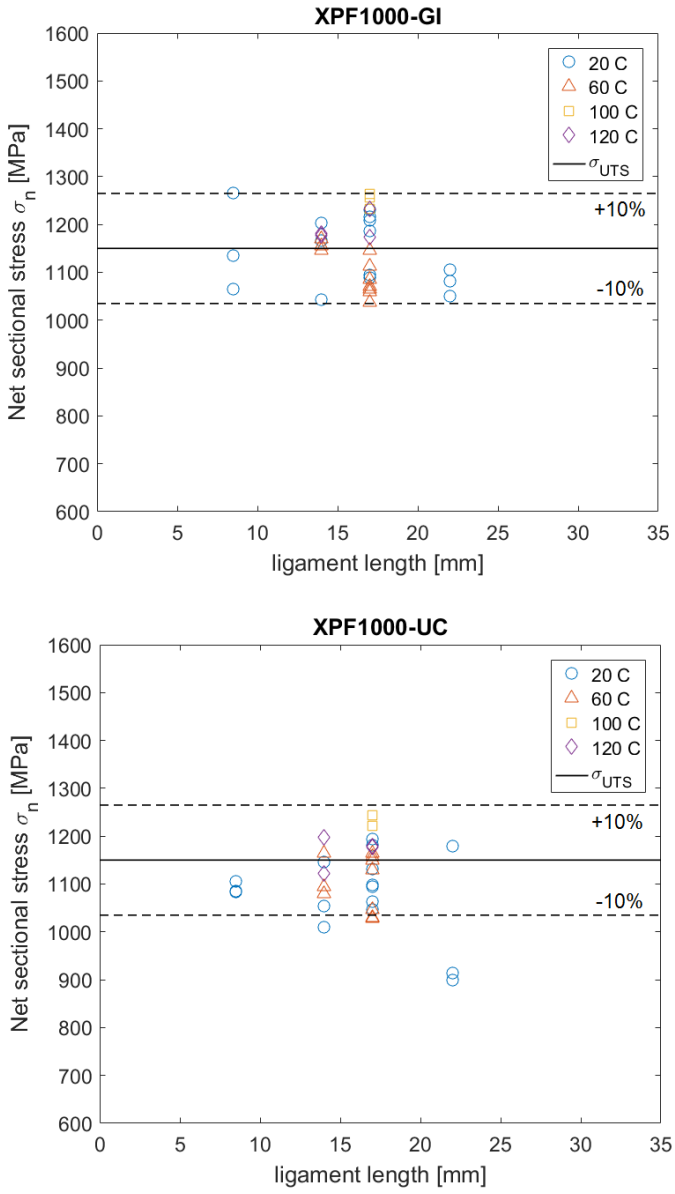

Figure A16: *Maximum net sectional stress as a function of the ligament length experienced during EWF testing of XPF1000 (2.7 mm thickness) with sheared notches for a range of temperatures. The stress criterion is included here with a ±10% interval.*

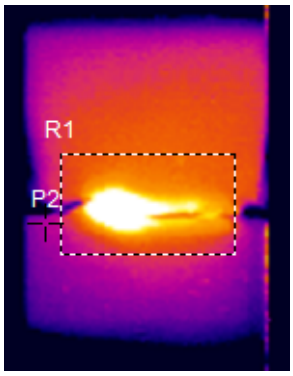

Figure A17: *Temperature measurement locations R1 (ligament volume) and P2 (below the notch)*

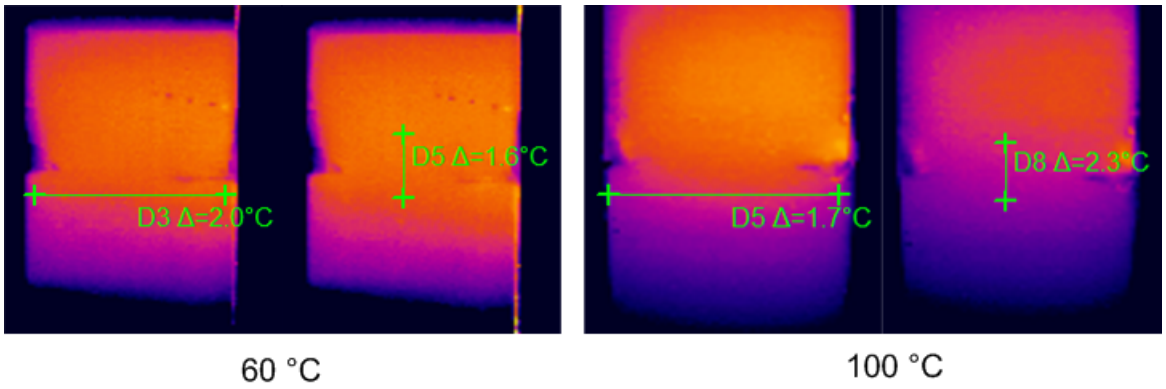

Figure A18: *Temperature gradients across the ligament volume at 60°C and 100°C.*

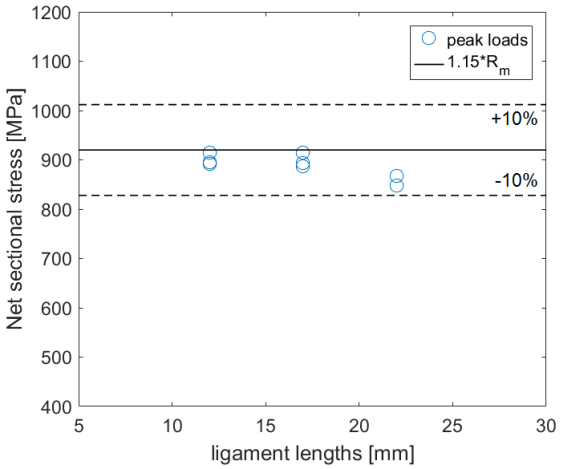

Figure A19: *Maximum net sectional stress as a function of ligament lengths experienced during EWF testing of CP800 (4.0 mm thickness) with sheared notches. The stress criterion is included here with a ±10% interval.*

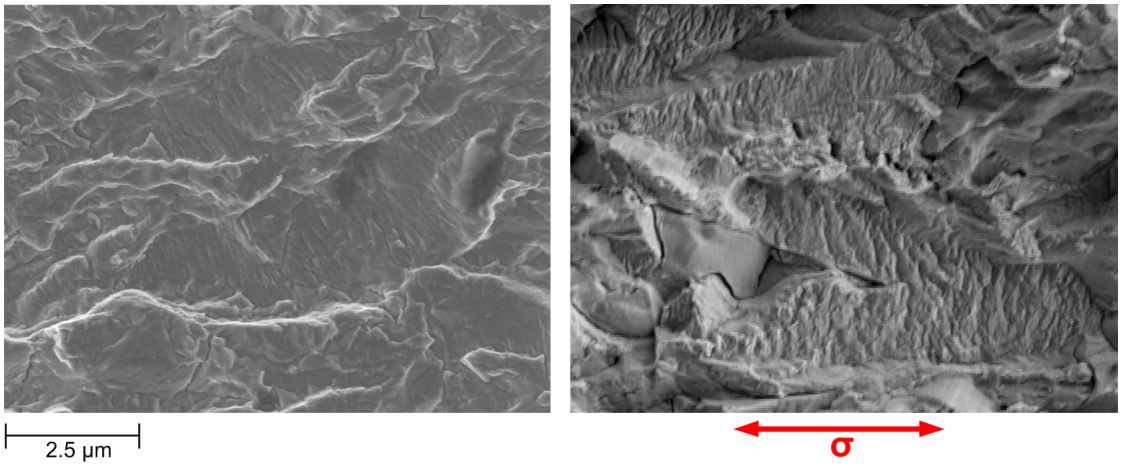

Figure A20: *Two different SEM (secondary electrons) images showing beach marks/striations perpendicular to the loading direction as a result of cyclic fatigue pre-cracking (XPF1000-UC 2.9 mm thickness)*

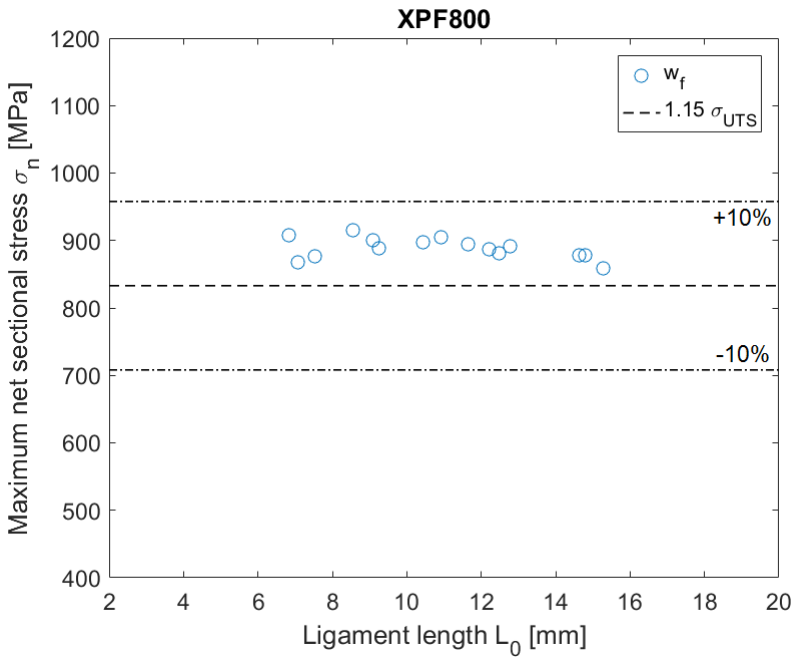

Figure A21: *Maximum net sectional stresses as a function of the ligament length experienced during EWF testing of fatigue pre-cracked XPF800 (3.2 mm thickness).*

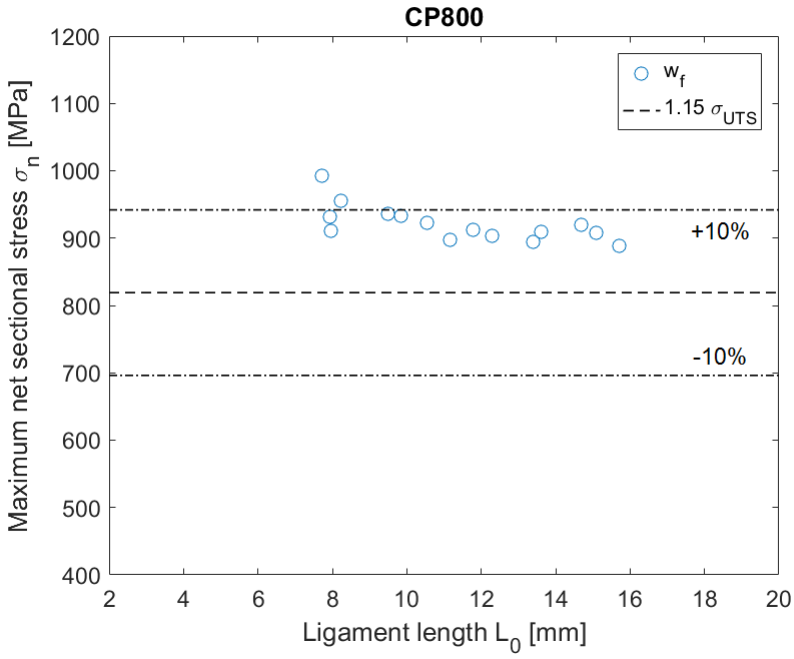

Figure A22: *Maximum net sectional stresses as a function of the ligament length experienced during EWF testing of fatigue pre-cracked CP800 (3.3 mm thickness).*

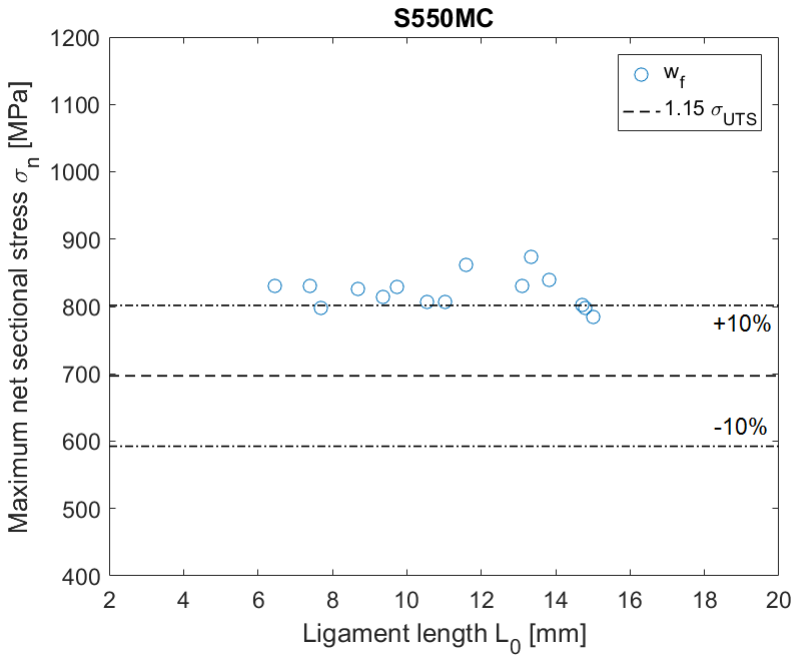

Figure A23: *Maximum net sectional stresses as a function of the ligament length experienced during EWF testing of fatigue pre-cracked S550MC (3.0 mm thickness).*

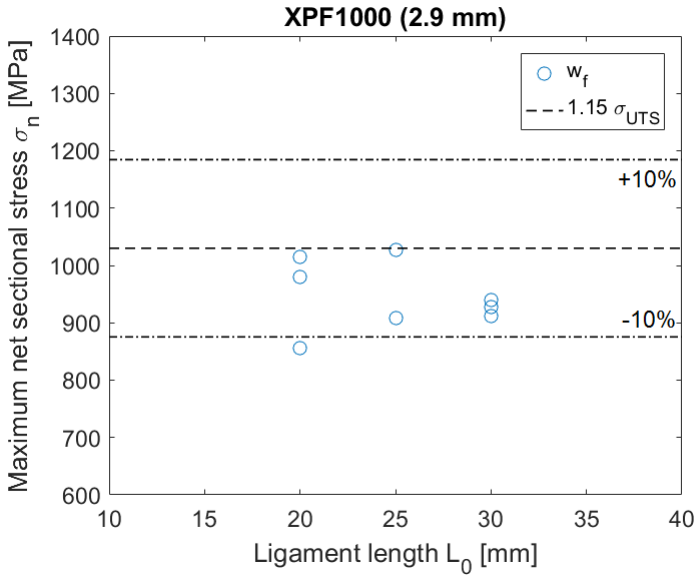

Figure A24: *Maximum net sectional stresses as a function of the ligament length experienced during EWF testing of XPF1000 (2.9 mm thickness) with sheared notches.*

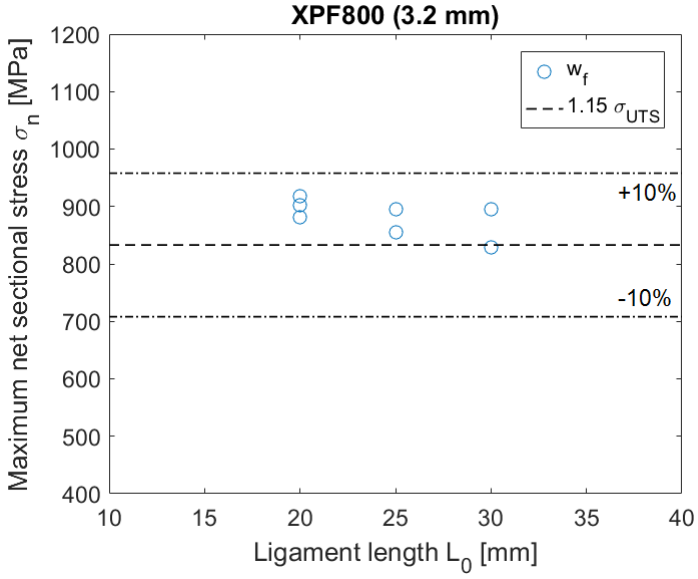

Figure A25: *Maximum net sectional stresses as a function of the ligament length experienced during EWF testing of XPF800 (3.2 mm thickness) with sheared notches.*

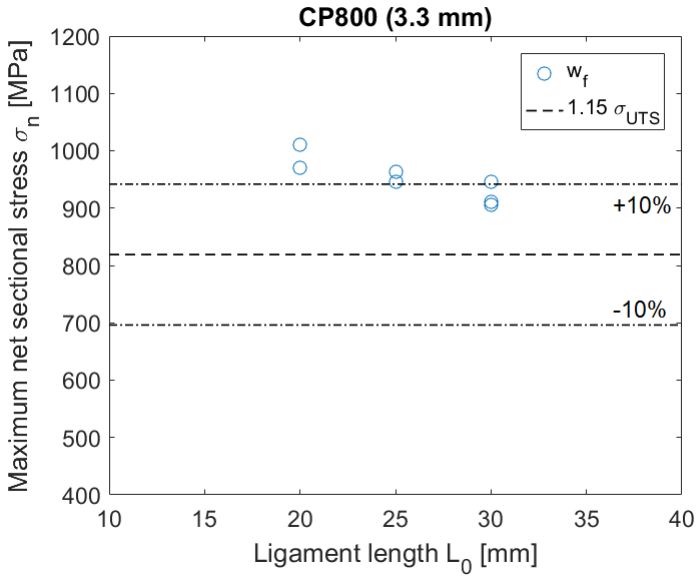

Figure A26: *Maximum net sectional stresses as a function of the ligament length experienced during EWF testing of CP800 (3.3 mm thickness) with sheared notches.*

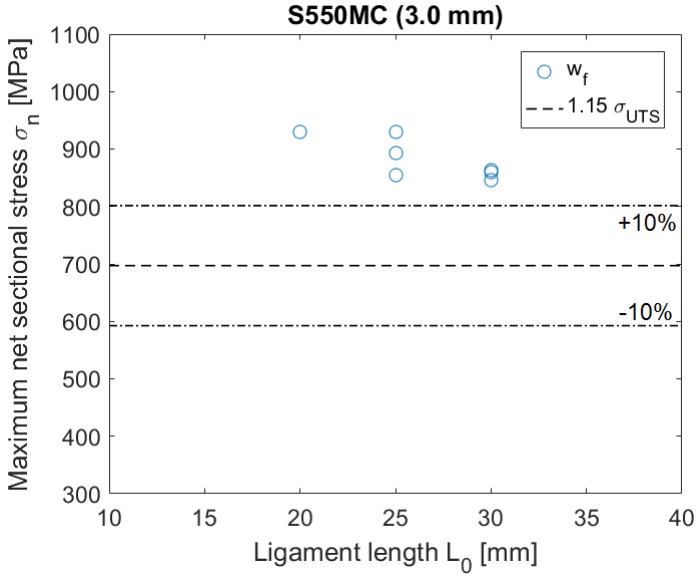

Figure A27: *Maximum net sectional stresses as a function of the ligament length experienced during EWF testing of S550MC (3.0 mm thickness) with sheared notches.*

A.4 Additional results from deep-drawing

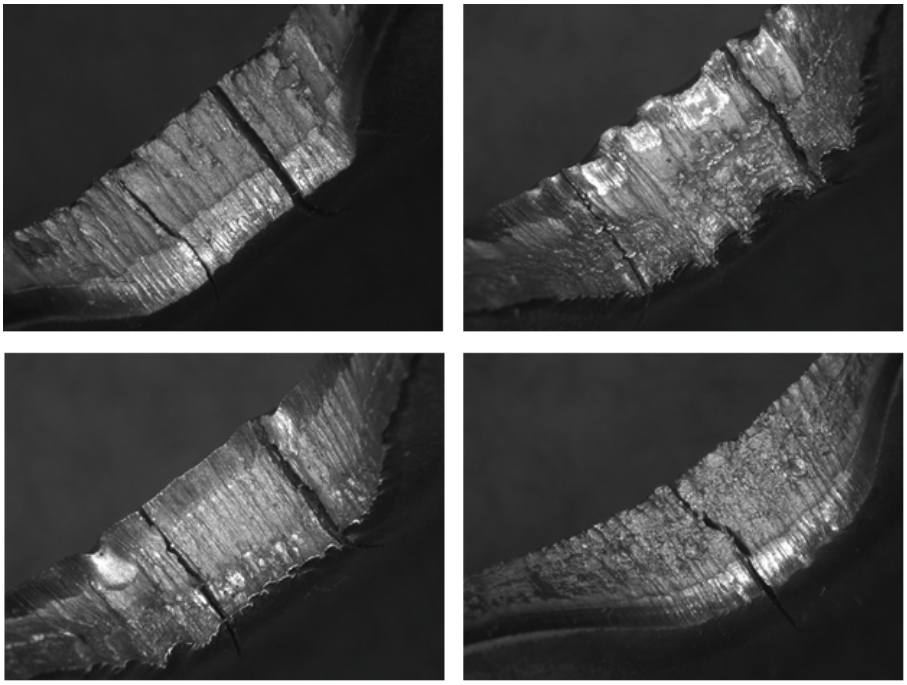

Figure A28: *XPF1000 (2.9 mm) close-up of inner edges.*

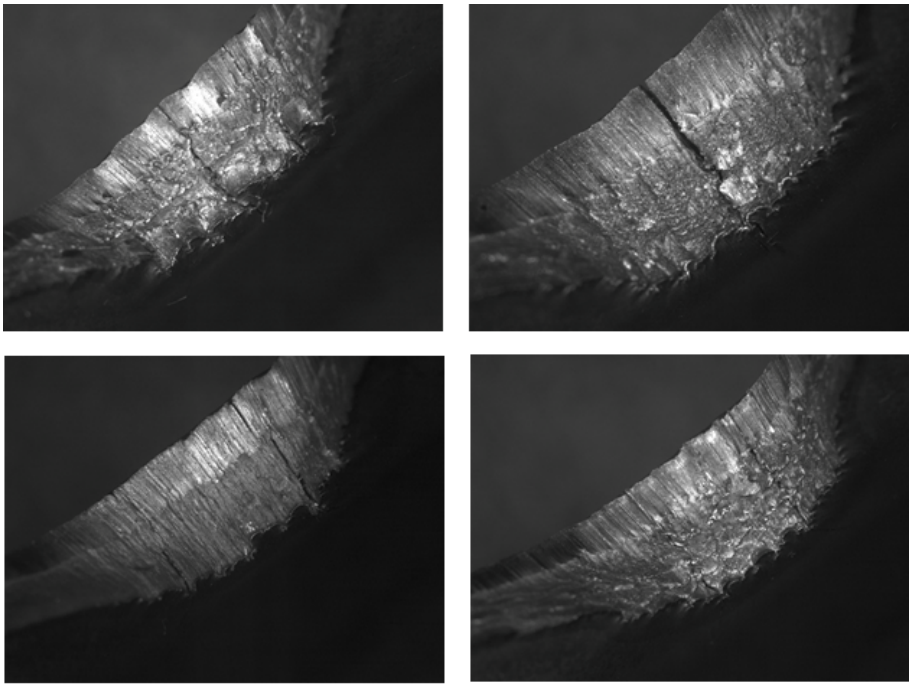

Figure A29: *XPF800 (3.2 mm) close-up of inner edges.*

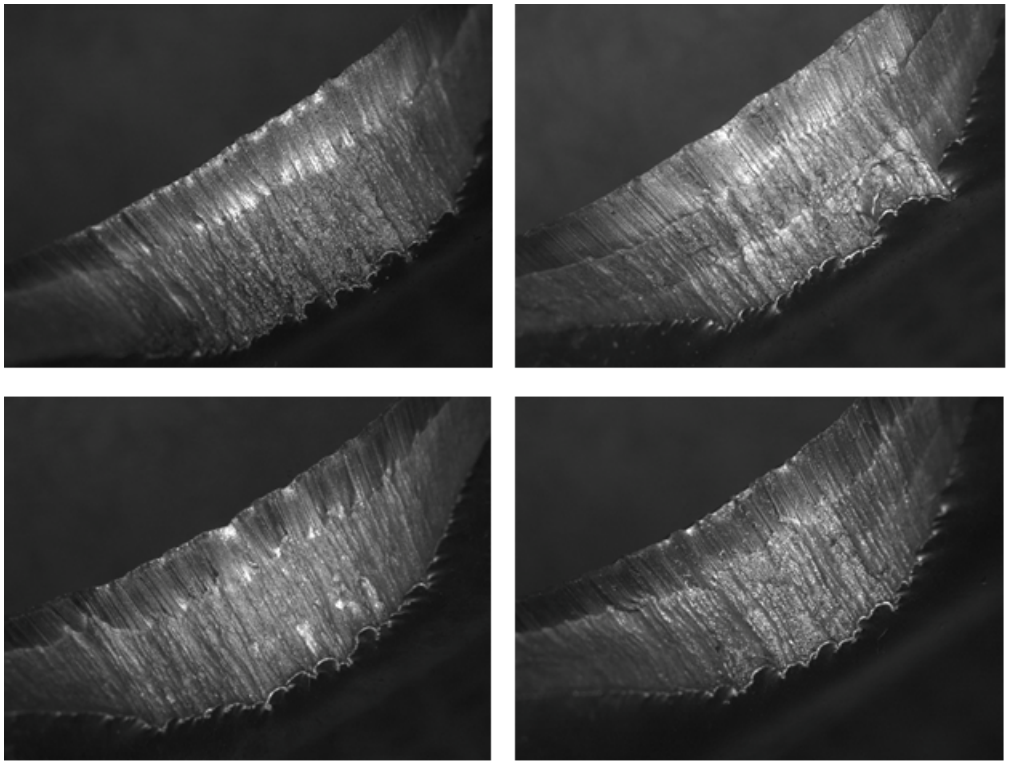

Figure A30: *CP800 (3.3 mm) close-up of inner edges.*

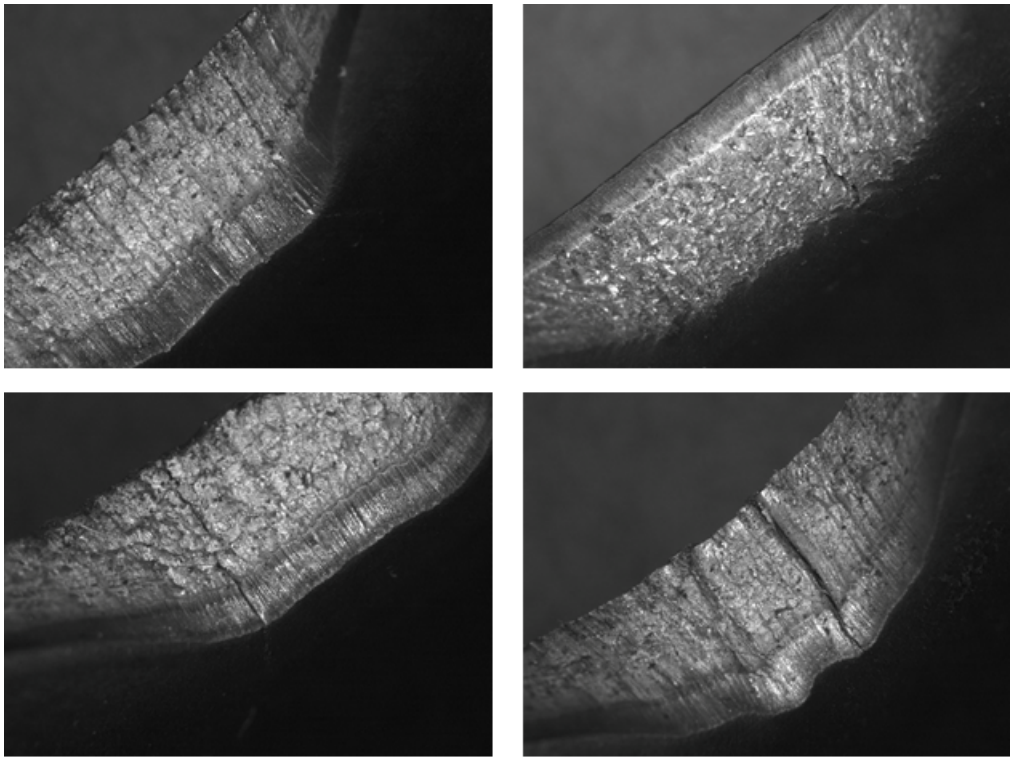

Figure A31: *S550MC (3.0 mm) close-up of inner edges.*

Appendix B

B.1 Ligament length sensitivity analysis

To recall; the splitting of essential and non-essential plastic contributions is allowed:

$$W_e = W_f - W_p \tag{6.29}$$

Dividing by ligament area yields the *specific* work parameters:

$$w_e = w_f - \beta w_p L_0 \tag{6.30}$$

Where the total specific work of fracture is measured during testing, and is calculated by:

$$w_f = \frac{W}{L_0 t} \tag{6.31}$$

The first term in Equation 6.30 causes a proportional shift in the linear regression line, while the second term is related to the *change in slope* of the linear regression line. For the CP800 (4.0 mm thickness) this dependence on L_0 is illustrated by evaluating the two EWF parameters after introducing a certain perturbation/offset in the array of ligament lengths (see Figure B1).

When varying the offset in ligament lengths with ± 1 mm a corresponding change in w_e of ± 232 kJ/m^2 is found. The change in βw_p is found to be $\pm$ 6 kJ/m^3. An under-estimation of the ligament lengths also causes a larger error than an over-estimation due to the non-linear relation. Graphically, the linear fit obtained from the w_f values changes both in magnitude and slope. These findings shows that inaccurate ligament length determination can drastically influence the obtained fracture toughness parameters and should receive proper attention.

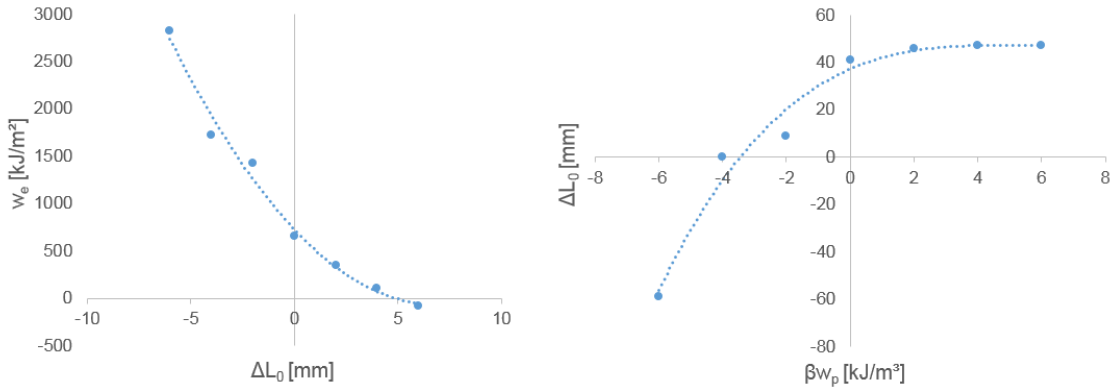

Figure B1: *Sensitivity of essential work of fracture parameters with respect to ligament lengths. A quadratic and cubic fit through the datapoints are included, respectively.*